

DISSERTATION

submitted to the

Combined Faculty of Mathematics, Engineering and Natural Sciences
of Heidelberg University, Germany

for the degree of

Doctor of Natural Sciences

Put forward by

IRINA SMIRNOVA-PINCHUKOVA

born in Tashkent, Uzbekistan

Oral examination: July 27, 2022

COMPARISON OF DIFFERENT STAR FORMATION
TRACERS IN NEARBY AGN HOST GALAXIES

IRINA SMIRNOVA-PINCHUKOVA

REFEREES:

PROF. DR. RALF KLESSEN

APL. PROF. DR. JOCHEN HEIDT

Abstract

This work is a part of the Close AGN Reference Survey (CARS, <https://www.cars-survey.org/>) that is intended to provide the most detailed view of the AGN – host galaxy connection and establish a reference for high-redshifts. The survey consists of 40 nearby Seyfert 1 galaxies with optical integral field unit datacubes and a multi-wavelength observational dataset. The first part of the thesis presents the star-formation-related analysis of the CARS first data release. The panchromatic spectral energy distribution is modeled with additional AGN constraints to infer stellar masses and infrared star formation rates. I also present the novel method of calculating the recent star formation rate from the $H\alpha$ emission in the conditions of AGN contamination using spectral and spatial datacube information. Then I compare the resulting infrared and $H\alpha$ star formation rates with $CO(1-0)$ data to analyze the star formation history and the trends between AGN and host galaxies. The second part of the thesis explores the data from SOFIA airborne observatory. The $[C\ II]$ far-infrared line is a bright coolant in the interstellar medium accessible with ALMA and often used as a star formation rate indicator. The discovery of one of the few known $[C\ II]$ excess galaxies HE 1353–1917 is introduced together with the discussion of its mechanisms and the meaning for the high-redshift objects. This is complemented by the follow-up SOFIA observations of HE 0412–0803 that allowed to confirm the proposed $[C\ II]$ excess mechanism and intrigued us with its puzzling VLA radio continuum data. Overall, in this thesis, I accurately infer, analyze, and compare star formation rate tracers for the CARS objects emphasizing the power of the multi-wavelength approach.

Zusammenfassung

Diese Arbeit ist Teil der Close AGN Reference Survey (CARS, <https://www.cars-survey.org/>), die den detailliertesten Überblick über die Verbindung zwischen AGN und Wirtsgalaxie liefern und eine Referenz für hohe Rotverschiebungen schaffen soll. Die Durchmusterung besteht aus 40 nahe gelegenen Seyfert-1-Galaxien mit optischen Integral Field Unit Datenwürfeln und einem Multi-Wellenlängen-Beobachtungsdatensatz. Im ersten Teil der Arbeit wird die Analyse der ersten CARS-Daten in Bezug auf die Sternentstehung vorgestellt. Die panchromatische spektrale Energieverteilung wird mit zusätzlichen AGN-Beschränkungen modelliert, um Sternmassen und Infrarot-Sternentstehungsraten zu ermitteln. Außerdem stelle ich eine neuartige Methode zur Berechnung der jüngsten Sternentstehungsrate aus der $H\alpha$ -Emission unter den Bedingungen der AGN-Kontamination vor, die spektrale und räumliche Datenwürfelinformationen verwendet. Anschließend vergleiche ich die resultierenden Infrarot- und $H\alpha$ -Sternentstehungsraten mit $CO(1-0)$ -Daten, um die Sternentstehungsgeschichte und die Trends zwischen AGN und Wirtsgalaxien zu analysieren. Der zweite Teil der Arbeit befasst sich mit den Daten des SOFIA-Observatoriums. Die $[C\ II]$ -Linie im fernen Infrarot ist ein Kühlmittel im interstellaren Medium, das mit ALMA zugänglich ist und oft als Indikator für die Sternentstehungsrate verwendet wird. Die Entdeckung einer der wenigen bekannten $[C\ II]$ -Überschussgalaxien HE 1353–1917 wird zusammen mit der Diskussion ihrer Mechanismen und der Bedeutung für die hochrotverschobenen Objekte vorgestellt. Ergänzt wird dies durch die SOFIA-Nachbeobachtungen von HE 0412–0803, die den vermuteten Mechanismus des $[C\ II]$ -Überschusses bestätigen konnten und uns mit ihren rätselhaften VLA-Radiokontinuumsdaten verblüfft haben. Insgesamt konnte ich in dieser Arbeit die Sternentstehungsraten der CARS-Objekte genau ableiten, analysieren und vergleichen, was die Leistungsfähigkeit des Multi-Wellenlängenansatzes unterstreicht.

TO MY LITTLE DAUGHTER MARINA

Contents

Acronyms	3
1 Introduction	7
1.1 Galaxy evolution	9
1.2 Active galactic nuclei	11
1.3 Close AGN Reference Survey	15
1.4 Thesis Outline	20
2 Star Formation in CARS	21
2.1 Introduction	22
2.2 Observational data set	23
2.2.1 Archival broad-band photometry	23
2.2.1.1 Catalog data	23
2.2.1.2 Aperture photometry	23
2.2.2 Galactic extinction and AGN broad-line correction	24
2.2.3 Dedicated broad-band imaging	24
2.2.3.1 DECam optical observations	25
2.2.3.2 WFI optical observations	25
2.2.3.3 PANIC NIR observations	25
2.2.3.4 SCUBA-2 FIR observations	29
2.2.3.5 SOFIA HAWC+ FIR observations	29
2.2.4 Integral-field spectroscopy observations	31
2.3 Analysis	31
2.3.1 Modeling the panchromatic SED	31
2.3.2 Measuring H α -based SFR	36
2.3.2.1 Demarcation lines	36
2.3.2.2 BPT mixing sequence	37
2.3.2.3 BPT morphology	39
2.3.3 Gas-phase metallicity	41
2.4 Results and discussions	44
2.4.1 Finding SFR dependencies on AGN parameters	44
2.4.2 Comparison of SFR tracers for AGN host galaxies	50
2.4.3 Individual comparison of current and recent SFRs	52
2.5 Summary and conclusions	55

3 [C II] Line Excess	59
3.1 Introduction	59
3.2 Observations and analysis	60
3.2.1 SOFIA/FIFI-LS observations	60
3.2.2 VLT/MUSE observations	62
3.2.3 SED fitting and FIR luminosities	63
3.3 Results and discussion	64
3.4 Conclusion	69
3.5 Follow-up observations	70
3.5.1 No [C II] excess	70
3.5.2 VLA puzzle	71
4 Conclusions	75
Summary and outlook	75
Appendix	79
A.1 Figures for the CARS objects	80
A.2 FIFI-LS time window selection	96
Publications	99
Bibliography	101
Acknowledgments	113

Acronyms

ΛCDM	Lambda Cold Dark Matter.
(U)LIRG	(Ultra-)luminous Infrared Galaxy.
2MASS	Two Micron All-Sky Survey.
AGN	Active Galactic Nucleus.
ALMA	Atacama Large Millimeter/submillimeter Array.
APASS	AAVSO Photometric All-Sky Survey.
APO	Apache Point Observatory.
BH	Black Hole.
BLR	Broad-line Region.
CALIFA	Calar Alto Legacy Integral Field Area.
CARS	Close AGN Reference Survey.
CASU	Cambridge Astronomical Survey Unit.
CCD	Charge-coupled Device.
CMB	Cosmic Microwave Background.
CTIO	Cerro Tololo Inter-American Observatory.
DECam	Dark Energy Camera.
DIMM	Dynamic Iterative Map Maker.
DLR	Deutsches Zentrum für Luft- und Raumfahrt.
ENLR	Extended Narrow-line Region.
ESO	European Southern Observatory.
FIFI-LS	Far-Infrared Field-Imaging Line Spectrometer.
FIR	Far Infra-red.
FIS	Far-infrared Surveyor.
FoV	Field of View.
FSRQ	Flat-spectrum Radio Quasar.
FWHM	Full Width at Half Maximum.
GALEX	Galaxy Evolution Explorer.

GASS	Parkes Galactic All Sky Survey.
HAWC	High-resolution Airborne Wideband Camera.
HES	Hamburg-ESO Survey.
HSA	Herschel Science Archive.
IFU	Integral Field Unit.
IMBH	Intermediate-Mass Black Hole.
IMF	Initial Mass Function.
IPAC	Infrared Processing and Analysis Center.
IR	Infra-red.
ISM	Interstellar Medium.
JCMT	James Clark Maxwell Telescope.
JHU	Johns Hopkins University.
KASHz	KMOS AGN Survey at High redshift.
KINGFISH	Key Insights on Nearby Galaxies: a Far-Infrared Survey with <i>Herschel</i> .
KMOS	K-band Multi-Object Spectrograph.
LINER	Low-Ionization Nuclear Emission-line Region.
LOS	Line of Sight.
MaNGA	Mapping Nearby Galaxies at APO.
MAST	Barbara A. Mikulski Archive for Space Telescopes.
MCMC	Markov-chain Monte Carlo.
MPA	Max-Planck-Institute for Astrophysics.
MPIA	Max-Planck-Institute for Astronomy.
MUSE	Multi-Unit Spectroscopic Explorer.
NASA	National Aeronautics and Space Administration.
NED	NASA/IPAC Extragalactic Database.
NIFS	Gemini-North's Near-Infrared Integral Field Spectrometer.
NIR	Near Infra-red.
NLR	Narrow-line Region.
NRAO	National Radio Astronomy Observatory.
NVSS	NRAO VLA Sky Survey.
PACS	Photodetecting Array Camera and Spectrometer.
Pan-STARRS	Panoramic Survey Telescope and Rapid Response System.
PANIC	Panoramic Near-Infrared Camera.
PDR	Photodissociation Region.
PMAS	Potsdam Multiaperture Spectrophotometer.
PSF	Point Spread Function.
PVD	Position-velocity Diagram.
QSO	Quasi-stellar Object.

SAMI	Sydney-Australian-Astronomical-Observatory Multi-object Integral-Field Spectrograph.
SCUBA-2	Submillimetre Common-User Bolometer Array 2.
SDSS	Sloan Digital Sky Survey.
SED	Spectral Energy Distribution.
SFE	Star Formation Efficiency.
SFMS	Star Forming Main Sequence.
SFR	Star Formation Rate.
SINFONI	Spectrograph for INtegral Field Observations in the Near Infrared.
SMBH	Super Massive Black Hole.
SMURF	Sub-mm User Reduction Facility.
SNR	Signal-to-noise Ratio.
SOFIA	Stratospheric Observatory For Infrared Astronomy.
SPIRE	Spectral and Photometric Imaging Receiver.
sSFR	specific Star Formation Rate.
SUPER	Survey for Unveiling the Physics and the Effect of Radiative feedback.
UV	Ultraviolet.
UVOT	Ultraviolet/Optical Telescope.
VIMOS	Visible Multi-object Spectrograph.
VISTA	Visible and Infrared Survey Telescope for Astronomy.
VLA (JVLA)	Karl G. Jansky Very Large Array.
VLBA	Very Long Baseline Array.
VLT	Very Large Telescope.
WFI	Wide-Field Imager.
WISE	Wide-field Infrared Survey Explorer.
WISSH	WISE/SDSS-Selected Hyper-luminous quasar survey.
xCOLD GASS	Extended CO Legacy Database for GASS.
XDR	X-ray Dominated Region.
ZAH	Zentrum für Astronomie der Universität Heidelberg.

1

Introduction

In the night sky, even without any telescope, men observed stars, planets of our Solar System, our galaxy the Milky Way, and other structures they called "nebulae". Throughout the history of astronomy, different types of those structures revealed their nature, such as comets, star clusters, supernovae remnants, etc. German philosopher Immanuel Kant in the 18th century, in his work "General History of Nature and Theory of the Heavens", suggested that some of those structures are other milky ways, and our galaxy is just one of many "Welteninseln" or "island universes". The Great Debate in 1920 questioned the nature of the "spiral nebulae" in detail, with Harlow Shapley and Heber Curtis discussing pieces of evidence for scales and distances toward the known objects. Later in 1924, observations made by Edwin Hubble proved that these nebulae were highly distant, residing outside of the Milky Way. This was the beginning of extragalactic astronomy.

Galaxies are indeed islands of gravitationally bound stars, gas, and dust, soaking in pools of dark matter haloes. Hubble (1926) sorted the shapes of the observed galaxies from the simplest forms he called early-type galaxies to complex structures or late-type galaxies,

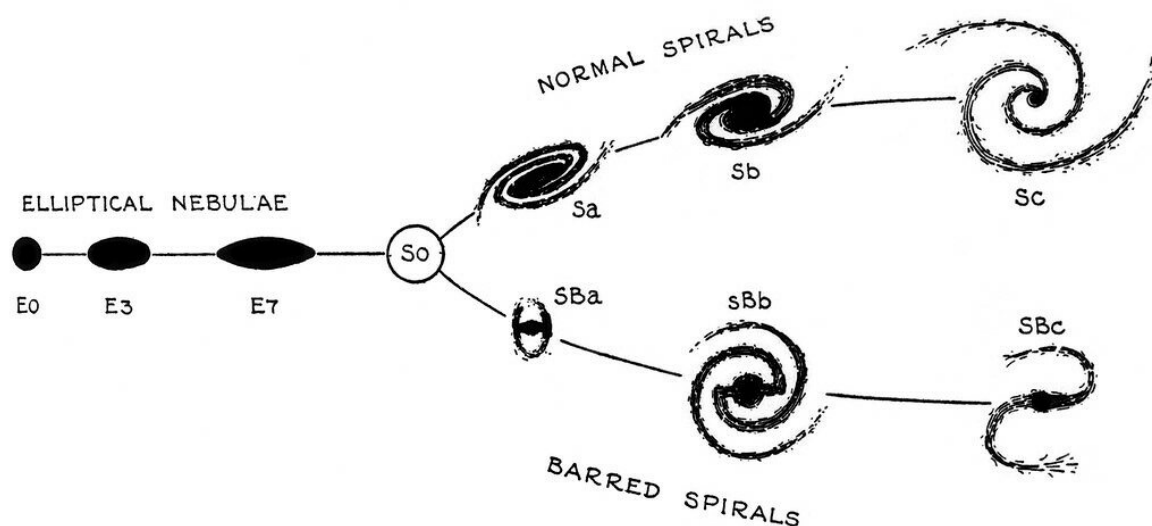


Figure 1.1: The Hubble tuning fork diagram for morphological classification of galaxies. The figure is taken from the book "The Realm of the Nebulae", Hubble (1936).

presenting the famous tuning fork diagram. In Fig. 1.1 the Hubble sequence starts with the spherical **E0** galaxies, continued with more and more flattened elliptical galaxies **E1-E7**, then the lenticulars **S0** at the center of the tuning fork continued with the spirals **S** sorted from tight **Sa** to loose **Sc** compositions and the parallel barred spiral **SB** branch. The fork is often continued by galaxies with the irregular shape **Irr** that do not fit into the sequence. As confusing as it may sound, early- and late-type galaxies have nothing to do with the early and late stages of the galaxy's lifetime.

COSMOLOGICAL MODEL

Redshift z is characterized by the relative difference between the observed λ_{obs} and emitted λ_{emi} wavelength, defined by the following formula:

$$1 + z = \frac{\lambda_{\text{obs}}}{\lambda_{\text{emi}}} = \frac{R(t_{\text{obs}})}{R(t_{\text{emi}})},$$

where $R(t)$ is the scale factor that describes the time evolution of homogeneous and isotropic Universe metrics. The distance between any two given gravitationally unbound parts of the observable universe increases with time; that is why the distant objects are redshifted according to the Hubble's law, with Hubble parameter $H(t) = \dot{a}/a$, where $a(t) = R(t)/R_{\text{now}}$ is the scale factor. This expansion of the Universe is described by the Friedmann (1922) equations:

$$\begin{aligned} \left(\frac{\dot{a}}{a}\right)^2 &= \frac{8\pi G}{3}\rho - \frac{kc^2}{a^2} + \frac{\Lambda c^2}{3}, \\ \frac{\ddot{a}}{a} &= -\frac{4\pi G}{3}\left(\rho + \frac{3p}{c^2}\right) + \frac{\Lambda c^2}{3}, \end{aligned}$$

where G and c are universal constants, the gravitational constant and the speed of light, ρ and p are the matter and radiation energy density and the pressure, and k describes the spatial curvature of the Universe (-1 for open, 0 for flat, or +1 for closed). The cosmological constant Λ represents the energy density of space, or vacuum energy, or the so-called dark energy. The current standard cosmological model Λ CDM includes the notion of dark energy and the cold (interacting weakly, if at all) dark matter.

The earliest electromagnetic radiation in the Universe decoupled from the matter at a redshift $z \sim 1100$ (epoch of recombination), when the neutral atoms formed, releasing photons that are now visible as the Cosmic Microwave Background (CMB). With the CMB observations Planck Collaboration et al. (2020) infer the current cosmological parameters, that are Hubble constant $H_0 = H(t_0) = (67.4 \pm 0.5) \text{ km s}^{-1} \text{ Mpc}^{-1}$, matter density parameter $\Omega_{\text{M}} = \rho_{\text{M}}/\rho_{\text{crit}} = 0.315 \pm 0.007$, dark matter density parameter $\Omega_{\Lambda} = \Lambda/\Lambda_{\text{crit}} = 0.679 \pm 0.013$, the age of the Universe of $13.830 \pm 0.037 \text{ Gyr}$, and the curvature k that corresponds to the flat Universe. For simplicity and better compatibility with the literature I assume the following values throughout the thesis: $H_0 = 70 \text{ km s}^{-1} \text{ Mpc}^{-1}$, $\Omega_{\text{M}} = 0.3$, and $\Omega_{\Lambda} = 0.7$.

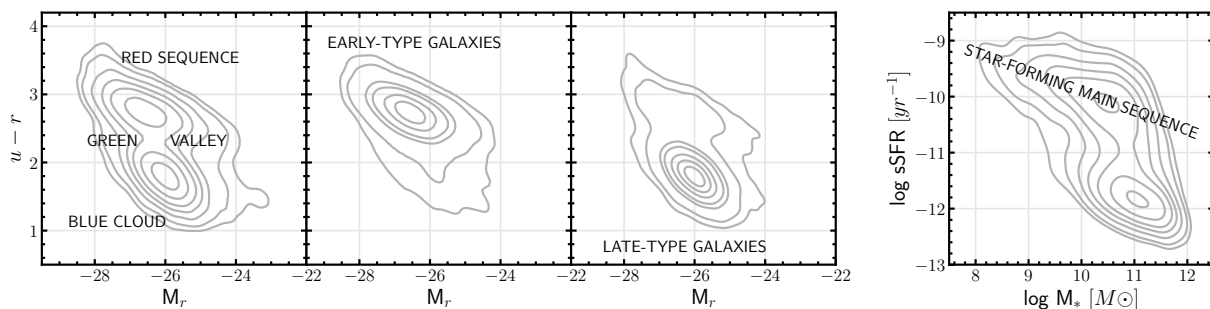


Figure 1.2: Equal density contours for $u - r$ color versus r -band absolute magnitude diagram using MPA JHU SDSS DR7 (Brinchmann et al. 2004; Abazajian et al. 2009, , <https://wwwmpa.mpa-garching.mpg.de/SDSS/DR7/>) and GalaxyZoo2 (Willett et al. 2013; Hart et al. 2016, , <https://data.galaxyzoo.org/>) data for all morphologies, early-, and late-type galaxies (left three panels). Corresponding sSFR versus stellar mass diagram (right panel).

1.1 Galaxy evolution

Hundreds of million years after the Big Bang, galaxies started to form in the potential wells of dark matter that already represented the Universe’s cosmic web. When the Universe was around a third of its nowadays age, which is observed at redshift ~ 1.5 (see COSMOLOGICAL MODEL box on page 8), the majority of galaxies had peculiar morphologies, but then they started to populate the Hubble fork (see, for example, Abraham & van den Bergh 2001; Mortlock et al. 2013).

An image of a galaxy allows us to judge its morphology. But, of course, an optical image also reveals quantities that provide essential characteristics of an object. The color-magnitude diagram (illustrated in Fig. 1.2) is a parametric space of high importance for understanding the behavior of galaxies through time or galaxy evolution. This diagram shows a clear bimodality (Bell et al. 2004; Strateva et al. 2001; Baldry et al. 2004; Wyder et al. 2007; Brammer et al. 2009) in a population of galaxies that are grouped in a so-called red sequence and a blue cloud. The less populated area in between them is called the green valley.

Absolute magnitude is a measure of luminosity and is proportionate to the stellar mass of a galaxy, while its color gives us an estimate of how many young blue stars are present, or, in other terms, the star formation rate (see STAR-FORMING GALAXY box on page 10). The specific star formation rate - stellar mass (sSFR- M_*) diagram as a physical representation of the color-magnitude diagram also shows a bimodality with the Star Forming Main Sequence (SFMS) and the red cloud. The late-type galaxies, or spirals, tend to locate in the blue cloud, which means that they are at the young stage of their evolution, following the tight SFMS relation. In contrast, the early-type bulge-dominated galaxies are mostly red-and-dead.

A star-forming galaxy should encounter critical events to end up in the red cloud, and this transition should be dramatic — at the timescales of only around 1 Gyr according to the under-population of the green valley (Schawinski et al. 2007; Salim 2014). This phenomenon is called quenching, which stops star formation much faster than natural gas exhaustion. Such vigorous processes include galactic interactions, like merging or high-speed fly-bys,

that are able to heat the gas in an entire galaxy. Those environmental outside-in quenching mechanisms are more effective for the small satellite galaxies. The large galaxies cannot be disturbed enough by the satellites to stop star formation completely, but still, they quench. The reason for their quenching seems to come from the insides of the galaxy, and there is one phenomenon powerful enough to do so.

STAR-FORMING GALAXY

In the previous box on the COSMOLOGICAL MODEL (page 8), we stated that the neutral atoms formed in the epoch of recombination. Those atoms are mostly hydrogen and helium; thus, all other elements of the periodic table are considered heavy elements or metals in astronomy. The gas transforms into stars that produce metals during their burning, enriching the gas or the interstellar medium (ISM). Galaxies are the main environments in which those processes thrive, and thereby galaxies are characterized by the star-formation, the quantity and quality of the stars, the level of this enrichment or metallicity, e.t.c.

To quantify star formation, astronomers use the total mass of stars formed per year, or star formation rate (SFR). SFR can be measured directly, counting the stars and modeling their masses and ages, or indirectly, which is more common for extra-galactic astronomy via observations of gas that acts both as the raw material for star formation and as a medium influenced by stellar radiation and supernova shocks. The Kennicutt (1989) – Schmidt (1959) law was the first empirical relation between the gas and star-formation. Star formation rate density scales as some positive power law with the local gas surface density: $\Sigma_{\text{SFR}} \propto \Sigma_{\text{gas}}^n$, where $n \sim 1.4$. All gas emission (whether it is a cold gas that has the potential to be converted into stars or the hot shock escaping from the supernova explosion), from the X-ray, through the ultraviolet (UV), via the optical and infrared (IR), all the way to the radio, both continuum and line emission, can be used as SFR indicators. The global SFR indicators (or tracers) involved in this thesis are calibrated with the $\text{H}\alpha$, $[\text{C II}]$, and $\text{CO}(1-0)$ emission lines and the total IR luminosity and radio continuum at 1.4 GHz. As stars form in cold clouds of molecular gas (traced by $\text{CO}(1-0)$ or $\text{H I } 21 \text{ cm}$ line emission), the estimate of the total molecular gas mass also characterises star formation with star formation efficiency ($\text{SFE} = \text{SFR}/M_{\text{mol}}$) and the depletion time ($\tau_{\text{dep}} = 1/\text{SFE} \sim 1 \text{ Gyr}$ for typical star-forming galaxy). The $\text{H}\alpha$ Balmer emission line originated in a cloud of ionized gas where star formation has recently taken place (the H II region) provides the most accurate indirect estimate of the recent star formation rate.

The specific star formation rate ($\text{sSFR} = \text{SFR}/M_{\star}$) is another star formation characteristic that accounts for the total stellar mass of a galaxy. To weigh the stellar mass, astronomers use the light that is produced by them. The mass-luminosity relation (Kuiper 1938) of individual stars $L/L_{\odot} \propto (M/M_{\odot})^a$, where L_{\odot} and M_{\odot} are the luminosity and mass of the Sun and $1 < a < 6$, and an assumption of star formation history and a function that describes the initial distribution of masses for a population of stars in a galaxy (the initial mass function, IMF) allow to model the observed

galaxy and infer its stellar mass. In this thesis, I use spectral energy distribution (SED, or a number of observed luminosities across the electromagnetic spectrum, see section 2.3.1) to infer the total stellar mass and other parameters.

1.2 Active galactic nuclei

Carl Seyfert (1943) discussed the observations of bright nuclei in nearby spiral nebulae, reporting spectra with unusually broad emission lines. This mystery of Activity of Nuclei of Galaxies captivated Victor Ambartsumian in the 1950s, who suggested that these nuclei must contain bodies of enormous mass and unknown non-stellar nature. Black holes (see BLACK HOLE ACCRETION box on page 13) were known in those years only as mathematical by-products of general relativity, so the scientific society did not consider such objects to exist in reality (though the discovery of neutron stars, made by Jocelyn Bell in 1967, showed the presence of gravitationally collapsed objects, the black hole existence has been confirmed only recently through the detection of gravitational waves by Abbott et al. (2016)). Simultaneously, quasars, or quasi-stellar radio sources, observed in the 3C survey¹ also needed an explanation for their enormous luminosities. Accretion onto a supermassive black hole was suggested as the solution by Edwin Salpeter (1964) and Yakov Zel'dovich (1964); while Donald Lynden-Bell (1969) added that the "dead quasars" reside at the centers of the nearby Seyfert galaxies resulting in the non-stellar emission. In the 1960s and 1970s, with new capacities of astronomy, the observed UV excess objects (observed by Ambartsumian's student Benjamin Markarian) and the bright X-ray objects contained both Seyferts and quasars, confirming the similarities in their nature.

The Unification model (proposed by Antonucci 1993 and Urry & Padovani 1995) explains a number of observational phenomena with an accreting supermassive black hole. At the very center of an active galactic nucleus (AGN), there is an accretion disk, its main engine, that provides optical and UV illumination; the electron plasma around produces inverse Compton hard X-ray emission; the high-speed gas clouds surrounding it are responsible for the broad, highly ionized emission lines (the broad-line region, BLR); the dusty torus emits the IR continuum; the gas clouds located further emit highly ionized narrow lines (the narrow-line region, NLR); and the radio emission of synchrotron and inverse Compton nature arises from relativistic plasma jets launched close to the SMBH and other extended structures such as lobes, rings, etc. Depending on the presence and development of these structures, and the spatial orientation of the nucleus and the host galaxy in relation to us, astronomers observe the variety of AGN types (see Fig. 1.3). The two large groups are radio-loud and radio-quiet AGN (Fanaroff & Riley 1974) with and without a prominent jet emission correspondingly. If the nucleus is bright enough to outshine the host galaxy and the object looks like a point-source, then it is called a quasar or a quasi-stellar object, QSO. Type 1 Seyferts or QSOs (depending on their radio-loudness) show broad emission lines together with highly ionized narrow lines, while type 2 AGN have the BLR obscured by the dust torus showing only the narrow emission lines. Low-ionization nuclear emission-line region galaxies (LINERs) also show only narrow lines but with lower ionization compared to Seyferts.

¹The Third Cambridge Catalogue of Radio Sources, Edge et al. (1959)

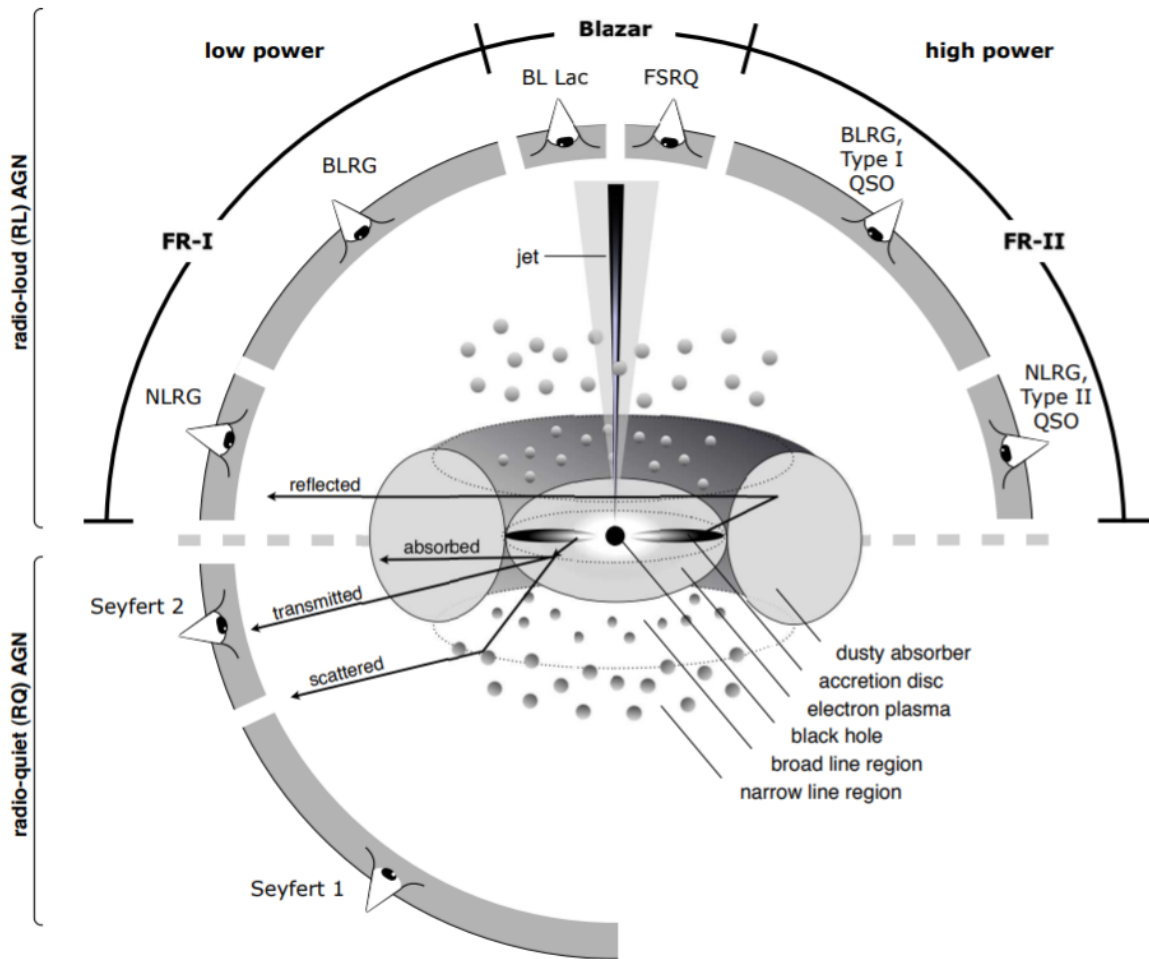


Figure 1.3: Schematic representation of the inner structure of an AGN in the context of the unified model. The type of the observed object depends on the viewing angle. Depending on the presence of a significant jet emission, the AGN type is divided into two large groups of radio-quiet and -loud AGN. The radio-quiet AGN are separated by two sub-groups of unobscured Seyfert 1 and obscured Seyfert 2 AGN. Radio-loud AGN include blazars: BL Lacertae objects and flat-spectrum radio quasars (FSRQs), depending on the optical spectrum; broad line- and narrow line-region galaxies (BLRG and NLRG) with FR-I type of the jet and lower power of the central engine or FR-II jet and higher power (Fanaroff & Riley 1974). The figure is taken from Beckmann & Shrader (2012).

One of the intriguing topics is the changing-look AGN that demonstrate transitions from type 1 to type 2 or/and vice versa (e.g., Denney et al. 2014; McElroy et al. 2016) and changing their X-ray properties (e.g., LaMassa et al. 2015; Ricci et al. 2016) on very short timescales. The mechanisms of this transformation are still a challenge for theoretical astronomy, and the agreement of the unification model with this observational phenomenon is questionable.

We observe AGN as objects, but from a perspective of a galaxy lifetime, the activity of its nucleus is a *stage* or even an *event*. SMBHs are found only in the centers of galaxies and tight correlations, such as famous BH mass – bulge velocity dispersion ($M_{\text{BH}}-\sigma$) relation

BLACK HOLE ACCRETION

A stellar black hole (BH) formed by the gravitational collapse of a star has typical masses of $M_{\text{BH}} \approx 3 - 100 M_{\odot}$, while a supermassive black hole (SMBH) mass is more than a million solar masses. The black hole growth occurs through material accretion and black hole merging, hence catching the rarely observed intermediate-mass black holes (IMBHs, $M_{\text{BH}} = 10^2 - 10^5 M_{\odot}$) may help us to find out more about the history of this intriguing growth. Black hole mass is the main characteristic that defines the gravitational radius together with the event horizon radius (or Schwarzschild radius if the BH is non-rotating), that light cannot escape from:

$$r_{\text{Sch}} = 2 r_{\text{grav}} = \frac{2 GM_{\text{BH}}}{c^2},$$

where the universal constants G and c are the gravitational constant and the speed of light. The accreting black hole is characterized also by the accretion rate \dot{M} and the bolometric luminosity $L_{\text{bol}} = \dot{M}\eta c^2$, where radiative efficiency η is around 10–20 % and even up to 40 % (Thorne 1974; Shankar et al. 2020), that makes the accretion onto BHs the most efficient radiative source in the Universe. While spherical accretion has a limit justified by the balance between the force of radiation and the gravitational force, called the Eddington limit:

$$\begin{aligned} \dot{M}_{\text{Edd}} &= \frac{L_{\text{Edd}}}{\eta c^2}, \\ L_{\text{Edd}} &= \frac{4\pi G c m_p}{\sigma_T} \approx 3.2 \times 10^4 \frac{M_{\text{BH}}}{M_{\odot}} L_{\odot}, \end{aligned}$$

where σ_T and m_p are the Thomson cross section and the mass of a proton; in non-spherical accretion this limit can be exceeded, resulting in super-Eddington accretion and Eddington ratios $\lambda_{\text{Edd}} = L_{\text{bol}}/L_{\text{Edd}} = \dot{M}/\dot{M}_{\text{Edd}}$ more than unity.

(e.g., Ferrarese & Merritt 2000; Kormendy & Ho 2013), indicate for the co-evolution of nuclei and their hosts. Indeed, AGN seems to be one of the key events in galaxy evolution, as there is evidence that most of the SMBH growth occurs in the green valley. SMBH masses in star-forming galaxies follow one scaling law, while the ones in quenched galaxies follow another scaling law (see, for example, Chen et al. 2020). AGN promotes rapid growth of SMBH, or vice-versa; the rapid growth of SMBH result in AGN, while galactic gas heats up, quenching the star formation inside-out. This rough picture is, of course, more complex and peculiar in reality with, for example, the effects of rejuvenation and its connection to AGN (e.g., Mathur 2000; Martín-Navarro et al. 2022) or an idea of independent BH – bulge growth in Jahnke & Macciò (2011). Overall, the co-evolution of SMBH and host galaxy consists of a balance between SMBH feeding and, as a result, AGN feedback.

In numerical simulations of galaxy evolution (e.g., Vogelsberger et al. 2014a; Schaye et al. 2015; Pillepich et al. 2018) AGN feedback such as radiatively-driven winds, mechanical energy, and thermal pressure released from the AGN are routinely incorporated to solve the overcooling problem described by Benson et al. (2003) and to reproduce the characteristics

Table 1.1: Some works report negative, positive, or no AGN feedback effect on the SFR, which emphasizes ambiguity on the observational side.

Negative feedback	Positive feedback	No effect
Ho (2005)	Kim et al. (2006)	Elbaz et al. (2011)
Nandra et al. (2007)	Cresci et al. (2015a)	Bongiorno et al. (2012)
Schawinski et al. (2009)	Cresci et al. (2015b)	Harrison et al. (2012)
Farrah et al. (2012)	Bernhard et al. (2016)	Husemann et al. (2014)
Page et al. (2012)	Santoro et al. (2016)	Balmaverde et al. (2016)
Mullaney et al. (2015)	Maiolino et al. (2017)	Leung et al. (2017)
Shimizu et al. (2015)	Koss et al. (2021)	Woo et al. (2017)
Wylezalek & Zakamska (2016)		Shangguan et al. (2018)
Kakkad et al. (2017)		Scholtz et al. (2020)
Catalán-Torrecilla et al. (2017)		
Bing et al. (2019)		
Bluck et al. (2020)		
Ramos Padilla et al. (2020)		
Brownson et al. (2020)		
Smith et al. (2020)		

of the observed galaxy population such as the galaxy color bimodality (e.g., Vogelsberger et al. 2014b; Nelson et al. 2018). Often two types of the AGN feedback mode are being distinguished, which are called the quasar mode or radiative mode (e.g., Di Matteo et al. 2005; Hopkins et al. 2008; Hopkins & Elvis 2010) and the radio mode, also known as kinetic or maintenance mode (e.g., Bower et al. 2006; Croton et al. 2006; Fabian 2012; Gaspari et al. 2020). The quasar mode is thought to initially quench star formation through powerful radiatively driven winds that remove the gas from the galaxy (e.g., Nesvadba et al. 2008; Feruglio et al. 2010; Maiolino et al. 2012) and thereby suppress star formation. The radio mode is a heating mechanism affecting the gaseous halo that prevents continuous condensation of cold and warm gas, thereby quenching star formation over long timescales and maintaining a low level of star formation in red sequence galaxies (e.g., Brüggén & Kaiser 2002; McNamara et al. 2005; Gaspari et al. 2019; McDonald et al. 2021).

From the observational point of view, as we see only a snapshot of the ongoing evolutionary stage, it is often impossible to identify which feedback type and mechanism is dominant, leading to even more ambiguity (see Fig. 1.4). Strong evidence for radio mode feedback has been collected from galaxy clusters hosting powerful radio galaxies (e.g., Fabian et al. 2006; McNamara & Nulsen 2007). But the role of quasar mode feedback is much more controversial from an observational perspective, as, for example, various studies have reported negative, positive, or no effect from feedback on the sSFRs of the observed AGN host galaxies (see Table 1.1). The reasons for this confusion are not only physical but also technical challenges that arise from the fact that AGN contaminates SFR indicators in every wavelength. A representative observational sample of galaxies, novel methods of "AGN decontamination" to infer SFRs, and usage of different SFR tracers are the required ingredients to get the complete picture of the AGN – SFR connection, and these are the elements this thesis is built from.

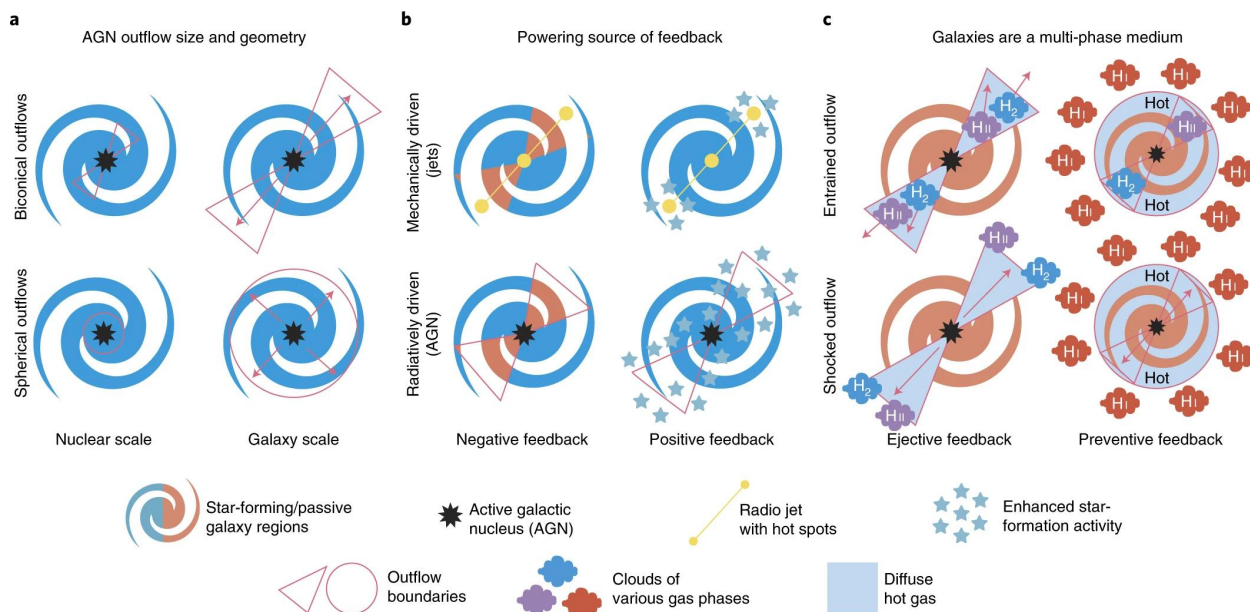


Figure 1.4: Cartoon representation of the possible AGN feedback types taken from Husemann & Harrison (2018). *Left panel a:* ambiguity in AGN outflow size (extended or compact) and geometry (spherical or bi-conical). *Middle panel b:* differences in powering source (radiatively-driven or mechanically-driven by a jet) and the type (negative or positive) of feedback. *Right panel c:* possible behavior of multi-phase gas (cold molecular gas H_2 ; warm-ionized gas $H\text{ II}$; atomic gas $H\text{ I}$). Whether H_2 and $H\text{ II}$ are swept out of the galaxies in a confined shock-front or are entrained in the hot plasma outflow. Another aspect is if accompanying negative feedback is ejective, where gas is rapidly pushed out of the galaxy or is preventive, where halo gas is kept hot and prevents cooling and condensation of $H\text{ I}$ back to the galaxy and thereby stalling the formation of stars on longer timescales.

1.3 Close AGN Reference Survey

Extra-galactic IFU surveys such as the Calar Alto Legacy Integral Field Area (CALIFA, Sánchez et al. 2012) survey and the SDSS Mapping Nearby Galaxies at APO (MaNGA, Bundy et al. 2015) survey study the nearby galaxies in detail, attempting to shed light on galaxy evolution. As AGN may be a key phenomenon in the evolutionary processes, a number of AGN surveys, for example, the KMOS AGN Survey at High redshift (KASHz, Harrison et al. 2016), the SINFONI Survey for Unveiling the Physics and the Effect of Radiative feedback (SUPER, Circosta et al. 2018), and the WISE/SDSS-selected Hyperluminous quasar (WISSH, Bischetti et al. 2017) survey, are focused on luminous AGN at redshifts between 1 and 3 where the peak of star formation resides. However, the downside is a large physical scale of > 7 kpc per arcsecond, significantly limiting the achievable spatial resolution. Our team brings a reference data set that examines AGN with substantial power of the central engine (which means the nucleus should not be obscured, type 1) between low-luminosity (because such AGN do not affect the hosts distinctly (for example, Laha et al. 2018)) and the ultra-luminous AGN (because they are rare, especially in the nearby universe); distance-wise close enough to dissect their host galaxies easily at sub-kpc scales and measure host galaxy characteristics accurately.

The largest catalog of luminous type 1 AGN in the southern hemisphere is the Hamburg-ESO Survey (HES, Wisotzki et al. 2000), where objects were selected through B-band imaging and slitless spectroscopy. A HES sub-sample of 99 type 1 AGN with $z < 0.06$ has been intensively studied by the group of Andreas Eckart in Cologne (for example, Busch et al. 2014). From this sample, 41 galaxies have already been targeted with single-dish submillimetre telescopes to obtain cold molecular gas masses via the CO(1–0) emission line (Bertram et al. 2007). The sub-sample of Bertram et al. (2007), since molecular gas content is the prime fuel for star formation in galaxies and a vital quantity to study the feedback process in galaxies, is serving as the parent sample for the resulting Close AGN Reference Survey, or CARS (P.I.: Dr. Bernd Husemann, www.cars-survey.org). Therefore, the AGN targeted by CARS correspond to the most luminous unobscured AGN in the nearby Universe, allowing a detailed investigation of AGN – host galaxy connection at relatively high spatial resolution.

The CARS project obtains, collects, and analyses spatially resolved multiwavelength data of all essential gas phases of the ISM, i.e., atomic, molecular, warm-ionized, and hot gas, using state-of-the-art facilities (see Fig. 1.5) and methods. The core of the CARS observations is an optical IFU snapshot survey with the Multi-Unit Spectroscopic Explorer (MUSE) on the Very Large Telescope (VLT) taken in 2014-2015 for nearly the entire sample. The MUSE characteristics are essential for separating the AGN and host galaxy emission and studying the stellar and ionized gas components, their respective kinematic fields, ionization conditions, and the distribution of star-forming H II region complexes. The cold gas phases are traced by deep Karl G. Jansky Very Large Array (VLA) observations of H I at ~ 15 -arcsecond resolution and Atacama Large Millimeter Array (ALMA) observations of CO(1–0) at ~ 0.8 -arcsecond resolution. Radio continuum images at C (4–8 GHz) and X (8–12 GHz) bands with ~ 1 -arcsecond resolution were also obtained for nearly the entire sample with the VLA to detect extended radio jets and characterize their luminosity, size, and orientation if present. The [C II] $158\mu\text{m}$ line IFU observations with the Far-Infrared Field-Imaging Line Spectrometer (FIFI-LS) onboard the Stratospheric Observatory For Infrared Astronomy (SOFIA) for several galaxies were aimed to provide a reference for the high-redshift studies that use the [C II] line as a SFR tracer.

With these and many more data collected by our team, we were able to introduce the results valuable for the entire extra-galactic community. CARS' success started with several publications on the unique changing look AGN Mrk 1018 (or HE 0203–0031, McElroy et al. 2016; Husemann et al. 2016b; Krumpke et al. 2017), that captured our attention for many years, making CARS a "survey of one object" in the beginning. Proceeding with a number of papers that also focused on a few objects (the deep Chandra observations of the two galaxies by Powell et al. 2018, the [C II] SOFIA observations in Busch et al. 2018; Smirnova-Pinchukova et al. 2019; Smirnova-Pinchukova et al. in prep., and the very detailed study of HE 1353–1917 in Husemann et al. 2019) the CARS team at last presented the analysis of the entire sample (study of the star formation in bars by Neumann et al. 2019, study of the [O III] wings by Singha et al. 2022, the main MUSE analysis presented in Husemann et al. 2022, and the work that is presented in this thesis Chapter 2, Smirnova-Pinchukova et al. 2022) leading to the CARS data release available at <http://cars.aip.de>.

The CARS project is not only the 41 galaxies (see Table 1.2) but also around 30 team

members from all around the world that provide excellent work and a warm atmosphere. At one of the annual CARS meetings, we visually classified CARS galaxy morphologies based on the optical broad-band images. The team members were independently answering questions about whether a galaxy is bulge-dominated **E**, disk-dominated **S** or irregular **Irr**; barred **B**, unbarred or uncertain; shows the presence of tidal tails, nearby companions and interactions with them **int** or if the galaxy appears isolated. I provide the result classification according to the majority of the votes in Table 1.2 (note that the classification differs from the discussed Hubble tuning fork). For more details and the voting results, see Husemann et al. (2022, Table 4).

Figure 1.5: Facilities used by CARS and involved in this thesis study. *Top:* Very Large Telescope (VLT) operated by the European Southern Observatory on Cerro Paranal in the Atacama Desert of northern Chile. Photo credit: G. Hüdepohl/ESO. *Middle:* Stratospheric Observatory for Infrared Astronomy (SOFIA), an airborne observatory operated by NASA and the German Aerospace Center (DLR). Photo credit: C. Thomas/NASA. *Bottom:* Karl G. Jansky Very Large Array (VLA) at the National Radio Astronomy Observatory (NRAO), a centimeter-wavelength radio astronomy observatory located in central New Mexico on the Plains of San Agustin. Photo credit: NRAO/AUI/NSF.



Table 1.2: CARS targets and their characteristics as reported in Husemann et al. (2022, see Tables 1, 4, and 6).

Object	Other Name	α (J2000) [h:m:s]	δ (J2000) [$^{\circ}$: $'$: $''$]	z^a	Distance ^b [Mpc]	Morphology ^c	b/a^d	M_{BH}^e [$10^6 M_{\odot}$]	L_{bol}^f [$10^{43} \text{ erg s}^{-1}$]	λ_{Edd}	Comments
HE 0021-1810		00:23:39.4	-17:53:54	0.0537	236.38	E	0.97 ± 0.01	12.3 ± 3.2	6.6 ± 0.7	0.04 ± 0.01	
HE 0021-1819		00:23:55.4	-18:02:51	0.0533	237.31	SB int	0.96 ± 0.01	6.1 ± 1.3	6.4 ± 0.6	0.08 ± 0.02	
HE 0040-1105	RBS 101	00:42:36.9	-10:49:22	0.0419	185.60	E	0.88 ± 0.02	5.5 ± 0.8	13.4 ± 1.3	0.19 ± 0.04	
HE 0045-2145	MCG-04-03-014	00:47:41.2	-21:29:28	0.0214	92.56	SB	0.92 ± 0.02	—	—	—	no AGN ^g
HE 0108-4743	RBS 162	01:11:09.7	-47:27:37	0.0239	104.36	SB	0.94 ± 0.01	0.5 ± 0.1	4.3 ± 0.4	0.69 ± 0.15	
HE 0114-0015	RBS 175	01:17:03.6	00:00:27	0.0458	202.26	SB int	0.69 ± 0.02	2.8 ± 0.6	4.4 ± 0.4	0.13 ± 0.03	outflow
HE 0119-0118	Mrk 1503	01:21:59.8	-01:02:24	0.0548	242.60	SB	0.98 ± 0.01	15.9 ± 2.4	48.0 ± 4.8	0.24 ± 0.04	no AGN ^g
HE 0150-0344		01:53:01.5	-03:29:23	0.0480	204.09	Irr int	0.91 ± 0.03	—	—	—	changing-look AGN
HE 0203-0031	Mrk 1018	02:06:16.0	-00:17:29	0.0425	187.79	Irr int	0.71 ± 0.07	—	—	—	changing-look AGN
HE 0212-0059	Mrk 590	02:14:33.6	-00:46:00	0.0264	115.31	S	0.88 ± 0.01	86.8 ± 17.5	21.3 ± 2.1	0.02 ± 0.00	
HE 0224-2834	AM 0224-283	02:26:25.9	-28:21:01	0.0602	268.06	Irr int	0.34 ± 0.28	35.8 ± 3.7	34.6 ± 3.5	0.08 ± 0.01	
HE 0227-0913	Mrk 1044	02:30:05.5	-08:59:53	0.0165	71.35	S	0.86 ± 0.01	1.0 ± 0.2	14.2 ± 1.4	1.12 ± 0.27	
HE 0232-0900	NGC 985	02:34:37.8	-08:47:15	0.0427	190.99	Irr int	0.98 ± 0.01	79.1 ± 9.8	111.2 ± 11.1	0.11 ± 0.02	
HE 0253-1641		02:56:02.6	-16:29:15	0.0319	138.64	SB	0.92 ± 0.05	2.3 ± 0.3	14.5 ± 1.5	0.49 ± 0.08	outflow
HE 0345+0056		03:47:40.2	01:05:14	0.0310	135.99	E	0.98 ± 0.01	2.3 ± 0.2	92.5 ± 9.2	3.22 ± 0.31	
HE 0351+0240	RBS 489	03:54:09.5	02:49:31	0.0354	158.52	Irr	0.64 ± 0.01	6.6 ± 1.1	16.9 ± 1.7	0.20 ± 0.05	
HE 0412-0803		04:14:52.7	-07:55:40	0.0380	168.31	E	0.91 ± 0.01	35.9 ± 16.9	66.2 ± 6.6	0.15 ± 0.15	
HE 0429-0247	RBS 550	04:31:37.1	-02:41:24	0.0423	185.83	S or E	0.74 ± 0.02	2.3 ± 0.4	22.3 ± 2.2	0.75 ± 0.15	
HE 0433-1028	Mrk 618	04:36:22.2	-10:22:34	0.0355	156.49	SB	0.80 ± 0.01	14.6 ± 1.7	58.4 ± 5.8	0.32 ± 0.06	
HE 0853+0102		08:55:54.2	00:51:11	0.0527	231.75	S	0.64 ± 0.02	9.2 ± 4.3	9.8 ± 1.0	0.08 ± 0.10	
HE 0853-0126		08:56:17.8	-01:38:08	0.0596	268.10	SB	0.67 ± 0.04	0.2 ± 0.0	3.8 ± 0.4	1.45 ± 0.32	super-Eddington
HE 0934+0119	Mrk 707	09:37:01.0	01:05:43	0.0507	224.08	SB	0.68 ± 0.01	4.3 ± 0.6	47.3 ± 4.7	0.87 ± 0.13	
HE 0949-0122	Mrk 1239	09:52:19.2	-01:36:43	0.0197	86.68	E	0.82 ± 0.01	0.7 ± 0.2	5.3 ± 0.5	0.61 ± 0.17	
HE 1011-0403	PG 1011-040	10:14:20.6	-04:18:40	0.0587	261.09	SB int	0.72 ± 0.01	9.5 ± 1.1	68.3 ± 6.8	0.57 ± 0.11	
HE 1017-0305	Mrk 1253	10:19:32.9	-03:20:14	0.0491	222.46	SB int	0.69 ± 0.05	38.5 ± 4.1	51.5 ± 5.2	0.11 ± 0.01	
HE 1029-1831		10:31:57.4	-18:46:34	0.0405	177.86	SB int	0.99 ± 0.04	6.4 ± 0.8	20.0 ± 2.0	0.25 ± 0.04	
HE 1107-0813		11:09:48.5	-08:30:15	0.0585	259.64	S	0.91 ± 0.01	39.3 ± 7.6	128.6 ± 12.9	0.26 ± 0.05	
HE 1108-2813	ESO 438-9	11:10:48.0	-28:30:04	0.0240	104.76	SB	0.89 ± 0.04	6.0 ± 1.1	11.1 ± 1.1	0.15 ± 0.030	ultra-fast outflow
HE 1126-0407	PG 1126-041	11:29:16.6	-04:24:08	0.0605	278.18	S	0.67 ± 0.05	24.4 ± 4.2	225.5 ± 22.6	0.73 ± 0.16	
HE 1237-0504	NGC 4593	12:39:39.4	-05:20:39	0.0083	38.81	SB	0.64 ± 0.03	5.4 ± 1.0	4.4 ± 0.4	0.06 ± 0.01	
HE 1248-1356	IC 3834	12:51:32.4	-14:13:17	0.0145	63.46	S	0.68 ± 0.01	1.4 ± 0.4	0.8 ± 0.1	0.05 ± 0.02	
HE 1310-1051	PG 1310-109	13:13:05.8	-11:07:42	0.0343	150.71	S	0.74 ± 0.01	16.8 ± 1.6	31.1 ± 3.1	0.15 ± 0.02	
HE 1330-1013	MCG-02-35-001	13:32:39.1	-10:28:53	0.0225	96.50	SB int	0.92 ± 0.03	1.5 ± 0.4	5.6 ± 0.6	0.30 ± 0.09	
HE 1353-1917	ESO 578-9	13:41:13.0	-14:38:41	0.0413	184.83	SB	0.57 ± 0.01	7.5 ± 1.0	76.2 ± 7.6	0.81 ± 0.15	
HE 1417-0909		14:20:06.2	-09:23:14	0.0437	194.93	Sb int	0.29 ± 0.01	32.4 ± 4.7	12.6 ± 1.3	0.03 ± 0.01	
HE 2128-0221		21:30:49.9	-02:08:15	0.0527	233.97	S	0.89 ± 0.01	13.9 ± 2.2	27.4 ± 2.7	0.16 ± 0.03	
HE 2211-3903	ESO 344-16	22:14:42.0	-38:48:23	0.0397	175.35	SB	0.60 ± 0.01	2.6 ± 0.4	10.5 ± 1.0	0.32 ± 0.06	
HE 2222-0026		22:24:35.3	-00:11:04	0.0581	264.83	SB int	0.85 ± 0.01	36.7 ± 5.7	21.1 ± 2.1	0.05 ± 0.01	
HE 2233+0124		22:35:42.0	01:39:33	0.0567	252.56	SB	0.88 ± 0.04	11.2 ± 1.7	25.7 ± 2.6	0.18 ± 0.03	
HE 2302-0857	Mrk 926	23:04:43.4	-08:41:09	0.0470	208.04	S	0.51 ± 0.01	99.7 ± 12.9	30.1 ± 3.0	0.02 ± 0.00	
							0.94 ± 0.08	92.8 ± 13.0	84.2 ± 8.4	0.07 ± 0.02	

^a Accurate systemic redshift of the host galaxies based on the stellar continuum.

^b Distance calculated according to the cosmological model, see box on page 8.

^c Morphological classification according to the majority of the CARS team votes, see text on the page 17 for details.

^d Axis ratio of the elliptical isophote at an intrinsic i band surface brightness of $24.5 \text{ mag arcsec}^{-2}$.

^e BH mass estimated from the BLR $H\beta$ luminosity and FWHM following Greene & Ho (2005b,a). A systematic error of 0.3 dex is typically assumed for the precision of single-epoch BH mass estimate for a single object.

^f Bolometric luminosity estimated from the $H\beta$ luminosity (see text for details). Errors are dominated by the systematic uncertainty of the absolute flux calibration which is assumed to be 10 per cent.

^g Misclassified starburst galaxy with no AGN.

1.4 Thesis Outline

The thesis consists of two main chapters except for the introduction and the conclusions. **Chapter 2** corresponds to one of the most recent papers published by the CARS team with me as a leading author. Smirnova-Pinchukova et al. (2022), as one out of the three CARS data release papers, is a work that characterizes properties of the entire CARS sample, introducing the new methods as well as discussing the CARS objects as a whole, comparing to other samples, and individually, noting the peculiarities of the galaxies one-by-one. **Chapter 3** corresponds to the first paper published by the CARS team with me as a leading author, where the SOFIA observations of 5 CARS galaxies are analyzed. Smirnova-Pinchukova et al. (2019) is a short paper; nevertheless, it was awarded the Ernst Patzer Prize² for one of the best publications by young MPIA/ZAH scientists in 2019. In section 3.5 of this chapter, I add the unpublished study of the follow-up SOFIA observations, as it completes the conclusions of Smirnova-Pinchukova et al. (2019). After the PhD defense, a more careful and detailed analysis is planned to be published as a separate paper.

For better readability of this manuscript, as the main papers of this thesis depend on several other CARS studies, I add necessary parts of publications that belong to other leading authors (some of them include my contribution only as a co-author, some of them do not have my contribution at all) in separate boxes (see, for example, QDEBLEND^{3D} box on page 30). All work that is published by my collaborators is therefore emphasized to avoid confusion.

²www.mpia.de/5012887/2019_11_29_Patzer_e

2

No obvious signature of AGN feedback on star formation, but subtle trends

Active galactic nuclei (AGN) are thought to be responsible for the suppression of star formation in massive $\sim 10^{10} M_{\odot}$ galaxies. While this process is a key feature in numerical simulations of galaxy formation, it has not been unambiguously confirmed in observational studies yet. The characterization of the star formation rate (SFR) in AGN host galaxies is challenging as AGN light contaminates most SFR tracers. Furthermore, the various SFR tracers are sensitive to different timescales of star formation from approximately a few to 100 Myr. We aim to obtain and compare SFR estimates from different tracers for AGN host galaxies in the Close AGN Reference Survey (CARS) to provide new observational insights into the recent SFR history of those systems. We constructed integrated panchromatic spectral energy distributions (SEDs) to measure the far infrared (FIR) luminosity as a tracer for the recent (<100 Myr) SFR. In addition we used the integral-field unit (IFU) observation of the CARS targets to employ the $H\alpha$ luminosity decontaminated by AGN excitation as a proxy for the current (<5 Myr) SFR. We find that significant differences in specific SFR of the AGN host galaxies as compared with the larger galaxy population disappear once cold gas mass, in addition to stellar mass, is used to predict the SFR for a specific AGN host. Only a tentative trend with the inclination of the host galaxy remains, such that SFR appears slightly lower than expected when the galaxies of unobscured AGN appear more edge-on along our line-of-sight, particular for dust-insensitive FIR-based SFRs. We identify individual galaxies with a significant difference in their SFR which can be related to a recent enhancement or decline in their SFR history that might be related to various processes including interactions, gas consumption, outflows, and AGN feedback. AGN can be present in various stages of galaxy evolution which makes it difficult to relate the SFR solely to the impact of the AGN. Our study shows that stellar mass alone is an insufficient parameter to estimate the expected SFR of an AGN host galaxy compared to the underlying non-AGN galaxy population. We do not find any strong evidence for a global positive or negative AGN feedback in the CARS sample. However, there is tentative evidence that 1) the relative orientation of the AGN engine with respect to the host galaxies might alter the efficiency of AGN feedback and that 2) the recent SFH is an additional tool to identify rapid changes in galaxy growth driven by the AGN or other processes.

2.1 Introduction

One common difficulty in observational studies is the measurement of the basic AGN host galaxy parameters such as SFR and stellar mass, because the AGN light can dominate the total emission of the host galaxy across nearly the entire electro-magnetic spectrum from radio to X-rays. Hence, it can be challenging to measure the SFR or stellar mass from commonly used proxies and various strategies have been used in the literature to mitigate the issue. The stellar mass can be easily determined from optical spectra or NIR-optical photometry in obscured AGN (e.g., Kauffmann et al. 2003; Silverman et al. 2009; Aird et al. 2012; Mignoli et al. 2013) as the light from the central AGN is blocked by dust along our line of sight. However, the drawback is that AGN parameters such as black hole mass can usually not be directly inferred for obscured AGN, except for few very nearby systems using the narrow-line region kinematics (e.g., Barth et al. 2001; Walsh et al. 2013).

The SFR of a galaxy is usually determined either from the UV radiation of young stars (e.g., Salim et al. 2007), the ionizing photons from H II regions using H α or [O II] (e.g., Kennicutt & Kent 1983; Kewley et al. 2004), the reheated warm and cold dust at MIR and FIR wavelengths (e.g., Kennicutt 1998), or the radio emission produced in supernova explosions (e.g., Condon 1992). All those tracers can be significantly contaminated by AGN emission even in obscured AGN. The UV or radio emission can be spatially separated through high-angular observations (Fernández-Ontiveros et al. 2018; Rosario et al. 2021). Alternatively, the overall spectral energy distribution is decomposed into various emitting components of a galaxy including AGN, star-formation heated dust and stars. Examples of such SED fitting codes are (X-)CIGALE (Noll et al. 2009; Yang et al. 2020), MAGPHYS (da Cunha et al. 2008), AGNFITTER (Calistro Rivera et al. 2016) or FORTESFIT (Rosario 2019), which can be used to infer stellar mass, IR-based SFR and AGN luminosity simultaneously even for unobscured type 1 AGN. One potential drawback of IR-based SFR tracers for AGN feedback studies is that it traces the SFR on relatively long timescales of ~ 100 Myr and therefore the SFR can be significantly over or underestimated for a strongly declining or rising SFR within that timescale (Hayward et al. 2014).

Considering that the quasar-mode feedback is expected to be a fast process, the H α line may be a more viable tracer for the feedback, considering that it probes the current SFR on < 5 Myr timescales. Unfortunately, the H α line can be strongly boosted by AGN ionization. In order to use H α as a SFR tracer, optical emission lines diagnostic diagrams such as the Baldwin-Phillips-Terlevich diagrams (Baldwin et al. 1981) have been extensively used to distinguish between AGN and H II region excitation. A comprehensive classification scheme with such diagnostic diagrams has been developed Kewley et al. (2006). In particular with integral-field unit spectroscopy, the usage of BPT diagrams has been extended to map the ionization conditions across galaxies to exclude regions from the SFR estimation dominated by AGN ionization using such BPT demarcation lines (e.g., Husemann et al. 2014; Nascimento et al. 2019). However, the superposition of different ionization conditions along the line-of-sight is a common scenario. The observed AGN mixing sequence (MS) arises from such a superposition, and an analytic approach to separate the relative contribution was presented in Davies et al. (2014b,a), Davies et al. (2016), and Davies et al. (2017).

In this chapter we use panchromatic SEDs to estimate stellar masses and FIR-based SFRs; and analyze the CARS IFU data to infer H α based SFRs adopting a new algorithm

to separate the contribution to the H α -line from other excitation mechanisms. In addition, we explore the use of different prescriptions to predict the expected SFR from the non-AGN galaxy population as control samples. This allows us to investigate links with AGN parameters depending on the actual SFR tracers and control sample properties being used as well as to distinguish between potentially declining and increasing star formation histories amongst the AGN host galaxies.

2.2 Observational data set

2.2.1 Archival broad-band photometry

We collect publicly available broad-band photometry from archival sources combined with dedicated observations for CARS targets to construct their panchromatic spectral energy distributions. Where catalogs are not available or do not properly handle extended sources, we extract consistent aperture photometry from the public survey images. All photometric measurements are listed in Table 2.1 and their origin is described below.

2.2.1.1 Catalog data

We directly took data from the *Herschel*/SPIRE point source catalog (250 μ m, 350 μ m, and 500 μ m bands, Schulz et al. 2017), the *Akari*/FIS bright source catalog (N60, N160, WIDE-L, and WIDE-S bands, Yamamura et al. 2009), and the 2MASS extended source catalog (J, H, and K_S bands, Jarrett et al. 2000) without further processing. The GALEX source catalog (FUV and NUV bands, Bianchi et al. 2017) were used only to compare the fluxes to our own aperture photometry measurements.

2.2.1.2 Aperture photometry

For the following data sets we performed customized aperture measurements on the survey images: *Herschel*/PACS 70, 100, and 160 μ m images from the *Herschel* science archive³, WISE atlas images (Cutri et al. 2011), 2MASS J, H and K_S images from the interactive image service⁴, VISTA/Paranal J, H, and K_S band images from the Cambridge astronomical survey unit⁵, optical *grizy* photometric images⁶ from the Pan-STARRS DR1 (Chambers et al. 2016) and *ugriz* images⁷ from the SDSS-III DR12 (Alam et al. 2015), and GALEX and Swift/UVOT ultraviolet images from the Barbara A. Mikulski Archive for Space Telescopes⁸. The elliptical apertures are defined for each instrument to cover the entire galaxy in the sequence of the bands. The aperture fluxes are computed using the AstroPy Python package PHOTUTILS (Bradley et al. 2020, photutils.readthedocs.io). Since the images of CARS targets are extended at these wavelengths the apertures are not affected by beam smearing and PSF matching as done for higher redshift targets is not a concern for our sample.

³HSA, <http://archives.esac.esa.int/hsa/whsa/>

⁴<https://irsa.ipac.caltech.edu/applications/2MASS/IM/interactive.html>

⁵CASU, <http://casu.ast.cam.ac.uk>

⁶available at <http://ps1images.stsci.edu>

⁷available at <https://dr12.sdss.org/>

⁸MAST, <http://archive.stsci.edu/>

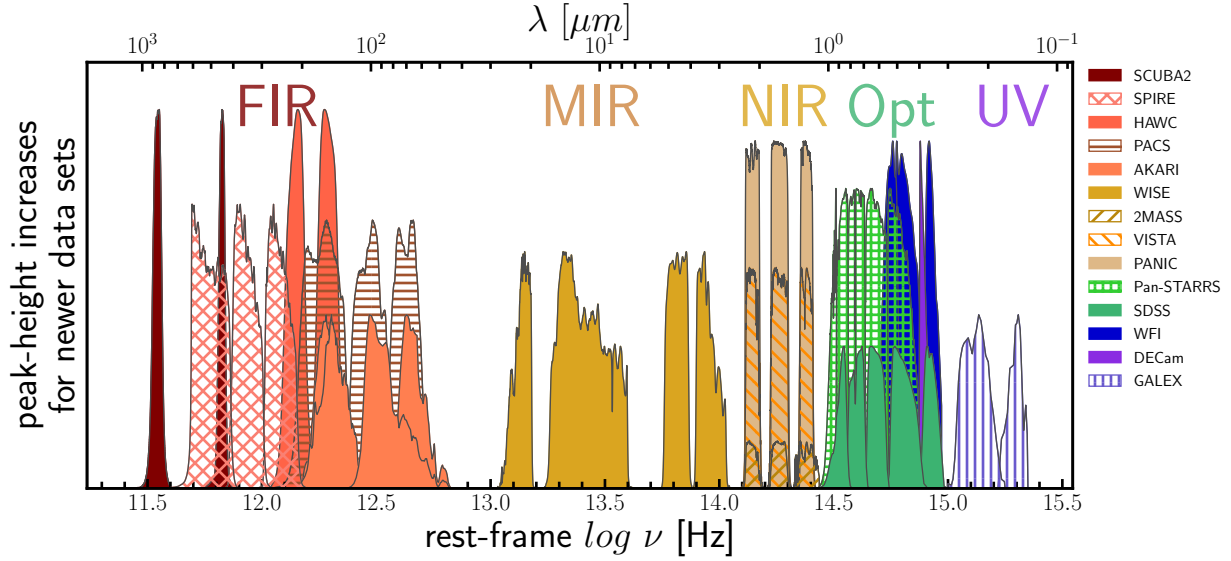


Figure 2.1: Photometric broad bands from a number of surveys and instruments used for the SED modeling. The y -axis is normalized roughly by the year of observational campaign to visually compare bands with similar coverage. When more than one option was available for certain bands, the preference was given to the band sets, which are temporally closer to each other (especially in near infrared and optical ranges) to minimize the impact of AGN variability.

2.2.2 Galactic extinction and AGN broad-line correction

The observed photometry for external galaxies is attenuated by the dust in the Milky Way depending on the specific line-of-sight. We apply an extinction correction to the NIR, optical, and UV photometry of the SED using the Fitzpatrick (1999) Milky Way attenuation curve. The normalization of the attenuation curve is anchored to the measured V band extinction (A_V) along our line-of-sight toward the target is taken from Schlafly & Finkbeiner (2011) and retrieved from the NASA/IPAC Extragalactic Database⁹. All corresponding photometric data in Table 2.1 are provided after extinction correction.

The broad emission lines of unobscured AGN can significantly contribute to broad-band photometry. Because the SED model library used for the fitting assumes smooth power-law for the optical-UV accretion disk component we need to subtract the broad emission line contribution from the photometry. We used the available IFU spectroscopy of the CARS sample to measure $H\beta$ and $H\alpha$ fluxes, and subtract them from the optical bands (mainly g and r). The values presented in Table 2.1 are presented after correction for the BLR contribution.

2.2.3 Dedicated broad-band imaging

Given the lack of available data in some bands for some of the CARS targets, we obtained dedicated observations to fill the missing gaps in our photometry. Optical observations were mainly missing in the u band which Pan-STARRS does not cover and HE 0108–4743 and

⁹NED, <https://ned.ipac.caltech.edu/>

HE 2211–3903 are not covered by SDSS or Pan-STARRS, given their low declination. Therefore, we obtained deep wide-field optical imaging with the Dark Energy Camera (DECam, DePoy et al. 2008) mounted to the 4m Blanco telescope of the Cerro Tololo Inter-American Observatory (CTIO) and with the Wide-Field Imager (WFI, Baade et al. 1999) mounted to the 2.2m telescope of the La Silla observatory. Missing NIR imaging were obtained with the PANoramic Near-Infrared Camera (PANIC, Cárdenas Vázquez et al. 2018) mounted to the 2.2m telescope at the Calar Alto Observatory. Finally, deeper FIR observations were obtained for most of the CARS targets undetected with *Akari* using the High-resolution Airborne Wideband Camera Plus (HAWC+, Harper et al. 2018) aboard the Stratospheric Observatory for Infrared Astronomy and the Submillimetre Common-User Bolometer Array 2 (SCUBA-2, Holland et al. 2013) camera mounted to the James Clark Maxwell Telescope (JCMT). The data characteristics and data reduction of all those new observations are described in more detail below.

2.2.3.1 DECam optical observations

DECam imaging in the u band was obtained for 14 CARS targets during the nights of 1–3 April 2017 as part of the program 2017A-0914 (PI: Grant Tremblay). DECam covers almost 3 sq. degree using a mosaic of 62 $2\text{ k}\times 4\text{ k}$ CCDs with a pixel size of $0.27''$. The total exposure times for each target ranged from 1200 s to 4800 s. The data were automatically reduced by the DECam community pipeline (Valdes et al. 2014) and retrieved from the NOAO archive. Absolute flux calibration for individual images was achieved by comparing detected stars in the field with the photometrically-calibrated SkyMapper DR1 (Wolf et al. 2018) catalog magnitudes.

2.2.3.2 WFI optical observations

WFI imaging in the UBV bands was obtained for HE 0108–4743 and HE 2211–3903 to provide optical photometry given the missing Pan-STARRS and SDSS coverage. The observations were taken during a larger observing run from 18-28 October under program 0100.A-9003 (PI: Bernd Husemann). WFI covers a $34'\times 33'$ FoV using a mosaic of 8 $2\text{ k}\times 4\text{ k}$ CCDs. At the time of observations 2 of the CCDs were broken so that a two-pointing offset scheme plus dithering was used to cover the same field. A total exposure time of 3600s was obtained for the U band.

The images were fully reduced and combined with the latest version of the *theli* pipeline¹⁰ (version 3) (Schirmer 2013). The absolute magnitude zero-point for each combined image was obtained by comparing stellar counts with catalog values from the SkyMapper DR1 and APASS DR1 (Henden et al. 2009) for the UBV bands.

2.2.3.3 PANIC NIR observations

Additional NIR imaging was also obtained with the Panoramic Near-Infrared Camera (PANIC, Cárdenas Vázquez et al. 2018) mounted to the 2.2m telescope at the Calar Alto observatory. Although PANIC consists of 4 Hawaii-2RG detectors only 2 were operational at the time of observations of which only one had nominal performance. 20 CARS targets

¹⁰<https://github.com/schirmermischa/THELI>

Table 2.1: Multiband aperture photometry measurements

Object	GALEX			SDSS/DECAM/PanSTARRS1										WFI		
	FUV [mJy]	NUV [mJy]	u [mJy]	g [mJy]	r [mJy]	i [mJy]	z [mJy]	y [mJy]	U [mJy]	B [mJy]	V [mJy]					
HE 0021-1810	0.17±0.02	0.21±0.02	...	1.4±0.1	2.3±0.2	3.2±0.3	3.6±0.4	4.8±0.5	0.5±0.1					
HE 0021-1819	0.18±0.02	0.25±0.03	...	1.0±0.1	1.6±0.2	2.1±0.2	2.3±0.2	2.9±0.3	0.3±0.0					
HE 0040-1105	0.09±0.01	0.18±0.02	0.62±0.06	1.5±0.1	2.4±0.2	3.4±0.3	4.0±0.4					
HE 0045-2145					
HE 0108-4743	0.69±0.07	1.29±0.13	1.7±0.2	4.9±0.5	8.0±0.8					
HE 0114-0015	0.21±0.02	0.34±0.03	0.68±0.07	1.8±0.2	3.1±0.3	4.3±0.4	5.3±0.5					
HE 0119-0118	0.84±0.02	1.26±0.03	1.66±0.17	3.5±0.3	5.1±0.5	6.9±0.7	8.0±0.8					
HE 0150-0344	0.32±0.03	0.44±0.04	0.65±0.07	1.3±0.1	1.6±0.2	2.1±0.2	2.3±0.2					
HE 0203-0031	1.78±0.18	1.95±0.19	4.61±0.46	9.1±0.9	15.5±1.5	21.6±2.2	26.4±2.6					
HE 0212-0059	0.81±0.08	1.26±0.13	4.66±0.47	17.2±1.7	32.9±3.3	46.3±4.6	58.4±5.8					
HE 0224-2834	0.19±0.02	0.35±0.03	...	2.0±0.2	3.0±0.3	3.9±0.4	4.3±0.4	5.2±0.5	0.7±0.1					
HE 0227-0913	3.23±0.32	4.25±0.43	5.74±0.57	9.4±0.9	14.5±1.5	17.9±1.8	22.1±2.2					
HE 0232-0900	4.46±0.45	5.22±0.52	7.48±0.75	12.0±1.2	16.9±1.7	23.1±2.3	27.4±2.7					
HE 0253-1641	0.14±0.01	0.31±0.03	1.16±0.12	3.1±0.3	5.1±0.5	6.8±0.7	8.3±0.8					
HE 0345+0056	2.79±0.28	4.32±0.43	6.36±0.64	8.3±0.8	9.7±1.0	10.2±1.0	11.5±1.2					
HE 0351+0240	0.86±0.09	1.14±0.11	...	2.0±0.2	3.2±0.3	3.8±0.4	4.3±0.4	5.2±0.5					
HE 0412-0803	0.30±0.03	0.45±0.05	...	4.8±0.5	7.5±0.7	8.2±0.8	9.5±1.0	11.5±1.1	2.1±0.2					
HE 0429-0247	1.6±0.2	2.4±0.2	2.8±0.3	3.1±0.3	3.6±0.4					
HE 0433-1028	4.72±0.47	4.88±0.49	...	10.2±1.0	15.1±1.5	17.5±1.7	20.3±2.0	25.3±2.5	5.3±0.5					
HE 0853-0126	0.32±0.03	0.53±0.05	1.07±0.11	2.1±0.2	3.2±0.3	4.3±0.4	5.1±0.5					
HE 0853+0102	0.15±0.01	0.20±0.02	0.43±0.04	1.2±0.1	1.9±0.2	2.5±0.3	3.1±0.3	3.8±0.4					
HE 0934+0119	0.69±0.07	0.84±0.08	1.79±0.18	2.5±0.3	3.3±0.3	4.0±0.4	3.8±0.4	4.6±0.5					
HE 0949-0122	0.45±0.05	0.71±0.07	2.14±0.21	5.8±0.6	10.7±1.1	12.6±1.3	16.7±1.7					
HE 1011-0403	2.39±0.24	2.86±0.29	2.39±0.24	4.0±0.4	5.3±0.5	6.5±0.6	7.0±0.7	8.5±0.9					
HE 1017-0305	0.65±0.06	0.84±0.08	1.51±0.15	3.1±0.3	5.1±0.5	7.1±0.7	8.6±0.9					
HE 1029-1831	0.61±0.06	1.13±0.11	1.52±0.15	4.0±0.4	6.1±0.6	7.1±0.7	8.2±0.8	10.1±1.0					
HE 1107-0813	1.26±0.13	2.30±0.23	...	5.7±0.6	7.2±0.7	7.9±0.8	8.2±0.8	9.6±1.0					
HE 1108-2813	3.80±0.38	10.9±1.1	16.2±1.6	19.6±2.0	22.8±2.3	26.6±2.7					
HE 1126-0407	1.54±0.15	2.77±0.28	4.16±0.42	6.7±0.7	7.7±0.8	10.8±1.1	10.5±1.1	12.0±1.2					
HE 1237-0504	4.94±0.49	9.47±0.95	...	72.1±7.2	136.8±13.7	189.6±19.0	217.0±21.7	261.6±26.2					
HE 1248-1356	0.49±0.05	0.97±0.10	2.91±0.29	12.2±1.2	21.5±2.2	28.7±2.9	34.7±3.5	41.2±4.1					
HE 1310-1051	1.19±0.12	1.32±0.13	1.42±0.14	3.2±0.3	4.3±0.4	4.7±0.5	5.2±0.5	5.6±0.6					
HE 1330-1013	1.83±0.18	6.5±0.7	11.2±1.1	15.1±1.5	18.2±1.8	22.0±2.2					
HE 1338-1423	1.86±0.19	2.18±0.22	3.26±0.33	6.7±0.7	10.9±1.1	13.2±1.3	15.6±1.6	18.7±1.9					
HE 1353-1917	0.21±0.02	0.50±0.05	0.86±0.09	3.0±0.3	6.3±0.6	7.7±0.8	9.7±1.0	11.4±1.1					
HE 1417-0909	0.54±0.05	0.51±0.05	0.73±0.07	1.1±0.1	1.9±0.2	2.4±0.2	2.6±0.3	3.2±0.3					
HE 2128-0221	0.14±0.01	0.24±0.02	0.49±0.05	0.8±0.1	1.2±0.1	1.6±0.2	1.9±0.2					
HE 2211-3903	0.69±0.07	1.03±0.10	2.6±0.3	4.5±0.5					
HE 2222-0026	0.13±0.01	0.19±0.02	0.35±0.04	0.8±0.1	1.3±0.1	1.9±0.2	2.4±0.2					
HE 2233+0124	0.07±0.01	0.10±0.01	1.07±0.11	1.9±0.2	3.3±0.3	5.2±0.5	6.8±0.7					
HE 2302-0857	1.85±0.18	2.04±0.20	3.25±0.33	6.6±0.7	11.2±1.1	16.5±1.7	20.2±2.0					

Table 2.1: continued.

Object	2MASS/PANIC/VISTA			WISE			Herschel/PACS			
	J [mJy]	H [mJy]	K_s [mJy]	$W1$ [mJy]	$W2$ [mJy]	$W3$ [mJy]	$W4$ [mJy]	$70\mu\text{m}$ [mJy]	$100\mu\text{m}$ [mJy]	$160\mu\text{m}$ [mJy]
HE 0021-1810	5.6±0.6	7.4±0.7	...	4.6±0.5	3.8±0.4	5±0	8±1
HE 0021-1819	3.4±0.3	...	3.6±0.4	2.3±0.2	2.3±0.2	8±1	21±2
HE 0040-1105	5.4±0.5	6.9±0.7	...	5.4±0.5	6.4±0.6	15±2	34±3
HE 0045-2145	15.9±1.6	...	16.2±1.6	13.0±1.3	10.1±1.0	99±10	516±52
HE 0108-4743	18.0±1.8	20.9±2.1	18.9±1.9	16.8±1.7	15.5±1.5	63±6	121±12
HE 0114-0015	6.7±0.7	10.7±1.1	...	6.5±0.7	6.2±0.6	17±2	38±4
HE 0119-0118	11.8±1.2	13.1±1.3	...	14.9±1.5	19.2±1.9	60±6	239±24
HE 0150-0344	2.6±0.3	3.0±0.3	2.8±0.3	2.3±0.2	2.0±0.2	16±2	54±5
HE 0203-0031	31.8±0.8	38.5±1.2	36.3±1.6	31.0±3.1	32.1±3.2	42±4	65±6	77±12
HE 0212-0059	73.0±7.3	81.0±8.1	71.6±7.2	43.3±4.3	31.1±3.1	92±9	242±24	413±21	...	1975±99
HE 0224-2834	5.5±0.5	7.9±0.8	7.5±0.7	10.2±1.0	14.4±1.4	35±3	89±9
HE 0227-0913	27.0±2.7	...	40.4±4.0	43.4±4.3	50.1±5.0	96±10	159±16
HE 0232-0900	35.4±3.5	45.1±4.5	...	44.7±4.5	54.8±5.5	156±16	409±41	1197±26	...	1450±57
HE 0253-1641	11.3±1.1	14.5±1.4	...	12.4±1.2	15.8±1.6	58±6	155±16
HE 0345+0056	...	21.1±2.1	...	58.9±5.9	80.8±8.1	181±18	315±32
HE 0351+0240	...	8.0±0.8	...	9.8±1.0	13.8±1.4	32±3	85±9	186±17
HE 0412-0803	...	16.5±1.7	...	43.1±4.3	66.0±6.6	175±17	386±39	587±19	...	423±51
HE 0429-0247	4.5±0.4	5.8±0.6	...	8.1±0.8	9.9±1.0	15±1	27±3
HE 0433-1028	...	38.6±3.9	...	50.8±5.1	77.6±7.8	239±24	598±60	2474±49	...	2334±47
HE 0853-0126	4.9±0.5	...	6.3±0.6	4.9±0.5	4.2±0.4	11±1	19±2
HE 0853+0102	5.1±0.5	6.8±0.7	7.3±0.7	5.8±0.6	6.0±0.6	9±1	14±1
HE 0934+0119	6.0±0.6	6.9±0.7	8.7±0.9	5.9±0.6	7.7±0.8	25±2	59±6	219±1	248±8	257±9
HE 0949-0122	28.4±0.7	53.3±1.4	96.1±2.3	175.1±17.5	256.3±25.6	490±49	921±92
HE 1011-0403	...	11.0±1.1	...	10.6±1.1	12.7±1.3	34±3	73±7	165±2	209±9	234±10
HE 1017-0305	14.2±1.4	...	10.8±1.1	14.0±1.4	16.1±1.6	36±4	71±7
HE 1029-1831	11.4±1.1	...	14.9±1.5	15.2±1.5	16.5±1.6	86±9	306±31
HE 1107-0813	...	20.9±2.1	26.6±2.7	21.5±2.1	24.7±2.5	30±3	46±5
HE 1108-2813	26.4±2.6	...	33.7±3.4	39.7±4.0	41.2±4.1	127±13	471±47
HE 1126-0407	11.5±1.1	18.9±1.9	28.5±2.8	34.7±3.5	46.1±4.6	98±10	262±26	454±9	...	354±7
HE 1237-0504	415.0±10.5	494.2±13.9	426.5±14.6	241.1±24.1	181.5±18.2	362±36	829±83
HE 1248-1356	43.7±4.4	48.0±4.8	46.2±4.6	28.6±2.9	21.5±2.1	68±7	138±14
HE 1310-1051	6.6±0.7	7.8±0.8	8.8±0.9	10.8±1.1	17.2±1.7	53±5	113±11	95±2	115±8	116±11
HE 1330-1013	26.8±2.7	33.7±3.4	29.4±2.9	16.2±1.6	12.1±1.2	23±2	50±5
HE 1338-1423	21.5±2.1	26.7±2.7	28.0±2.8	27.0±2.7	33.3±3.3	78±8	149±15	141±18
HE 1353-1917	15.3±1.5	20.5±2.1	20.9±2.1	14.1±1.4	13.2±1.3	34±3	73±7	246±5	...	768±15
HE 1417-0909	3.4±0.3	3.9±0.4	4.2±0.4	4.3±0.4	5.5±0.6	13±1	28±3
HE 2128-0221	2.5±0.3	3.2±0.3	3.4±0.3	3.2±0.3	3.9±0.4	10±1	22±2
HE 2211-3903	...	15.3±1.5	37.0±3.7	58.2±5.8	83.1±8.3	188±19	371±37
HE 2222-0026	3.1±0.3	4.6±0.5	...	5.0±0.5	6.4±0.6	13±1	21±2
HE 2233+0124	8.2±0.8	10.9±1.1	...	11.4±1.1	11.3±1.1	13±1	14±1
HE 2302-0857	43.0±4.3	53.0±5.3	...	75.1±7.5	87.0±8.7	114±11	239±24	441±9	...	641±13

Table 2.1: continued.

Object	AKARI			SOFIA			Herschel/SPIRE			JWST/SCUBA2	
	N60 [mJy]	WIDE-S [mJy]	WIDE-L [mJy]	N160 [mJy]	D band [mJy]	E band [mJy]	250 μ m [mJy]	350 μ m [mJy]	500 μ m [mJy]	450 μ m [mJy]	850 μ m [mJy]
HE 0021-1810	<296
HE 0021-1819	228 \pm 23
HE 0040-1105	<873	<76	<5
HE 0045-2145	3130 \pm 82	3904 \pm 103	3518 \pm 391	4134 \pm 954	<239	12 \pm 6
HE 0108-4743	<450	1006 \pm 71	3778 \pm 328	2245 \pm 979
HE 0114-0015	214 \pm 17	86 \pm 16
HE 0119-0118	...	1411 \pm 98	1879 \pm 605	<1917	573 \pm 23	198 \pm 20	66 \pm 22
HE 0150-0344	<330	720 \pm 65	<1445	<1261	293 \pm 21	108 \pm 23
HE 0203-0031	82 \pm 16	72 \pm 16
HE 0212-0059	<701	747 \pm 69	2648 \pm 929	612 \pm 37	349 \pm 31	186 \pm 21
HE 0224-2834
HE 0227-0913	<989	455 \pm 85	<1072	407 \pm 41	<270	<12
HE 0232-0900	...	1291 \pm 16	2204 \pm 389	699 \pm 21	356 \pm 24	144 \pm 28
HE 0253-1641	661 \pm 66
HE 0345+0056
HE 0351+0240	<129	<9
HE 0412-0803	<105	<8
HE 0429-0247	<445
HE 0433-1028	...	2572 \pm 103	<4505	1102 \pm 20	496 \pm 26	204 \pm 18
HE 0853-0126
HE 0853+0102	100 \pm 11
HE 0934+0119	<229	<10
HE 0949-0122	...	1375 \pm 164
HE 1011-0403	126 \pm 12	51 \pm 12
HE 1017-0305	<323	<10
HE 1029-1831	2134 \pm 407	2596 \pm 93	3535 \pm 984	<331	15 \pm 7
HE 1107-0813
HE 1108-2813	3203 \pm 109	3330 \pm 174	191 \pm 120	14 \pm 6	...
HE 1126-0407	...	484 \pm 30	...	<1163	198 \pm 14	80 \pm 15
HE 1237-0504	2659 \pm 345	2926 \pm 174	5120 \pm 423	4676 \pm 808
HE 1248-1356	...	972 \pm 100	2409 \pm 1520	<172	10 \pm 6	...
HE 1310-1051	61 \pm 11
HE 1330-1013	<137	6 \pm 4
HE 1338-1423	127 \pm 18	83 \pm 16
HE 1353-1917	...	<585	444 \pm 52	216 \pm 32	85 \pm 16
HE 1417-0909
HE 2128-0221	<457
HE 2211-3903	...	657 \pm 70
HE 2222-0026
HE 2233+0124	<527
HE 2302-0857	...	647 \pm 119	282 \pm 14

were observed as part of programmes F17-2.2-014 and H17-2.2-008 (PI: Bernd Husemann). For the first program only the best performing chip was used covering a FoV of $15' \times 15'$. For the second program a mosaic strategy was used to cover the nominal $30' \times 30'$ with the two operational detectors. The sampling of PANIC is $0''45$ per pixel. For the analysis in this chapter we only use a small part of the images covering the AGN host galaxies so that the full FoV is not relevant.

Total exposure times ranged from 1–2 hours for the J, H, and Ks bands, but not all NIR bands could be obtained for all the targets. A spiral dither pattern was used along all observations for background subtraction, excluding satellite tracks and image cosmetics. The PANIC exposures were reduced and combined with the dedicated PANIC pipeline¹¹. The astrometric registration and absolute photometry was further optimized with the PhotometryPipeline (PP, Mommert 2017) software package using 2MASS as photometric reference.

2.2.3.4 SCUBA-2 FIR observations

SCUBA-2 is a 10 000 pixel bolometer camera simultaneously operating at $450 \mu\text{m}$ and $850 \mu\text{m}$ and covering an area of 41 arcmin^2 on the sky (Holland et al. 2013). Effective beam sizes are $10''$ and $15''$ at $450 \mu\text{m}$ and $850 \mu\text{m}$, respectively.

Given the angular size of our AGN hosts on the sky, we observe using the "constant velocity (CV) Daisy" mapping mode which provides uniform sensitivity in the central $3'$ of the observation. The "CV Daisy" is a circular scanning pattern designed so that the target is always within the field-of-view of the array throughout the integration while moving at a constant $155''/\text{s}$. The observation provides usable coverage out to $\sim 6.0'$ in radius, but beyond a radius of $1.5'$ the map sensitivity decreases rapidly.

The observations were performed in service mode between February and December 2019 during grade 3 weather conditions ($0.08 < \tau_{225} < 0.12$) as part of project M19AP019 (PI: Timothy Davis). On-source exposure times ranged from 1 h to 7.5 h. The resulting maps were reduced using the Dynamic Iterative Map Maker (DIMM) within the sub-mm user reduction facility (SMURF, Chapin et al. 2013). For a full overview of the procedure see Chapin et al. (2013).

The data were reduced using the blank field reduction in order to detect point sources within the map. The maps were then calibrated using the standard flux calibration factors of $\text{FCF}_{450} = 491 \text{ Jy beam}^{-1} \text{pW}^{-1}$ and $\text{FCF}_{850} = 537 \text{ Jy beam}^{-1} \text{pW}^{-1}$ (Dempsey et al. 2013). To improve the point source detection, a matched filter was applied to the maps. This matched filtering caused a $\sim 10\%$ loss in flux (determined by inserting artificial sources into the map and comparing the flux before and after), so an additional 10% was applied to the FCFs to account for this.

2.2.3.5 SOFIA HAWC+ FIR observations

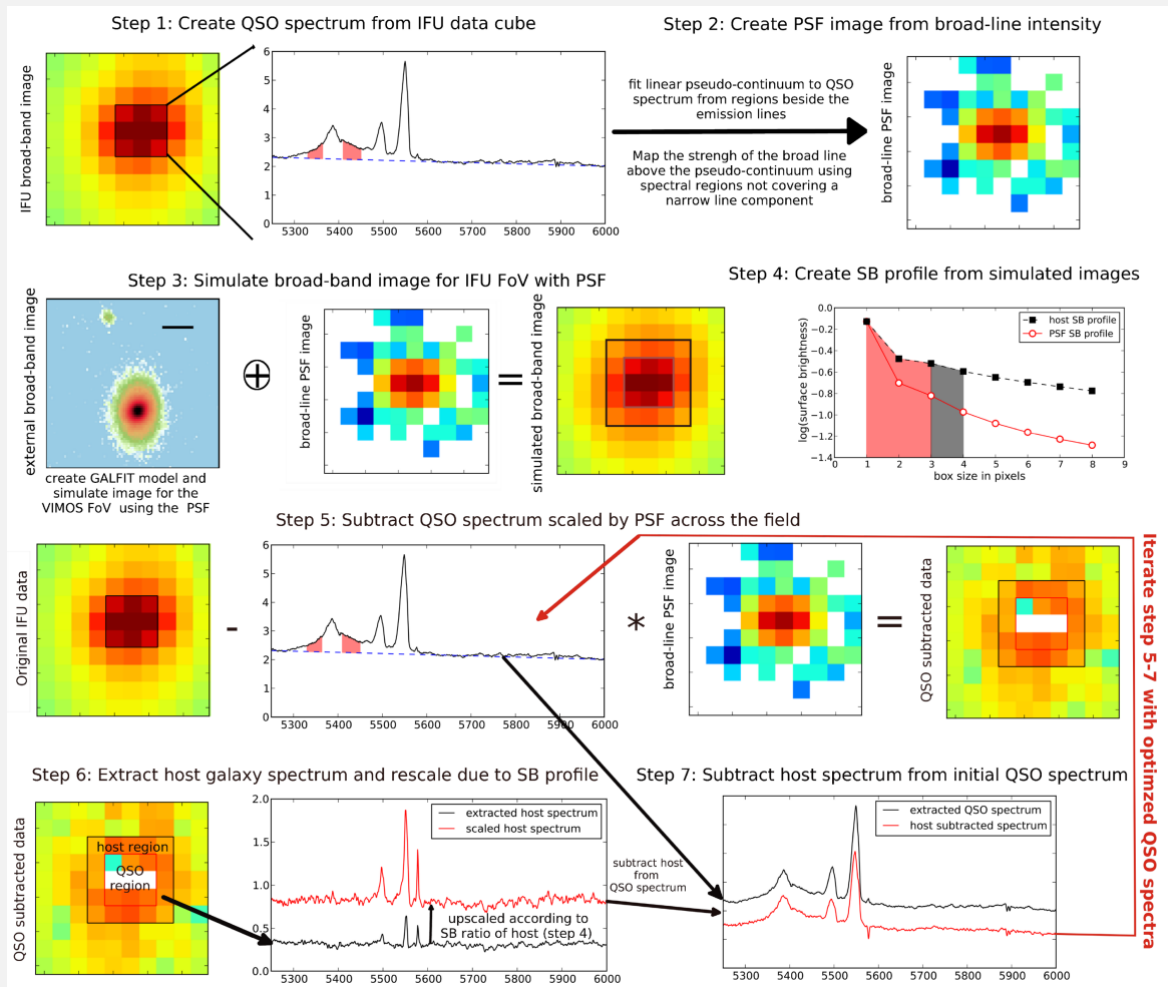
The HAWC+ FIR camera (Harper et al. 2018) aboard SOFIA was used to obtain FIR photometry for CARS targets that could not be detected with all-sky *Akari* FIR survey and that were not targeted with *Herschel*. Observations were taken for 8 out of 11 proposed targets as part of a SOFIA survey program (Plan ID: 07_193, PI: Bernd Husemann) with

¹¹<https://github.com/ppmim/PAPI>

exposure times ranging from 15 min to 60 min. HE 0227–0913 was observed in the E band ($214\ \mu\text{m}$) while all other targets were observed in the D band ($154\ \mu\text{m}$). The FWHM of the HAWC+ beam is $18''.2$ and $13''.5$ for the E and D band, respectively. All data were reduced by the HAWC+ SOFIA team using a dedicated instrument pipeline. The pipeline was run specifically with the faint object flag to account for the faint signal in our targets.

QDEBLEND^{3D}

The IFU data analysis in this thesis is dependant on the two extra pre-analysis steps after the standard data reduction: deblending the unobscured AGN emission from the host galaxy with the QDEBLEND^{3D} tool; and the following step of fitting the spectra with the PYPARADISE tool, described in the next box on page 34.



An example of QDEBLEND^{3D} analysis steps for the VIMOS observations of HE 0952–1552. The figure is taken from Husemann et al. (2014).

Studying the properties of QSO host galaxies, and type 1 AGN hosts in general, requires an accurate decomposition of the AGN and host galaxy light. The three-dimensional nature of the IFU data allows this deblending to be done in the spatial

and spectral dimensions. Husemann et al. (2013, 2014) presents a dedicated software tool `QDEBLEND3D` for this task. The algorithm uses the fact that the broad-line region of an AGN is appearing as a point-like source given its compact size $< 1\text{pc}$. Thus, a point-spread function (PSF) can be easily computed and used to deblend point-like and extended emission. The basic concept is that the spectrum in each spaxel is a superposition of the host galaxy spectrum at this position and of the AGN spectrum modulated in absolute flux according to the PSF of the observation. However, significant over-subtraction will occur when the nuclear QSO spectrum is contaminated by host galaxy light. In `QDEBLEND3D` this host galaxy contamination is minimized by iterative estimation of a mean host galaxy spectrum from the residual datacube that is subsequently subtracted from the QSO spectrum. The example of the algorithm steps is shown on the figure above. The material of this box is taken from Husemann et al. (2013, 2014); the `QDEBLEND3D` tool is available at <https://git.io/qdeblend3d/>.

2.2.4 Integral-field spectroscopy observations

IFU observations for the CARS sample were mainly obtained with the MUSE instrument at the Very Large Telescope (VLT) (Bacon et al. 2010) for 37 targets under programs 094.B-0345(A), 095.B-0015(A), 099.B-0242(A), and 099.B-0249(B), with the VIMOS instrument at the VLT (Le Fèvre et al. 2003) for 2 targets under program 083.B-0801(A), and with the PMAS instrument at the 3.5m Calar Alto telescope (Roth et al. 2005) for 2 targets under program H18-3.5-010. MUSE covers a $1' \times 1'$ FoV at a sampling of $0''.2$, VIMOS covers a $27'' \times 27''$ FoV at a sampling of $0''.67$ and PMAS covers a $16'' \times 16''$ FoV with a sampling of $1''$. All details of the IFU observations and their data reduction are presented in Husemann et al. (2022).

For the present chapter, we are working with emission line maps that were created after the AGN point-like emission was removed from the reconstructed IFU datacube (see `QDEBLEND3D` box on page 30). Emission-line fluxes are extracted by fitting Gaussian profiles after modeling and subtracting the stellar continuum (see `PYPARADISE` box on page 34) from the AGN-subtracted data. All the details of this process and its application to the CARS IFU data are presented in Husemann et al. (2022). For the analysis presented in this chapter we use the 2D emission line maps of $[\text{O III}]\lambda 5007$, $\text{H}\beta$, $[\text{N II}]\lambda 6583$, $\text{H}\alpha$, $[\text{S II}]\lambda\lambda 6716, 6731$ and their associated errors. All those data are also accessible from the CARS data release 1 at <http://cars.aip.de>.

2.3 Analysis

2.3.1 Modeling the panchromatic SED

In order to infer primary physical parameters such as the stellar mass M_\star or the SFR, we need to model the panchromatic SED constructed for all the sources. We decided to perform the SED fitting with the publicly available `AGNFITTER` package (Calistro Rivera et al. 2016). `AGNFITTER` models the observed photometry as a super-position of various

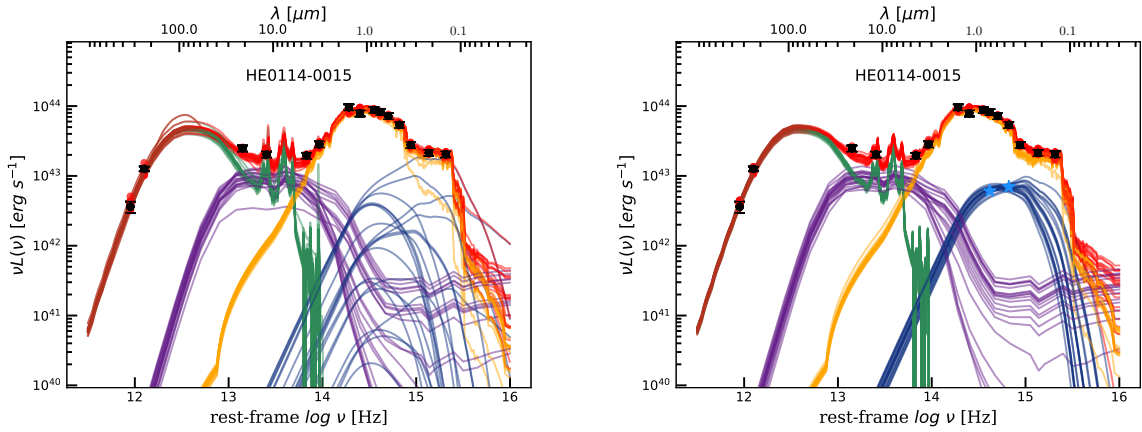


Figure 2.2: SED for HE 0114–0015 and the best-fit model determined by AGNFITTER (Calistro Rivera et al. 2016). 20 MCMC realizations of the SED model are shown for the broadband photometric data (black points with error bars) where the red points are the corresponding predictions from the model. The red lines represent the total model, which consists of four components: the cold and warm dust in star-forming regions (green lines), the torus of AGN-heated dust (purple lines), the stellar continuum (yellow lines), and the AGN accretion disk (blue lines). On the right panel is an additional constraint to the accretion disk model (e.g., g and i AGN photometry is included).

template libraries for the stellar continuum, the AGN accretion disk emission, AGN-heated dust emission from the torus and the cold dust emission excited by star formation.

The stellar library is taken from Bruzual & Charlot (2003) and parametrized by a stellar age of the galaxy and an exponential decay time of the starburst τ which can be further modified by reddening and normalized in absolute flux. The accretion disk emission is represented by an empirical composite spectrum generated from 259 type-1 AGN from the Sloan Digital Sky Survey (SDSS, York et al. 2000), which can be de-reddened using the Small Magellanic Cloud reddening law of Prevot et al. (1984). This leaves the flux normalization and the reddening as the only two free parameters for this component. The hot dust component of the AGN is reconstructed from the empirical SED library collected by Silva et al. (2004) based on photometric observations of AGN that were modeled with the radiative transfer code GRASIL Silva et al. (1998) to obtain the full NIR SEDs. The library is divided in a range of absorbing neutral hydrogen column densities N_H through the torus along our line-of-sight as the main free parameter in addition to the normalization. Semi-empirical starburst template spectra from Chary & Elbaz (2001) and Dale & Helou (2002) are used to model the cold dust component from star formation which are denoted by a luminosity parameter and can be normalized.

AGNFITTER uses the `emcee` package (Foreman-Mackey et al. 2013) for an affine-invariant Markov-Chain Monte Carlo (MCMC) ensemble sampling to explore the 10-dimensional parameter space associated with the underlying template library of spectra. The advantage of AGNFITTER is that it natively accepts upper limits in the photometry, allows to set priors on parameters and additional constraints can be incorporated easily to break degeneracies. Particularly, one big issue in the SED modeling of luminous type 1 AGN is that the accretion disk model is competing with the stellar population model in the UV–optical

Table 2.2: AGN host galaxy properties inferred from SED modeling

Object	z^a	$\log\left(\frac{M_*}{[M_\odot]}\right)^b$	$\log\left(\frac{L_{\text{tor}}}{[\text{erg s}^{-1}]}\right)^c$	$\log\left(\frac{L_{42.5-122.5\mu\text{m}}}{[\text{erg s}^{-1}]}\right)^d$	$\log\left(\frac{L_{8-1000\mu\text{m}}}{[\text{erg s}^{-1}]}\right)^e$	SFR _{IR} ^f	$\log\left(\frac{L_{\text{CO}}}{[\text{K kms}^{-1}\text{pc}^2]}\right)^g$
HE0021-1810	0.054	10.64 ^{+0.04} _{-0.05}	43.02 ^{+0.07} _{-0.19}	<43.67	<43.98	<3.7	< 6.8
HE0021-1819	0.053	10.50 ^{+0.04} _{-0.05}	42.82 ^{+0.16} _{-0.59}	43.76 ^{+0.05} _{-0.04}	44.04 ^{+0.05} _{-0.04}	4.2 ^{+0.6} _{-0.3}	7.6 ± 2.1
HE0040-1105	0.042	10.16 ^{+0.13} _{-0.10}	43.50 ^{+0.05} _{-0.04}	<43.82	<44.03	<4.1	7.7 ± 1.7
HE0045-2145	0.021	9.36 ^{+0.03} _{-0.02}	...	44.18 ^{+0.01} _{-0.01}	44.45 ^{+0.01} _{-0.01}	10.9 ^{+0.2} _{-0.2}	8.1 ± 0.4
HE0108-4743	0.024	9.77 ^{+0.18} _{-0.10}	43.12 ^{+0.07} _{-0.08}	43.67 ^{+0.02} _{-0.02}	44.04 ^{+0.02} _{-0.02}	4.3 ^{+0.2} _{-0.2}	7.6 ± 0.6
HE0114-0015	0.046	10.47 ^{+0.13} _{-0.19}	43.26 ^{+0.10} _{-0.09}	43.74 ^{+0.03} _{-0.03}	44.02 ^{+0.03} _{-0.03}	4.0 ^{+0.3} _{-0.3}	7.8 ± 2.9
HE0119-0118	0.055	10.91 ^{+0.02} _{-0.06}	43.76 ^{+0.10} _{-0.24}	44.65 ^{+0.01} _{-0.02}	44.89 ^{+0.01} _{-0.02}	30.4 ^{+1.0} _{-1.1}	8.4 ± 0.8
HE0150-0344	0.048	9.57 ^{+0.12} _{-0.09}	...	44.10 ^{+0.02} _{-0.02}	44.36 ^{+0.02} _{-0.02}	9.0 ^{+0.4} _{-0.4}	7.8 ± 3.4
HE0203-0031	0.043	10.88 ^{+0.02} _{-0.02}	43.90 ^{+0.04} _{-0.07}	43.00 ^{+0.08} _{-0.09}	43.34 ^{+0.06} _{-0.09}	0.8 ^{+0.1} _{-0.2}	< 7.0
HE0212-0059	0.026	10.59 ^{+0.01} _{-0.01}	...	43.54 ^{+0.01} _{-0.02}	43.87 ^{+0.01} _{-0.01}	2.9 ^{+0.1} _{-0.1}	7.9 ± 0.6
HE0224-2834	0.060	10.13 ^{+0.19} _{-0.17}	44.27 ^{+0.04} _{-0.03}	<44.06	<44.38	<9.3	7.9 ± 3.2
HE0227-0913	0.016	9.92 ^{+0.17} _{-0.12}	43.44 ^{+0.05} _{-0.05}	42.85 ^{+0.11} _{-0.10}	43.16 ^{+0.10} _{-0.08}	0.6 ^{+0.1} _{-0.1}	7.2 ± 1.9
HE0232-0900	0.043	10.88 ^{+0.23} _{-0.12}	44.45 ^{+0.06} _{-0.04}	44.31 ^{+0.01} _{-0.01}	44.59 ^{+0.01} _{-0.01}	14.9 ^{+0.2} _{-0.2}	8.6 ± 1.0
HE0253-1641	0.032	10.28 ^{+0.11} _{-0.24}	42.76 ^{+0.54} _{-1.39}	44.17 ^{+0.04} _{-0.05}	44.41 ^{+0.04} _{-0.05}	10.0 ^{+0.9} _{-1.2}	8.0 ± 1.1
HE0345+0056	0.031	8.85 ^{+0.62} _{-0.26}	44.42 ^{+0.03} _{-0.03}	<43.84	<44.13	<5.2	< 6.7
HE0351+0240	0.035	9.85 ^{+0.34} _{-0.70}	43.75 ^{+0.04} _{-0.04}	43.28 ^{+0.04} _{-0.05}	43.56 ^{+0.05} _{-0.05}	1.4 ^{+0.2} _{-0.1}	< 6.9
HE0412-0803	0.038	10.08 ^{+0.10} _{-0.12}	44.57 ^{+0.02} _{-0.03}	43.78 ^{+0.02} _{-0.02}	44.04 ^{+0.02} _{-0.04}	4.2 ^{+0.2} _{-0.3}	< 6.8
HE0429-0247	0.042	9.18 ^{+0.51} _{-0.10}	43.55 ^{+0.03} _{-0.05}	<44.10	<44.43	<10.5	< 7.3
HE0433-1028	0.036	10.80 ^{+0.08} _{-0.09}	44.55 ^{+0.03} _{-0.03}	44.43 ^{+0.00} _{-0.00}	44.70 ^{+0.00} _{-0.00}	19.4 ^{+0.2} _{-0.2}	8.6 ± 0.6
HE0853-0126	0.060	10.32 ^{+0.06} _{-0.08}	43.54 ^{+0.07} _{-0.24}	<44.05	<44.42	<10.1	8.2 ± 2.4
HE0853+0102	0.053	10.54 ^{+0.04} _{-0.10}	43.31 ^{+0.08} _{-0.05}	43.16 ^{+0.09} _{-0.30}	43.51 ^{+0.08} _{-0.20}	1.3 ^{+0.3} _{-0.5}	< 7.2
HE0934+0119	0.051	10.13 ^{+0.25} _{-0.31}	43.75 ^{+0.05} _{-0.05}	43.71 ^{+0.00} _{-0.01}	43.98 ^{+0.00} _{-0.01}	3.7 ^{+0.0} _{-0.0}	< 7.0
HE0949-0122	0.020	10.02 ^{+0.09} _{-0.31}	44.54 ^{+0.02} _{-0.02}	43.45 ^{+0.07} _{-0.10}	43.74 ^{+0.10} _{-0.09}	2.1 ^{+0.5} _{-0.4}	7.2 ± 2.3
HE1011-0403	0.059	10.74 ^{+0.07} _{-0.17}	44.16 ^{+0.04} _{-0.03}	43.69 ^{+0.01} _{-0.01}	43.98 ^{+0.01} _{-0.01}	3.7 ^{+0.1} _{-0.1}	8.2 ± 1.8
HE1017-0305	0.049	10.93 ^{+0.10} _{-0.15}	44.06 ^{+0.05} _{-0.05}	<44.10	<44.45	<11.0	8.0 ± 1.6
HE1029-1831	0.041	10.49 ^{+0.06} _{-0.18}	43.89 ^{+0.05} _{-0.08}	44.57 ^{+0.01} _{-0.02}	44.84 ^{+0.01} _{-0.02}	27.1 ^{+0.8} _{-1.3}	8.4 ± 1.0
HE1107-0813	0.059	11.17 ^{+0.20} _{-0.38}	43.78 ^{+0.17} _{-1.34}	<44.46	<44.87	<28.6	8.0 ± 2.5
HE1108-2813	0.024	10.29 ^{+0.11} _{-0.05}	43.74 ^{+0.07} _{-0.09}	44.24 ^{+0.01} _{-0.01}	44.50 ^{+0.02} _{-0.01}	12.4 ^{+0.4} _{-0.4}	8.2 ± 0.7
HE1126-0407	0.060	10.59 ^{+0.37} _{-0.46}	44.73 ^{+0.03} _{-0.04}	44.15 ^{+0.01} _{-0.01}	44.42 ^{+0.01} _{-0.01}	10.2 ^{+0.2} _{-0.1}	8.2 ± 2.0
HE1237-0504	0.008	10.92 ^{+0.01} _{-0.01}	43.12 ^{+0.06} _{-0.06}	43.26 ^{+0.03} _{-0.02}	43.58 ^{+0.02} _{-0.03}	1.5 ^{+0.1} _{-0.1}	7.2 ± 1.5
HE1248-1356	0.015	10.31 ^{+0.01} _{-0.01}	42.65 ^{+0.10} _{-0.16}	43.22 ^{+0.06} _{-0.07}	43.49 ^{+0.05} _{-0.06}	1.2 ^{+0.1} _{-0.2}	7.3 ± 1.1
HE1310-1051	0.034	10.35 ^{+0.06} _{-0.18}	43.90 ^{+0.02} _{-0.02}	42.87 ^{+0.02} _{-0.02}	43.17 ^{+0.02} _{-0.02}	0.6 ^{+0.0} _{-0.0}	< 6.8
HE1330-1013	0.022	10.69 ^{+0.03} _{-0.13}	42.93 ^{+0.10} _{-0.49}	<43.69	<43.89	<3.0	7.5 ± 1.8
HE1338-1423	0.041	11.02 ^{+0.06} _{-0.20}	44.24 ^{+0.03} _{-0.05}	43.18 ^{+0.06} _{-0.08}	43.52 ^{+0.05} _{-0.07}	1.3 ^{+0.2} _{-0.2}	< 6.9
HE1353-1917	0.035	10.99 ^{+0.03} _{-0.06}	43.37 ^{+0.07} _{-0.07}	43.50 ^{+0.01} _{-0.01}	43.86 ^{+0.01} _{-0.01}	2.8 ^{+0.1} _{-0.1}	8.1 ± 1.4
HE1417-0909	0.044	10.23 ^{+0.10} _{-0.17}	43.54 ^{+0.04} _{-0.05}	<43.39	<43.67	<1.8	< 6.7
HE2128-0221	0.053	9.93 ^{+0.21} _{-0.67}	43.58 ^{+0.04} _{-0.05}	<43.75	<44.02	<4.0	< 6.9
HE2211-3903	0.040	9.83 ^{+0.22} _{-0.21}	44.64 ^{+0.02} _{-0.03}	43.84 ^{+0.06} _{-0.05}	44.16 ^{+0.07} _{-0.08}	5.6 ^{+0.9} _{-1.0}	8.0 ± 1.2
HE2222-0026	0.058	10.20 ^{+0.09} _{-0.15}	43.81 ^{+0.02} _{-0.04}	<44.11	<44.46	<11.2	7.4 ± 3.9
HE2233+0124	0.057	10.71 ^{+0.10} _{-0.03}	41.55 ^{+0.71} _{-0.58}	43.84 ^{+0.03} _{-0.05}	44.22 ^{+0.03} _{-0.05}	6.4 ^{+0.4} _{-0.6}	8.0 ± 1.8
HE2302-0857	0.047	11.20 ^{+0.09} _{-0.13}	44.31 ^{+0.06} _{-0.06}	43.96 ^{+0.01} _{-0.01}	44.24 ^{+0.01} _{-0.01}	6.7 ^{+0.1} _{-0.1}	8.2 ± 1.4

^a Redshift directly measured from the CARS IFU data as reported in Husemann et al. (2022).

^b Stellar masses and 1σ uncertainties from stellar template fitting reported by AGNFITTER.

^c Integrated luminosity of the torus template reported by AGNFITTER.

^d Luminosity of the matched star-forming IR template reported by AGNFITTER integrated over the 42.5-122.5 μm wavelength range.

^e Same as (d) but integrated over the full 8-1000 μm wavelength range.

^f Estimated SFR based on $L_{8-1000\mu\text{m}}$ using calibration of Murphy et al. (2011), see Eq. 2.1.

^g CO(1-0) line luminosity based on the flux measurements from Bertram et al. (2007) and listed in Husemann et al. (2022).

rest-frame wavelength regime. This leads to a degeneracy between the accretion disk and stellar continuum model when fitting the observed integrated broad-band photometry as shown in Fig. 2.2 (left panel).

This degeneracy could be solved by linking the UV radiation field with the corresponding re-emission in the IR as an additional constraint implemented for example in the CIGALE or MAGPHYS SED fitting codes. However, this method requires an assumption of the UV escape fractions and dust content of the galaxies, which can be very different for starburst galaxies and AGN-dominated galaxies. Due to the low redshift of the CARS sample, it is possible to spatially separate the AGN and host galaxy light using 2D image synthesis modeling even in ground-based images. This allows us to obtain direct measurements for the AGN brightness in the optical bands. The AGN magnitudes in the g and i bands are obtained by modeling the ground-based images as a super-position of two Sersic profiles and a point source for the AGN with the `galfit` package (Peng et al. 2002, 2010) as described in Husemann et al. (2022). Hence, we adjusted the likelihood function within the AGNFITTER code to consider these additional photometric data as constraints solely for the AGN accretion disk component model. The effectiveness of this approach is shown in Fig. 2.2 in comparison to the modeling without those additional AGN constraints.

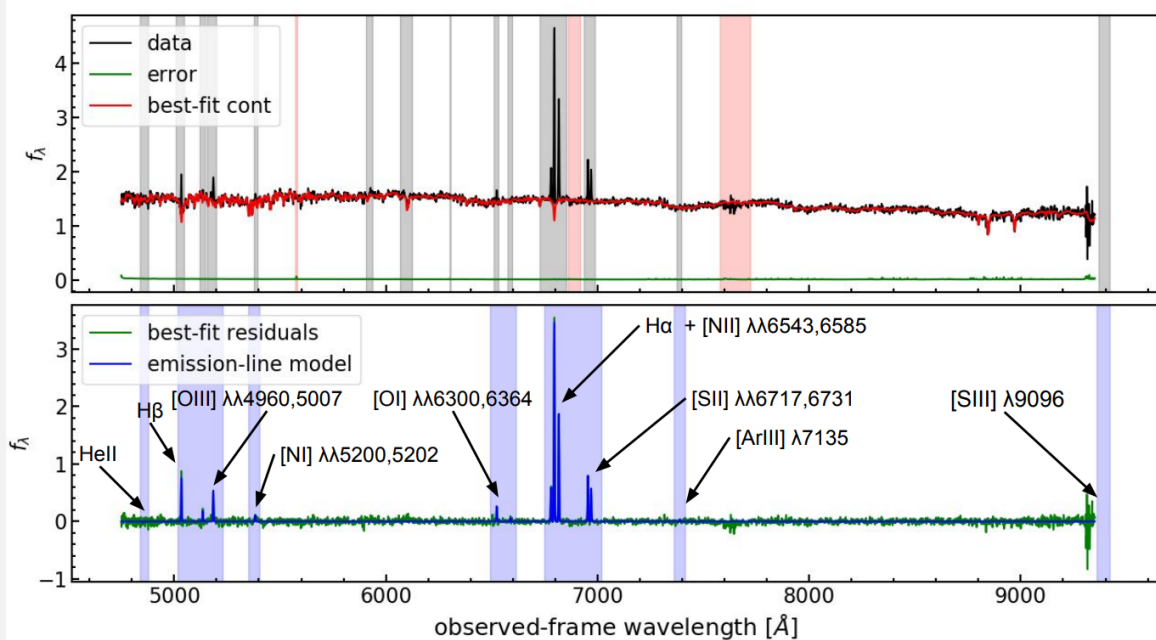
With the additional photometric constraints we reduced the uncertainties of the various physical quantities that are directly computed by AGNFITTER from the posterior parameter distribution. For our work we are most interested in the stellar mass M_\star that are based on the stellar population model and its associated luminosity normalization. In addition we report the integrated luminosity of the torus model (L_{tor}), and the luminosities of the cold dust component integrated between entire IR 8–1000 μm ($L_{8-1000\mu\text{m}}$) wavelength range and a restricted range of 42.5–122.5 μm ($L_{42.5-122.5\mu\text{m}}$) for literature comparisons. AGNFITTER estimates a SFR from the integrated IR luminosity using the calibration established by Murphy et al. (2011):

$$\left(\frac{\text{SFR}_{\text{IR}}}{[\text{M}_\odot \text{yr}^{-1}]} \right) = 3.88 \times 10^{-44} \left(\frac{L_{8-1000\mu\text{m}}}{[\text{erg s}^{-1}]} \right). \quad (2.1)$$

In cases where the cold dust SED is not well constrained due to upper limits in the FIR photometry, we determine 5σ upper limits from the posterior distribution function of the integrated luminosities and SFR. We list all the inferred parameters from SED fitting as described above in Table 2.2 and all the corresponding SED models with AGNFITTER are shown in Fig. A.2 of the Appendix A.1.

PYPARADISE

Before the analysis of the $\text{H}\alpha$ emission line is described further in the thesis it is necessary to provide the information box of the second pre-analysis step for the CARS IFU data. PYPARADISE is the tool that performs stellar population synthesis modelling of the stellar continuum and subsequent emission lines fitting for galaxy spectra.



Example of the full spectral modeling using PYPARADISE for one binned spectrum of HE 0433–1028. The figure is taken from Husemann et al. (2022)

After the QSO subtraction, the CARS team infers maps of the stellar and ionized gas properties across the host galaxies with the PYPARADISE tool (described in Husemann et al. 2016a; Weaver et al. 2018; Husemann et al. 2022), an extended Python version of the PARADISE code (Walcher et al. 2015). The SNR of individual spaxels in the IFU data can be too low to properly model the stellar continuum and low surface brightness emission line regions. With PYPARADISE two different binning strategies are applied. For bright emission line regions it is best to retain the native MUSE spatial sampling of $0''.2$ for which the SNR in the stellar continuum may not be sufficient for the continuum modeling. An initial Voronoi binning is therefore performed to achieve a minimum continuum SNR of 20 per Voronoi cell. Then the binned stellar continuum spectra are modelled with PYPARADISE using stellar spectra from the Indo-US spectra library (Valdes et al. 2004) and the inferred stellar kinematics are remapped back to the native MUSE sampling grid. Afterwards, the stellar continuum in the full cube is modelled while keeping the stellar kinematics fixed, so that the emission lines can be fitted to the residual continuum spectra for each individual MUSE spectra. Additionally, we bin the QSO-subtracted datacube by 8×8 pixels for MUSE, 2×2 pixels for PMAS, and 4×4 pixels for VIMOS corresponding to a binned sampling of $1''.6$, $2''.0$, and $2''.64$, respectively. The analysis of the binned data allows us to trace the emission lines nearly an order of magnitude fainter in surface brightness than in the unbinned data. Errors on the stellar kinematics are inferred using an MCMC approach as part of PYPARADISE iterative continuum modeling. The errors on all emission-line parameters are inferred combining a bootstrapping and Monte-Carlo approach. The material of this box is taken from Husemann et al. (2022); PYPARADISE is available at <https://git.io/pyparadise>.

2.3.2 Measuring H α -based SFR

The IFU observations for the CARS sample as presented in Husemann et al. (2022) are well suited to measure the current star formation rate of the host galaxies in comparison to the FIR-based SFR. Various calibrations have been determined to convert the extinction-corrected H α luminosity into a SFR from which we use the calibration of Calzetti et al. (2007)

$$\left(\frac{\text{SFR}_{\text{H}\alpha}}{[M_{\odot} \text{ yr}^{-1}]} \right) = 5.3 \times 10^{-42} \left(\frac{L_{\text{H}\alpha}}{[\text{erg s}^{-1}]} \right) \quad (2.2)$$

to estimate the integrated SFR based on the integrated H α . However, not all of the H α emission is associated with star-forming H II regions in AGN host galaxies. A detailed spatially resolved emission line diagnostic analysis is therefore essential for AGN host galaxies to separate the contribution from AGN photoionization and star-forming H II regions to the excitation of H α .

In order to provide reliable H α -based SFR estimates, we use a combination of line maps from pixel-by-pixel and binned IFU cubes after subtracting the AGN point-source emission as described in Husemann et al. (2022) in more detail. While the pixel-by-pixel maps provide high-spatial resolution information for bright emission line regions, the binned maps provide higher signal-to-noise ratio (SNR) information on the more extended ionized gas. We only consider the diagnostic lines H α , H β , [N II] and [O III] as detected above a 3σ level. For the maps we also include the weaker spaxels where only H α SNR is required to be more than 3.

Here, we consider several ways to correct the H α flux by the AGN contribution as described in more detail in the following subsections. All those methods leverage the potential of the IFU data to perform flexible spatially resolved emission-line diagnostics that open possibilities for de-contamination compared to traditional narrow-band imaging or long-slit spectroscopy.

2.3.2.1 Demarcation lines

The simplest approach to correct for the AGN affected H α emission is to ignore those spaxels displaying AGN ionization and integrate only the H α flux from regions clearly associated with H II regions. Specific BPT demarcation lines are often used as hard boundaries to distinguish between different ISM ionization processes in galaxies even though physically (due to line-of-sight blending and other physical processes) those demarcations cannot be hard boundaries.

The theoretical "maximum starburst" demarcation line proposed by Kewley et al. (2001) divides the region where ionization could still be explained by pure star-formation from the region where AGN ionization is required to contribute to the emission. Similarly, the empirical 'pure star-forming' BPT demarcation line proposed by Kauffmann et al. (2003) defines a part in the BPT assumed to be powered purely by H II regions whereas other mechanisms can play a role in the remaining part. The gap in between the stricter "pure star-forming" and the "maximum starburst" demarcation lines is often referred to as the mixed or composite BPT region.

The AGN contamination to H α across the BPT and, in particular, through the composite region can be tackled in different ways. Nascimento et al. (2019) considers the pure star-forming region and the composite region to be entirely associated with star formation

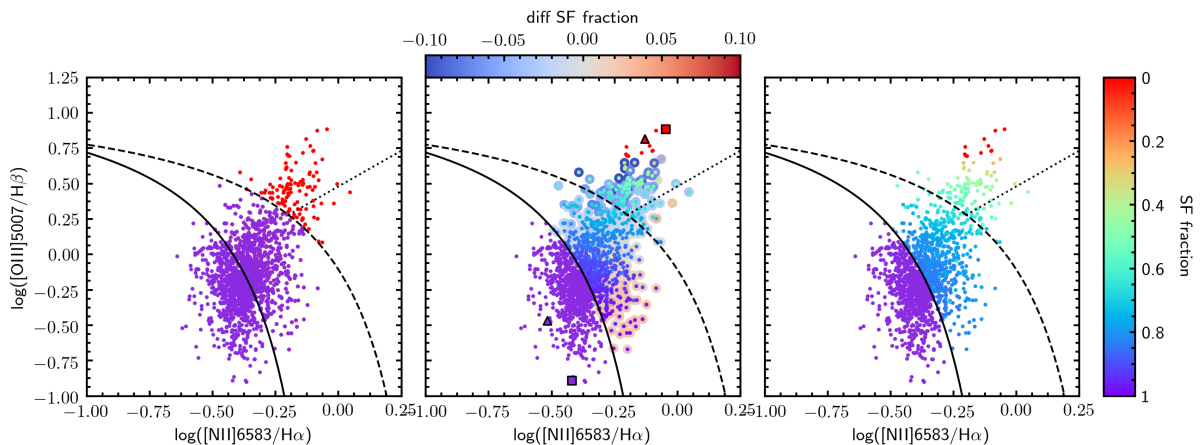


Figure 2.3: BPT diagram of HE 0853+0102 as an example for a mixing sequence between H II regions and AGN photoionization across the host galaxy. We highlight three ways of determining the SF fraction from the BPT diagram. Left panel: A simple demarcation line approach where everything above the Kewley et al. (2001) line is classified as pure AGN and below as pure star formation. Middle panel: Simple linear combination with a χ^2 fit using a fixed line vector as a reference point for the characteristic AGN and H II line ratios. The colored halos around the points represent the difference between the calculated SF fraction adopting two different reference pairs (triangle and square symbols) to highlight the systematic uncertainties introduced by a certain choice. Right panel: MCMC fitting results of the star formation fraction adopting a large cloud of potential reference points for the AGN (red points) and H II region (purple points) which are explored during the MCMC sampling.

assuming that the AGN contribution in the composite region compensates for the ‘hidden’ star formation. Wylezalek et al. (2018) assigns a fixed fraction of 80% of AGN ionization contribution to H α in the BPT region above the “maximum starburst” demarcation line and only a 20% contribution to the composite region. We use the former approach (illustrated in Fig. 2.3, left panel) to be able to consistently compare our results (Table 2.4) with previous works and the more sophisticated methods as described below.

2.3.2.2 BPT mixing sequence

In contrast to the fixed contribution assumed before, there is likely a smooth transition of ionization contributions across galaxies. AGN host galaxies therefore often show a mixing sequence which appears as an elongated structure in the BPT diagram. This mixing sequence (MS) usually exhibits a prominent dependency on the distance from the AGN. As proposed by Davies et al. (2014a,b, 2016, 2017), one can pick basis vectors of emission line ratios to characterize pure AGN and star-forming ionization and treat the composite data points of the MS as a linear combination of the basis vectors:

$$\begin{pmatrix} [\text{O III}]/\text{H}\beta \\ [\text{N II}]/\text{H}\alpha \\ [\text{S II}]/\text{H}\alpha \end{pmatrix}_{\text{MS}} = f_{\text{AGN}} \times \begin{pmatrix} [\text{O III}]/\text{H}\beta \\ [\text{N II}]/\text{H}\alpha \\ [\text{S II}]/\text{H}\alpha \end{pmatrix}_{\text{AGN}} + f_{\text{SF}} \times \begin{pmatrix} [\text{O III}]/\text{H}\beta \\ [\text{N II}]/\text{H}\alpha \\ [\text{S II}]/\text{H}\alpha \end{pmatrix}_{\text{SF}}. \quad (2.3)$$

Here, the parameters f_{AGN} and f_{SF} represent the non-negative linear coefficient for the AGN and star-forming ionization fractions, correspondingly. An important additional basic constraint of $f_{\text{AGN}} + f_{\text{SF}} = 1$ ensures that flux is preserved. In principle more excitation mechanisms could be added to this equation, but this will lead to degeneracies in the basis vector as they are not fully orthogonal.

The emission line columns are normalized to either $\text{H}\alpha$ or $\text{H}\beta$, which minimizes the impact of internal extinction within the host on the results. Here, we include the $[\text{S II}]/\text{H}\alpha$ line ratio from the other classical BPT diagram and more line ratios could in principle be considered if SNR are high enough to be informative.

The idea behind the method is to pick emission-line basis vectors at the extreme ends of the mixing sequence, which should best reflect the assumption of two completely independent excitation mechanisms. The process of picking such emission-line ratio basis vectors allows considerable freedom and uncertainty. For example, the selected pair of basis vectors may not fully capture the different ISM conditions across the galaxies such as metallicity or ionization parameter. In the Fig. 2.3, middle panel, the example of two different bases pairs - triangle and square symbols - leads to a 10% difference in the resulting SF fraction.

For more meaningful results, the uncertainties caused by the choice of the basis vector need to be estimated and included into the final SFR uncertainty. With Monte Carlo Markov Chain (MCMC) algorithms it is possible to use the Bayesian approach and also take into account the uncertainty of the underlying model. So, our solution to the basis-picking problem is to define a large number of basis ratio sets and let the MCMC sampling to choose basis vectors for a certain spaxel and, more importantly, take the uncertainty of this choice into account. We use the MCMC python package EMCEE to develop a python package called RAINBOW¹² designed to handle the mixing sequence fitting. For each given spaxel it tries various combinations of basis vectors and determines the posterior probability distribution of the parameters through maximizing the likelihood function:

$$\ln p(\vec{y}|\vec{x}_{\text{AGN}}, \vec{x}_{\text{SF}}, f_{\text{SF}}, \vec{\sigma}_y, \mathcal{F}) = -\frac{1}{2} \sum \left[\frac{(\vec{y} - \vec{y}_{\text{model}})^2}{\vec{\sigma}^2} + \ln(2\pi\vec{\sigma}^2) \right], \quad (2.4)$$

$$\vec{\sigma}^2 = \vec{\sigma}_y^2 + \vec{y}_{\text{model}}^2 \times \mathcal{F}^2;$$

where \vec{y} represents the vector of emission line ratios of the fitted spaxel, $\vec{\sigma}_y$ is the corresponding error vector, \vec{x}_{AGN} and \vec{x}_{SF} represent basis vectors, and the model is $\vec{y}_{\text{model}}(\vec{x}_{\text{AGN}}, \vec{x}_{\text{SF}}, f_{\text{SF}}) = (1 - f_{\text{SF}})\vec{x}_{\text{AGN}} + f_{\text{SF}}\vec{x}_{\text{SF}}$ such as the vector equation 2.3. The likelihood function here is a Gaussian where the variance is underestimated by the fractional amount parameter \mathcal{F} , that represents an uncertainty of the model. The star-forming ionization fraction f_{SF} and its uncertainty then is inferred from the probability distribution. An example of the MCMC fitting result from RAINBOW is shown in the right panel of Fig. 2.3.

Our criteria of picking SF emission-line ratio basis vectors from the mixing sequence are: first, SF bases should be below the "pure star-forming line" (Kauffmann et al. 2003); second, the signal-to-noise ratio of all the involved lines should be 3σ or more ($> 3\sigma$ threshold is used to reduce the number of the basis vectors which speeds-up the fitting process); third, a certain radius may be specified to bound the basis vectors closer to the center and represent a narrower range of metallicities and ionization parameters. The criteria of picking AGN

¹²Publicly available open-source at <https://gitlab.com/SPIrina/rainbow>

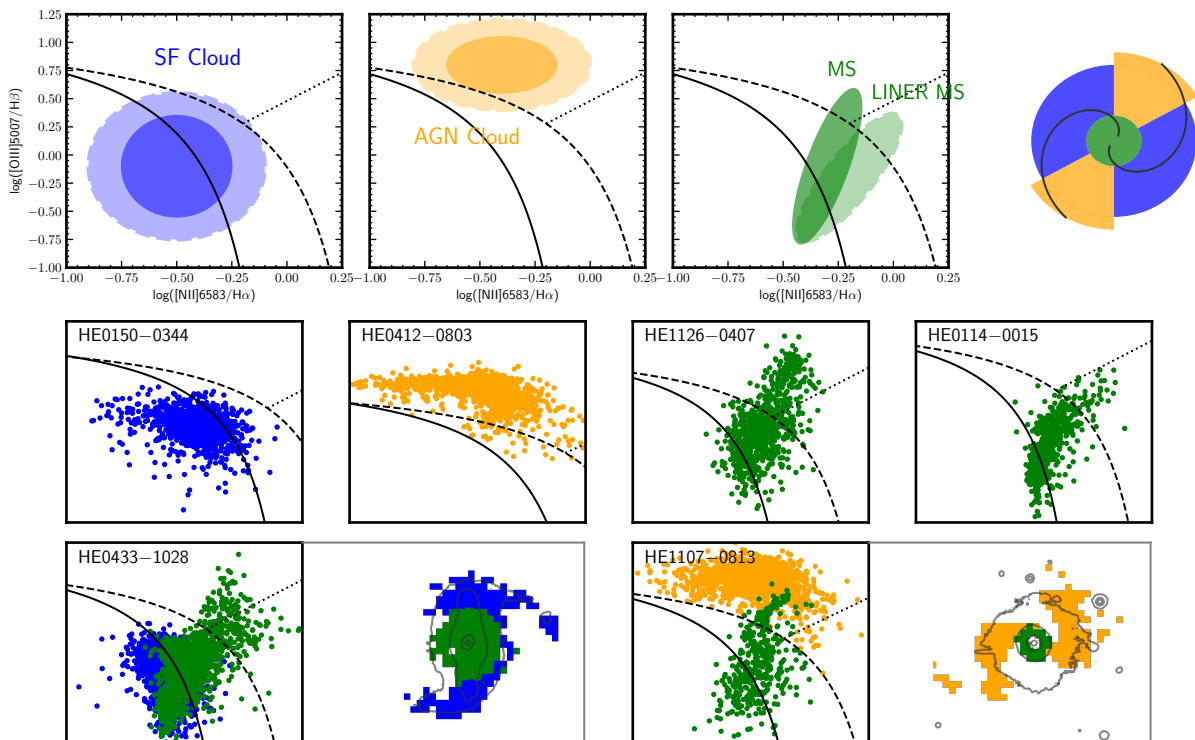


Figure 2.4: Schematic sketch of the BPT morphology populations. Upper row: On the right there is a representation of a galaxy with a central region in green, the rest of the galactic body in blue, and an AGN ionization cone in yellow. These regions populate specific areas on the BPT diagram: left diagram: star-forming cloud with two different sizes; middle diagram: AGN-ionized cloud with two sizes; right diagram: mixing sequence elongated toward the AGN area and a mixing sequence elongated toward the LINER area. Middle row: BPT diagram schematic examples for the SF cloud, AGN cloud, mixing sequence and LINER mixing sequence dominated galaxies. Lower row: BPT diagram and spatial map examples for SF cloud and AGN cloud combined with a mixing sequence in one galaxy.

(or shock/evolved star, as described in section 2.3.2.3) photoionization basis vector from the mixing sequence are the following: first, $[\text{O III}]/\text{H}\beta$ is above a certain threshold, this threshold cannot be same for all galaxies, as it depends on the strength of the AGN, and, therefore, is set to a value between 0.5 — 0.8 (0.25 — 0.5 for LINERs) depending on a galaxy, so that only the top spaxels are selected; second, a certain distance from the AGN may be specified to separate the AGN basis in the central spatial region and extended AGN cloud. The adopted selection is shown on a galaxy-by-galaxy case in Fig. A.4 for the entire sample in the Appendix A.1.

2.3.2.3 BPT morphology

The idea of treating the mixing sequence as a signature of physical mixing of H II regions and AGN ionized regions suggests that different populations of spaxels on a BPT diagram can be differentiated based on their properties. We name this approach BPT morphology, as the idea is to distinguish different shapes on the diagram (see Fig. 2.4):

Table 2.3: Separation radii for galaxies with star-forming cloud and/or AGN-ionised cloud. SF and AGN cloud spaxels are located outside of the corresponding spatial radii.

Object	SF radius [arcsec]	AGN radius [arcsec]
HE 0021–1810	15.0	—
HE 0351+0240	—	7.0
HE 0433–1028	9.0	—
HE 1107–0813	7.0	4.0
HE 1108–2813	13.0	—
HE 1237–0504	7.0	—
HE 1353–1917	15.0	5.0
HE 2211–3903	13.0	—
HE 2233+0124	—	3.0

1) The star-forming cloud is an extended structure located under the "maximum starburst line" of Kewley et al. (2001) on a BPT diagram. This emission arises from across the star forming body of a galaxy and, therefore, contains emission from regions with different metallicities, densities, and ionization parameters. The variance of these ISM parameters results in the extensive shape that covers large area in the BPT diagram. Although it spreads out to the composite area between the "pure star-forming" and the "maximum starburst" demarcation lines on the BPT diagram, we assume that there is no need to clean this group of spaxels from the AGN contamination. See HE 0150–0344 (Fig. 2.4 middle row, left) as an example of a galaxy without AGN but with the spaxels spreading to the composite BPT area.

2) The AGN-ionized cloud is a structure which spans the upper region of a BPT diagram and spreads to the left side toward lower $[\text{N II}]/\text{H}\alpha$ line ratios. This corresponds to the extended narrow-line region or AGN-illuminated gas. Spatially, this region can reach from the AGN across the entire galaxy and even outside of the galaxy's main body. This group of spaxels does not contribute to the galaxy's SFR, although we can infer the upper limits considering hidden star formation as highlighted below.

3) The mixing sequence is already described in the section above; it is an elongated structure on a BPT diagram which tends to be located in the central region of a galaxy. However, not all mixing sequences end in the AGN ionized area of the BPT diagram, where some are extending from the H II regions area to the LINER area likely due to different excitation mechanisms for the LINER emission. Nevertheless, the LINER mixing sequence can be treated in the same way as the AGN mixing sequence, following the same assumption of the two main excitation sources — star formation and LINER excitation. The model (Eq. 2.3) will then have f_{LINER} instead of f_{AGN} with the same flux preservation constrain $f_{\text{LINER}} + f_{\text{SF}} = 1$.

An AGN host galaxy can have one of the described populations or even a combination of those (see the galaxy-by-galaxy cases in Appendix A.1, Fig. A.4). We separate star-forming clouds and AGN-ionized clouds with a simple yet efficient method: manually introducing fixed spatial radii for each individual galaxy (listed on the Table 2.3) and separating the regions with the circles as on the bottom examples of Fig. 2.4 and Fig. A.4. After separating different populations we assume that the SF cloud and AGN-ionized cloud have 100% and 0% contribution to the star-formation rate, correspondingly. The mixing sequence is modeled, out to a certain radius, with RAINBOW as described in the previous section to compute SF

fractions along the sequence.

However, we attempt to correct all populations for the AGN contribution (similarly as with the mixing sequence). Given that some small contribution to the $H\alpha$ emission from star formation may be hidden in galaxies which display only an AGN cloud morphology, we estimate an upper limit for the SF contribution adopting AGN bases or SF bases from the other galaxies with a prominent mixing sequence and apply our RAINBOW analysis.

2.3.3 Gas-phase metallicity

Another important characteristic of the ionized gas is the metallicity. The gas-phase metallicity tracks the immediate enrichment history of the ISM due to the evolution of stars and their metal yields across the galaxy. Undisturbed disk galaxies typically have negative metallicity gradients (Sánchez et al. 2014) and their central metallicity correlates with the stellar mass of a galaxy (Tremonti et al. 2004; Kewley & Ellison 2008). As stellar evolution is a long-term process, outflows and inflows of gas on short timescales can significantly affect the observed metallicity distribution and therefore can be used as a key diagnostic to understand the origin and motions of gas on galactic scales. For example a flattening and dilution of gas-phase metallicity have been observed during galaxy mergers and interactions (e.g., Ellison et al. 2008; Kewley et al. 2010; Thorp et al. 2019), and in barred galaxies (Martin & Roy 1994; Sánchez et al. 2014) where low-metallicity gas from the outskirts is efficiently transported toward the center. On the other hand, gas outflows can enrich the circum-galactic medium with metals from the galaxy center which has been observationally confirmed from absorption line studies (e.g., Bordoloi et al. 2011; Tumlinson et al. 2011; Bouché et al. 2012; Nielsen et al. 2015; Schroetter et al. 2019).

Measuring gas-phase metallicities across AGN host galaxies is more complicated because all strong-line metallicity diagnostics are calibrated for H II regions. Their application to regions photoionized by the AGN is invalid in the majority of cases, but specific calibrations have been developed (e.g., Storch-Bergmann et al. 1998). The metallicity measurements can in principle be restricted to H II regions ionized by star formation (as identified from BPT diagnostics) in AGN host galaxies (e.g., Husemann et al. 2014), but this approach greatly limits suitable targets and radial coverage. The $[N II]/H\alpha$ (N2 index) line ratio is one of the prominent strong-line metallicity calibrators (Pettini & Pagel 2004; Marino et al. 2013) for H II regions. Photoionization models show that the N2 index should also trace the metallicity in AGN photoionized regions (e.g., Groves et al. 2006) with a different scale. That the situation is more complex was shown by Stern & Laor (2013) as they found a secondary dependence of the N2 index with AGN luminosity. At the same time they discovered that the $[N II]/[S II]$ (N2S2 index) is well recovering the mass-metallicity relation of galaxies for AGN hosts independent of AGN luminosity. Indeed, the N2S2 index is generally a good metallicity calibrator (Dopita et al. 2016) also for SF ionized H II regions, but not as widely used given that the diagnostic lines are significantly fainter.

In Husemann et al. (2019), we established a N2S2 index calibration based on the SDSS galaxy sample, and used it to map the gas-phase metallicity across the CARS AGN galaxy HE 1353-1917. The metallicity pattern revealed that the ENLR of the edge-on galaxy follows a very similar radial metallicity than the star forming disk. This let us conclude that the diffuse extra-planar gas was expelled by SN-driven winds rather than an outflow from the

Table 2.4: H α -based SFRs and metallicity estimated from the IFU emission lines

Object	demarcation line approach		class ^c	BPT rainbow method		12 + log(O/H) ^d [r_{eff}^{-1}]	$\alpha_{\text{O}/\text{H}}^{\text{e}}$ [r_{eff}^{-1}]
	$f_{\text{H}\alpha}^{\text{a}}$ [$10^{-16} \text{ erg s}^{-1} \text{ cm}^{-2}$]	$\text{SFR}_{\text{H}\alpha}^{\text{b}}$ [$M_{\odot} \text{ yr}^{-1}$]		$f_{\text{H}\alpha}^{\text{a}}$ [$10^{-16} \text{ erg s}^{-1} \text{ cm}^{-2}$]	$\text{SFR}_{\text{H}\alpha}^{\text{b}}$ [$M_{\odot} \text{ yr}^{-1}$]		
HE0021-1819	359 ± 36	1.3 ± 0.1	MS	342 ± 34	1.2 ± 0.1	8.89 ± 0.02	-0.031 ± 0.010
HE0040-1105	16 ± 2	0.03 ± 0.00	AGN	<41	<0.1	8.85 ± 0.02	0.040 ± 0.016
HE0045-2145	5672 ± 567	3.1 ± 0.3	LMS	4687 ± 477	2.5 ± 0.3	9.16 ± 0.02	-0.018 ± 0.003
HE0108-4743	8594 ± 859	5.9 ± 0.6	MS	8251 ± 825	5.7 ± 0.6	9.05 ± 0.01	-0.055 ± 0.009
HE0114-0015	978 ± 98	2.5 ± 0.3	LMS	901 ± 90	2.3 ± 0.2	9.06 ± 0.02	-0.007 ± 0.011
HE0119-0118	1107 ± 111	4.1 ± 0.4	MS	1006 ± 101	3.8 ± 0.4	8.99 ± 0.01	0.026 ± 0.020
HE0150-0344	3961 ± 396	10.5 ± 1.0	8.88 ± 0.02	-0.029 ± 0.005
HE0203-0031	71 ± 7	0.16 ± 0.02	AGN+SF	<202	<0.5	9.08 ± 0.02	-0.006 ± 0.003
HE0212-0059	4163 ± 416	3.5 ± 0.4	MS	3978 ± 398	3.4 ± 0.3	8.99 ± 0.00	-0.050 ± 0.013
HE0224-2834	368 ± 37	1.7 ± 0.2	MS+AGN	397 ± 40	1.8 ± 0.2	8.88 ± 0.01	-0.006 ± 0.007
HE0227-0913	2970 ± 297	1.0 ± 0.1	MS	2933 ± 293	0.9 ± 0.1	8.96 ± 0.01	-0.017 ± 0.007
HE0232-0900	8226 ± 823	19.0 ± 1.9	MS	8197 ± 820	19.0 ± 1.9	9.00 ± 0.01	-0.017 ± 0.004
HE0253-1641	197 ± 20	0.24 ± 0.02	MS	232 ± 23	0.28 ± 0.03	8.97 ± 0.02	-0.025 ± 0.023
HE0345+0056	3474 ± 348	4.1 ± 0.4	SF	3477 ± 348	4.1 ± 0.4	8.81 ± 0.09	0.066 ± 0.073
HE0351+0240	143 ± 14	0.23 ± 0.02	AGN	<240	<0.4	8.80 ± 0.03	-0.010 ± 0.013
HE0412-0803	93 ± 9	0.17 ± 0.02	AGN	<192	<0.3	8.85 ± 0.02	0.009 ± 0.007
HE0429-0247	262 ± 26	0.6 ± 0.1	AGN	<338	<0.7	8.80 ± 0.02	0.016 ± 0.015
HE0433-1028	5997 ± 600	9.3 ± 0.9	MS+SF	6700 ± 671	10.4 ± 1.0	8.97 ± 0.01	-0.049 ± 0.009
HE0853+0102	407 ± 41	1.4 ± 0.1	MS	381 ± 38	1.3 ± 0.1	8.89 ± 0.02	-0.005 ± 0.021
HE0853-0126	142 ± 14	0.6 ± 0.1	SF	130 ± 13	0.6 ± 0.1	8.60 ± 0.16	0.130 ± 0.154
HE0934+0119	650 ± 65	2.1 ± 0.2	MS+SF	599 ± 60	1.9 ± 0.2	8.92 ± 0.02	-0.098 ± 0.011
HE0949-0122	26 ± 3	0.01 ± 0.00	AGN	<214	<nan	8.90 ± 0.04	0.049 ± 0.039
HE1011-0403	328 ± 33	1.4 ± 0.1	LMS	294 ± 29	1.3 ± 0.1	9.03 ± 0.01	-0.022 ± 0.014
HE1017-0305	353 ± 35	1.1 ± 0.1	LMS	340 ± 34	1.1 ± 0.1	9.00 ± 0.02	-0.007 ± 0.021
HE1029-1831	4689 ± 469	9.4 ± 0.9	SF	3732 ± 377	7.5 ± 0.8	9.12 ± 0.01	-0.099 ± 0.006
HE1107-0813	121 ± 12	0.5 ± 0.1	MS+AGN	115 ± 12	0.49 ± 0.05	9.08 ± 0.02	-0.003 ± 0.006
HE1108-2813	6094 ± 609	4.2 ± 0.4	MS+SF	5840 ± 587	4.1 ± 0.4	9.01 ± 0.01	-0.110 ± 0.008
HE1126-0407	195 ± 20	1.0 ± 0.1	MS	217 ± 22	1.1 ± 0.1	9.08 ± 0.03	-0.048 ± 0.022
HE1237-0504	1501 ± 150	0.14 ± 0.01	LMS	3249 ± 425	0.31 ± 0.04	9.10 ± 0.00	-0.144 ± 0.025
HE1248-1356	2766 ± 277	0.7 ± 0.1	MS	3034 ± 303	0.8 ± 0.1	9.05 ± 0.01	-0.128 ± 0.012
HE1310-1051	1294 ± 129	1.9 ± 0.2	SF	1258 ± 127	1.8 ± 0.2	8.84 ± 0.07	0.010 ± 0.049
HE1330-1013	763 ± 76	0.45 ± 0.05	MS	716 ± 72	0.42 ± 0.04	9.13 ± 0.04	-0.146 ± 0.053
HE1338-1423	742 ± 74	1.6 ± 0.2	AGN	1319 ± 135	2.9 ± 0.3	9.04 ± 0.06	-0.019 ± 0.075
HE1353-1917	609 ± 61	0.9 ± 0.1	MS+A+S	594 ± 59	0.9 ± 0.1	8.96 ± 0.02	-0.119 ± 0.013
HE1417-0909	6 ± 1	0.01 ± 0.00	AGN	<23	<0.1	8.73 ± 0.08	0.106 ± 0.066
HE2128-0221	154 ± 15	0.5 ± 0.1	MS	140 ± 14	0.49 ± 0.05	8.93 ± 0.04	-0.047 ± 0.020
HE2211-3903	2419 ± 242	4.7 ± 0.5	MS+SF	2534 ± 253	4.9 ± 0.5	9.08 ± 0.01	-0.145 ± 0.010
HE2222-0026	43 ± 4	0.19 ± 0.02	SF	34 ± 3	0.15 ± 0.02	8.80 ± 0.05	0.088 ± 0.050
HE2233+0124	355 ± 36	1.4 ± 0.1	MS+AGN	339 ± 34	1.4 ± 0.1	9.05 ± 0.02	-0.057 ± 0.018
HE2302-0857	1339 ± 134	3.7 ± 0.4	MS	1618 ± 162	4.4 ± 0.4	8.92 ± 0.01	-0.074 ± 0.013

^a Integrated extinction-corrected H α flux decontaminated by AGN contribution either using a demarcation line cut or the rainbow method presented here. Given the high S/N of the data the error is dominated by the systematics in the absolute photometric zero-point which is assumed to be 10%.

^b H α -based SFR determined from the associated H α luminosity following the calibration of Calzetti et al. (2007), see Eq. 2.2.

^c Classification of the BPT in a (LINER) mixing sequence (L)MS, AGN cloud, SF cloud and any combination of the four.

^d Central oxygen abundance on the Tremonti et al. (2004) metallicity scale determined through the N2S2 index following Eq. 2.5. A linear fit to the radial distribution is used to determine the central abundance as the spatial coverages varies through the sample.

^e Slope of the linear metallicity gradient normalized to the effective radius of the respective galaxy as reported in Husemann et al. (2022).

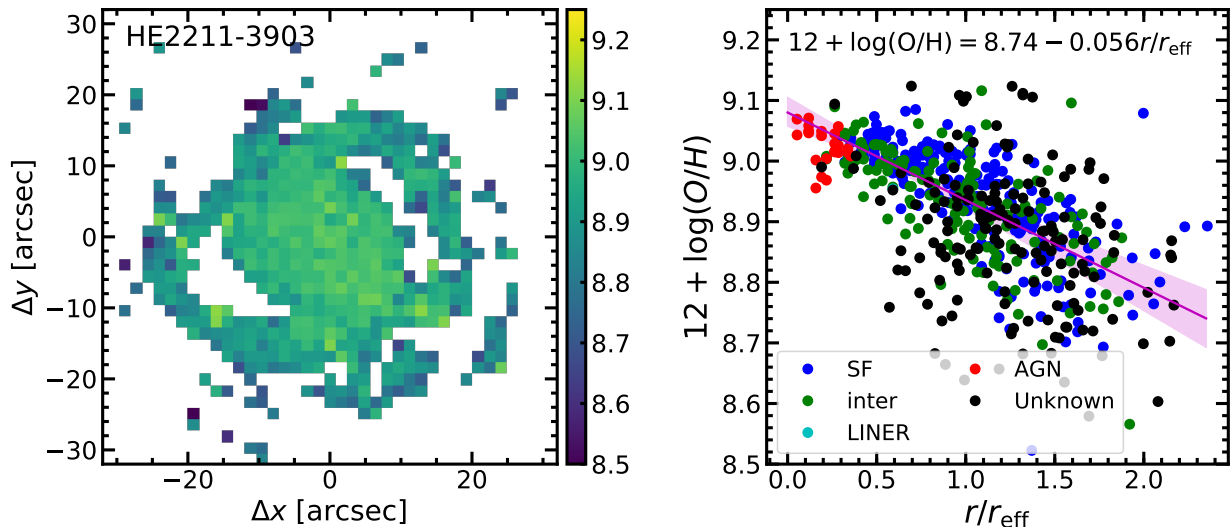


Figure 2.5: Example of the 2D and radial metallicity distribution for HE2211–3903. The oxygen abundance was measured using the N2S2 index which is almost insensitive to the excitation. On the left panel the full 2D distribution is shown and on the right panel a radial projection in units of the effective radius taken from the single Sersic model. A linear fit is performed and shown as the red line.

central AGN. Here, we apply the N2S2 index calibration established in Husemann et al. (2019) for all CARS targets to infer the metallicity gradient and absolute scale of the central metallicity. In order to directly use the metallicity determined for SDSS based on Tremonti et al. (2004) we determined an $N2S2 = \log([\text{N II}]\lambda 6583/[\text{S II}]\lambda\lambda 6716, 6731)$ calibration for this SDSS metallicity scale in the similar way as described in Husemann et al. (2019):

$$12 + \log(\text{O}/\text{H}) = 8.875 + 0.827 \times N2S2 - 0.288 \times N2S2^2 \quad (2.5)$$

Based on this calibration we estimated the oxygen abundance across the galaxies and reconstruct the radial metallicity gradient, as shown for the face-on disk galaxy HE2211–3903 in Fig. 2.5. For this galaxy a negative radial metallicity gradient is clearly recovered with a slope of $\alpha_{\text{O}/\text{H}} = -0.055 \text{ dex } r_{\text{eff}}^{-1}$ with a zero-point central metallicity of $12 + \log(\text{O}/\text{H}) = 8.732$. As expected from the work of Stern & Laor (2013), the N2S2 index indeed recovers a matching absolute metallicities even in the case of strong AGN ionization without significant offset in metallicity as shown in Fig. 2.5. Hence, the 2D map of the estimated oxygen abundance does not show any features related to the varying ionization conditions throughout its disk. While the $[\text{N II}]$ and $[\text{S II}]$ emission lines may not exactly originate from the same location within H II region, due to the ionization structure of the nebulae on 100 pc scales (e.g., Sanders et al. 2020; Mannucci et al. 2021), our calibration based on SDSS spectra ($3''$ apertures) consistently include also part of the surrounding diffuse gas similar to our MUSE observation with typical resolutions of $0''.7\text{--}1''.0$ covering 300–1000 pc depending on redshift. Because we are unable to isolate individual H II regions with CARS, any calibration based on isolated H II would be invalid.

This methodology therefore allows us an initial characterization of the metallicity for the entire sample, as listed in Table 2.4 and maps shown in Fig. A.5. Notably, we exclude a close

star-forming companion in case of HE 0203–0031 and HE 1017–0305 from the radial fitting and fixed the center to the AGN position in all cases. As the absolute metallicity scale is strongly dependent on the underlying calibration we also transform our oxygen abundance estimate from the original O3N2 calibration scale as used in (Husemann et al. 2019) to the one of Tremonti et al. (2004) so that we can more easily apply calibrations from the non-AGN SDSS sample as discussed below. Uncertainties are determined by bootstrapping; re-fitting the linear relation after randomly sub-selecting 80% of the data points.

2.4 Results and discussions

2.4.1 Finding SFR dependencies on AGN parameters

In order to investigate the potential impact of AGN on the total SFR of their host galaxies we collect the derived CARS host galaxies parameters such as AGN-corrected integrated $H\alpha$ and IR luminosity and associated SFRs together with the stellar mass from our analysis presented above. From the SFRs we compute the specific SFR (sSFR) by dividing with the stellar mass, that is $\text{sSFR} = \text{SFR}/M_\star$ and compare it against the stellar mass as shown in the Fig. 2.6 for the $H\alpha$ and IR-based SFRs, respectively.

We compare the CARS host galaxies with the non-AGN galaxy population at low redshifts using the data from SDSS (Brinchmann et al. 2004; Abazajian et al. 2009), xCOLD GASS (Saintonge et al. 2017), KINGFISH (Skibba et al. 2011), and the Herschel Reference Survey (HRS, Smith et al. 2012; Boselli et al. 2015). Those reference samples highlight the position of the so-called star-forming main-sequence (SFMS) as determined by various authors and is indicated on Fig. 2.6, with blue dashed lines. These were derived from SDSS galaxies in the $H\alpha$ diagram by Renzini & Peng (2015) and Shimizu et al. (2015) for the IR diagram.

Those SFMS relations are derived from different data sets, and as our goal is to achieve consistency between the two diagrams, we consistently determine the SFMS from the xCOLD GASS (xCG) sample. The xCG is a subsample from the SDSS sample, therefore $H\alpha$, IR, stellar mass, and also CO(1–0) and metallicity data are available from the literature sources listed above. As there is also a BPT classification of the objects, we exclude AGN and LINER galaxies to define a clean star-forming subsample of galaxies (hereafter training sample) resulting in 197 objects for the $H\alpha$ diagram and 86 objects for the IR diagram. The linear SFMS fits to the training sample data and the corresponding R^2 scores (defined below in equation 2.7) are:

$$\begin{aligned} \log L_{H\alpha} &= (0.69 \pm 0.03) \log M_\star + (34.3 \pm 0.3); R^2 = 0.50 \\ \log L_{\text{IR}} &= (0.81 \pm 0.03) \log M_\star + (35.7 \pm 0.3); R^2 = 0.62 \end{aligned} \tag{2.6}$$

Our SFMS linear relations are consistent with the literature determinations shown in Fig. 2.6 within the reported scatter.

In order to assess the differences between the CARS hosts and the training sample we compute the residuals along the SFMS relation (Fig. 2.6 bottom panel). The CARS objects exhibit a scatter around the SFMS of 0.69 dex based on $H\alpha$ and 0.60 dex based on IR SFR, respectively, ignoring the upper limits. Moreover, the residuals reveal a clear negative correlation with a Pearson correlation coefficient of $r = -0.69$ and $r = -0.61$ for the $H\alpha$

and IR SFR, respectively. This negative trend might be naïvely interpreted as a result of star-formation quenching where higher mass galaxies appear to be more passive potentially due to the effects of the AGN (e.g., Cicone et al. 2014; Saintonge et al. 2017; Lacerda et al. 2020) considering our AGN selection.

However, the stellar mass is not the only parameter which controls the SFR of a galaxy. The cold gas content was shown to be another fundamental parameter linked to the SFR and explaining part of the scatter in SFR perpendicular to the SFMS (Tacconi et al. 2018; Colombo et al. 2020; Piotrowska et al. 2020; Ellison et al. 2020). Furthermore, the gas-phase metallicity is being discussed to be linked to the SFR and stellar mass, the so-called fundamental mass-metallicity relation (Lequeux et al. 1979; Mannucci et al. 2010; Yates et al. 2012; Curti et al. 2020), but see also Sánchez et al. (2017, 2019). In particular, the metallicity could be related to the metallicity-dependent conversion of L_{CO} to the total cold gas mass (e.g., Genzel et al. 2012; Bolatto et al. 2013; Carleton et al. 2017; Utomo et al. 2017) or the general ability of the gas to cool to form star-forming gas clouds.

In order to quantitatively compare the previous model with the ones introduced further we use the coefficient of determination or the R^2 score (Draper 1998). It provides an indication of how well the fit is for the given dataset with the best possible score of 1.0. Unsuitable models can result in negative R^2 scores and an R^2 score of 0.0 would result from a constant model that always predicts the expected value. For a dataset $y_1 \dots y_n$ with fitted values $y_{1 \text{ model}} \dots y_{n \text{ model}}$ and a mean value $\bar{y} = \frac{1}{n} \sum_{i=1}^n y_i$ the R^2 score is calculated as follows:

$$R^2 = 1 - \frac{\sum_i (y_i - y_{i \text{ model}})^2}{\sum_i (y_i - \bar{y})^2}. \quad (2.7)$$

As our model above does not take into account the cold gas content nor the gas-phase metallicity of the host galaxy, we expand our one-dimensional linear model into a multidimensional linear model for the SFR (hereafter SFMS+gas model) with stellar mass (M_\star), CO(1-0) luminosity (L_{CO}) and metallicity ($12 + \log(\text{O}/\text{H})$) as the independent parameters. Here, we use the CO(1-0) luminosity from Saintonge et al. (2017) as the main cold gas mass proxy and the oxygen abundance $12 + \log(\text{O}/\text{H})$ determined from the ionized gas emission lines in the SDSS spectra as determined by Tremonti et al. (2004) as the main gas-phase metallicity parameter. This leads to the following formulas for the linear multidimensional model:

$$\begin{aligned} \log(L_{\text{H}\alpha}/[\text{erg s}^{-1}]) = & (-0.01 \pm 0.06) \log(M_\star/[M_\odot]) \\ & + (0.62 \pm 0.04) \log(L_{\text{CO}}/[\text{K km s}^{-1} \text{pc}^2]) \\ & + (-0.01 \pm 0.07)(12 + \log(\text{O}/\text{H})) \\ & + (36.2 \pm 0.5) \end{aligned} \quad (2.8)$$

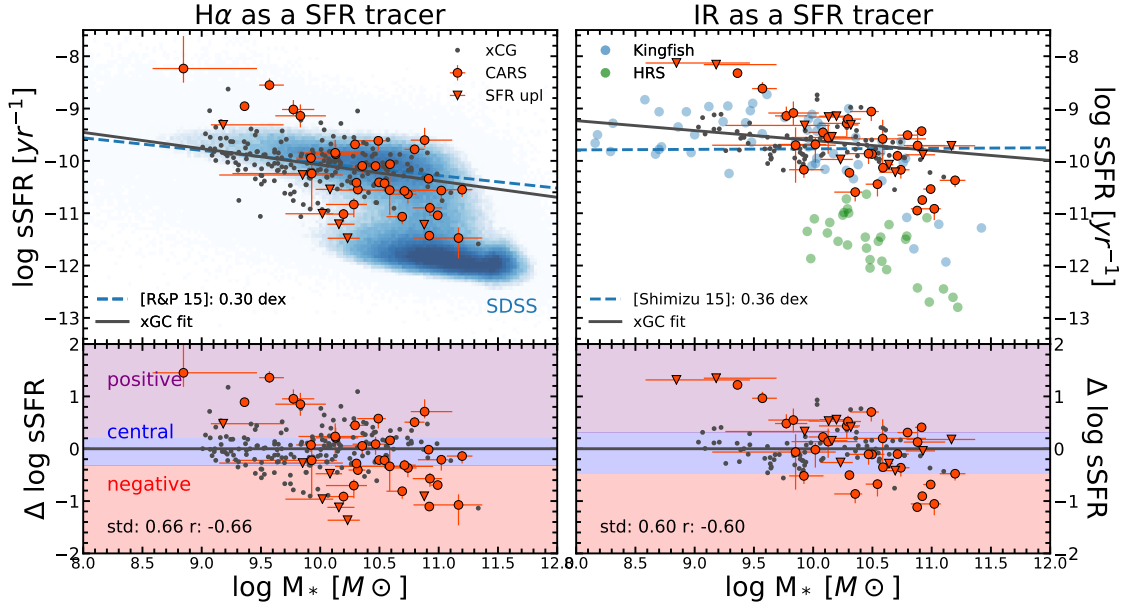


Figure 2.6: Comparison of the sSFR against stellar mass for H α - and IR-based SFR tracers. The CARS objects are shown as red points with error bars, while xCOLD GASS (xCG) are in small gray dots, KINGFISH are in blue and Herschel Reference Survey (HRS) in green. Specific SFR is calculated from H α luminosity (*left panel*) derived after BPT morphology analysis and RAINBOW fitting using the SFR formula $\text{SFR}_{\text{H}\alpha} = 5.3 \cdot 10^{-42} \times L_{\text{H}\alpha}$ (Calzetti et al. 2007). IR specific SFR (*right panel*) derived from the AGNFITTER modeling using the Murphy et al. (2011) SFR formula. The stellar mass is taken from the AGNFITTER modeling parameters. The background on the left plot is the density map of SDSS galaxies (Brinchmann et al. 2004). Linear models to the star-forming main sequence are shown as black solid lines from Renzini & Peng (2015) and Shimizu et al. (2015), respectively. The best-fit linear relation from the xCG sample is shown as the blue dashed line in both cases. In the *lower panel* we show the residuals around the adopted star-forming main sequence where the colored bands (red, blue, and purple) emphasize three bins used further in Fig. 2.8

$$\begin{aligned}
 \log(L_{\text{IR}}/[\text{erg s}^{-1}]) = & (-0.13 \pm 0.06) \log(M_{\star}/[M_{\odot}]) \\
 & + (0.98 \pm 0.04) \log(L_{\text{CO}}/[\text{K km s}^{-1} \text{pc}^2]) \\
 & + (-1.13 \pm 0.09)(12 + \log(\text{O}/\text{H})) \\
 & + (47.0 \pm 0.7)
 \end{aligned} \tag{2.9}$$

with R^2 scores of $R^2 = 0.64$ and $R^2 = 0.89$, respectively.

As gas content is by far the most dominant driver compared to metallicity and metallicity may not be always measurable, we also determine relations that only rely on stellar mass

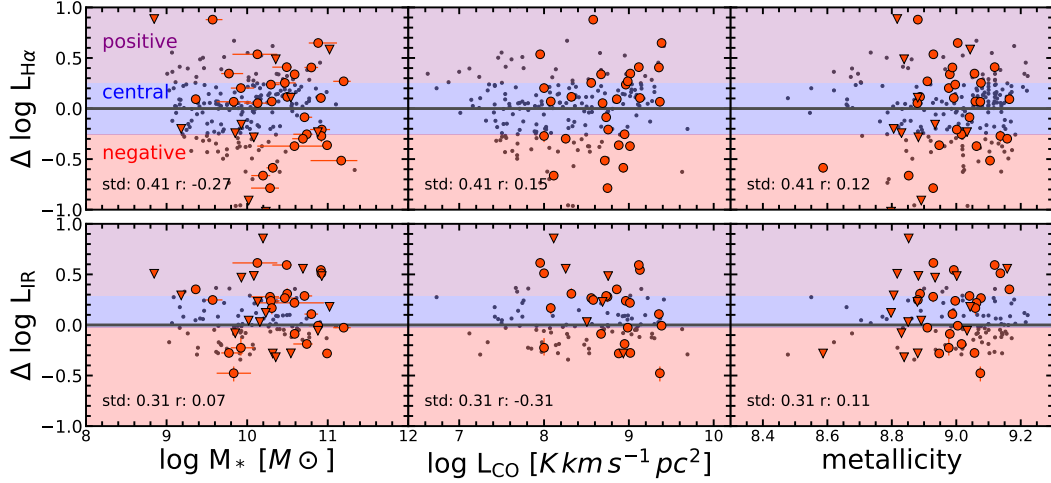


Figure 2.7: Difference between measured and expected H α (upper panels) and FIR luminosity (lower panels) as a function of stellar mass, CO(1-0) luminosity and $12+\log(\text{O}/\text{H})$ ionized gas metallicity. Here we used our more complex model (Eq. 2.1 and Eq. 2.2) to predict the SFR-sensitive luminosities. The black dots are the data from our xCG training sample and the red symbols are the CARS data with triangles indicating upper limits. The colored bands (red, blue and purple) define three bins in residual luminosity as discussed in the text and used for Fig. 2.8.

and gas content:

$$\begin{aligned} \log L_{\text{H}\alpha} = & (-0.01 \pm 0.06) \log(M_{\star}/[M_{\odot}]) \\ & + (0.62 \pm 0.04) \log(L_{\text{CO}}/[\text{K km s}^{-1} \text{pc}^2]) \\ & + (36.2 \pm 0.3) \end{aligned} \quad (2.10)$$

$$\begin{aligned} \log L_{\text{IR}} = & (-0.19 \pm 0.05) \log(M_{\star}/[M_{\odot}]) \\ & + (0.82 \pm 0.04) \log(L_{\text{CO}}/[\text{K km s}^{-1} \text{pc}^2]) \\ & + (38.7 \pm 0.3) \end{aligned} \quad (2.11)$$

The quality of these models can be represented by R^2 scores of $R^2 = 0.64$ and $R^2 = 0.84$, respectively. As expected the quality of the model does not become significantly worse and can be securely used for all samples where metallicity is not available. Here, we use the full model including metallicity because this parameter is available to us and so we can use it in our analysis. In any case the choice of the models does not alter our final results given the similarity of both models and low impact of metallicity.

After building the new model to predict SFR using the xCG training sample, we apply it to the CARS objects with the additional information of $L_{\text{CO}(1-0)}$ taken from Bertram et al. (2007) and $12 + \log(\text{O}/\text{H})$ inferred from the CARS IFU observations as described above. With the new SFMS+gas model we obtain new predictions for the expected SFR of individual CARS objects and present the corresponding residuals in Fig. 2.7. In comparison with the previous residuals (Fig. 2.6 bottom panel), the residuals are significantly smaller.

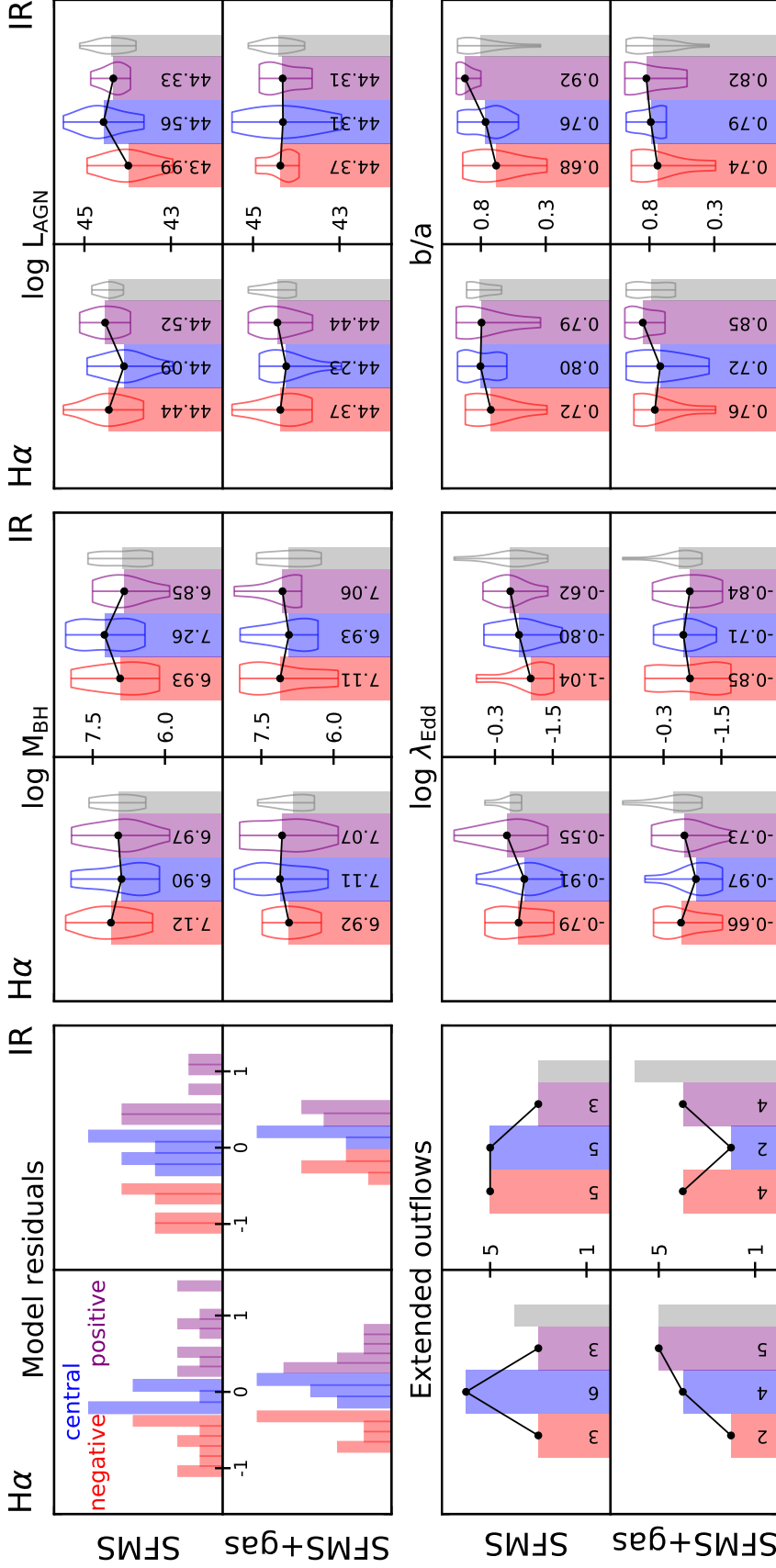


Figure 2.8: Comparison of SFR residuals from the SFMS and SFMS+gas model against various AGN parameters. The *upper left panel* shows the histograms of the residuals for SFMS and SFMS+gas for both H α and IR models, with the red, blue, and purple colors corresponding to the previous plots (Fig. 2.6 and Fig. 2.7, background colors). The other panels show the comparison of the AGN parameters taken from Husemann et al. (2022) and Singha et al. (2022): logarithm of BH mass (upper center), logarithm of AGN bolometric luminosity (upper right), number of the objects, containing extended outflows (*lower left*), logarithm of Eddington ratio (*lower center*), and b/a morphological parameter (*lower right*). *Each of the four models* is represented with three bins (from left to right: negative red, central blue, positive purple) and the forth bin with the upper limits (gray). The error bars of the bins also represent the distribution of the parameters within the bins. The black dots and lines highlight the trend of the mean values that are written over the bins.

The scatter is reduced by a factor of two as the trend with the gas content is taken into account. The initially observed correlation with stellar mass is significantly flattened, with a correlation coefficient consistent with no remaining mass dependence. One potential issue may arise for AGN hosts as the abundance of cold gas has been suspected to be linked with the AGN either by expelling or heating the cold gas (e.g., Carniani et al. 2017; Kakkad et al. 2017; Perna et al. 2018; Bischetti et al. 2021; Circosta et al. 2021). Considering that the residual sSFR scatter is significantly reduced when incorporating cold gas mass in the SFR prediction indicates that this potential effect is negligible for our sample.

In order to understand if there are any remaining link between the residuals in sSFR and various AGN parameters we divide the residual space into three bins (negative, central, and positive residual bins) and compare the mean values of the AGN parameters for each bin. The bins are created such, that the number of objects in the bins is approximately equal (with a small excess of objects in the central bin). Objects with upper limits are treated separately as we cannot necessarily associate them to a specific bin. The central residual bin for IR luminosity is shifted slightly toward higher values because of the larger number of upper limits that are too high to be informative. Those objects with upper limits are missing to populate the central and negative residuals bins, but are mostly included in the case of $H\alpha$. As we are only interested in the relative changes along the residuals we focussed to have sufficient objects in each bin for statistical reasons. In Fig. 2.8, we compare bins in residual SFR for the SFMS and the new SFMS+gas models for both $H\alpha$ and IR SFR tracers allowing us to explore trends with BH mass, AGN luminosity, Eddington ratio and b/a host galaxy axis ratio as reported by Husemann et al. (2022) and Singha et al. (2022) for both proxies.

We find no trends of the residuals to systematically change with the $\log M_{\text{BH}}$ and $\log L_{\text{AGN}}$ given the uncertainties. While a putative correlation is seen with the fraction of objects containing extended outflows in the SFMS+gas model using the $H\alpha$ proxy, it is not reflected in the IR tracer and therefore not robust. While the logarithm of the Eddington ratio ($\log \lambda_{\text{Edd}}$) has a slight increasing trend (e.g. higher AGN Eddington ratio in SFR excess systems) for the SFMS model, such a trend vanishes for the SFMS+gas model. It is important to note that most of the previous studies that investigated the impact of AGN on the SFR only used stellar mass as a proxy for the expected SFR (e.g., Page et al. 2012; Husemann et al. 2014; Shimizu et al. 2015; Balmaverde et al. 2016; Bernhard et al. 2016; Catalán-Torrecilla et al. 2017; Circosta et al. 2018; Scholtz et al. 2020). The inclusion of the cold gas mass to predict the expected SFR in addition to the stellar mass can significantly alter the derived conclusions about potential positive, negative or no AGN feedback on their host galaxies. It is therefore crucial for future studies to take more parameters into account than just stellar mass to properly characterize the parent population of non-AGN galaxies.

In Fig. 2.8 the geometrical parameter b/a (tracing the galaxy inclination) shows a clear trend for both $H\alpha$ and IR SFRs for the SFR model. When comparing the b/a distribution for the negative and positive residual bins with Kolmogorov-Smirnov and Anderson-Darling tests we find a highly significant difference between them for the IR SFR with a p -value of 0.003, but less significant for $H\alpha$. This suggests that dust extinction or hidden star formation is not the driver for this trend. The trend significantly flattens for the SFMS+gas model considering that the overall scatter in the residuals is greatly reduced, so that the difference become insignificant for our sample size. A potential explanation for the tentative trend

might be the orientation of the AGN. The CARS objects are unobscured AGN hosts, which means that the ionization cone of the AGN is pointed to the observer. Hence, the cross-section of the AGN ionization cone which can interact with the ISM is increased when the host galaxies are closer to an edge-on geometry. Such misalignments of the galaxies rotation axis and the central AGN engine can have an important influence on the impact of the AGN on the host galaxy, as has already been proposed for various individual galaxies (e.g., García-Burillo et al. 2014; Gallimore et al. 2016; Cresci et al. 2015b; Alonso-Herrero et al. 2018; Husemann et al. 2019; Smirnova-Pinchukova et al. 2019). With the CARS sample we start to see a potential systematic trend across the population where the potential of the AGN to suppress SFR might also dependent on the relative orientation of the central engine with respect to the galaxy. However, our CARS sample is strongly limited by the low number of more edge-on systems and a bigger sample is needed to gain more insight into this process. Our results highlight that the AGN luminosity may not be the only factor determining the ability of the AGN to impact star formation. The efficiency with which the released energy can couple to the host galaxy adds complexity to the picture, where geometry is certainly just one of many additional parameters to be considered.

2.4.2 Comparison of SFR tracers for AGN host galaxies

Another complexity in investigating the impact of AGN on star formation is caused by the fact that different SFR indicators trace different timescales of star formation. $H\alpha$ emission is related to the most recent star formation (~ 5 Myr) as excited necessarily by hot O stars, whereas IR traces the dust heated by a wider range of stars, and, therefore traces SF over longer timescales (~ 100 Myr; e.g. Kennicutt 1998, Hayward et al. 2014, Flores Velázquez et al. 2021). Both SFR tracers are expected to be implicitly linked to the CO luminosity as a molecular gas mass tracer (conversion factor $\alpha_{\text{CO}} = 4.3 M_{\odot} (\text{K km s}^{-1} \text{pc}^{-2})^{-1}$, Bolatto et al. 2013), because the cold gas is the necessary seed reservoir of which new stars can be formed.

By combining the SFR calibrations for the IR and $H\alpha$ luminosity (Eq. 2.1 and Eq. 2.2) we can make a prediction for their expected relation. Furthermore, we can link the SFR to the CO luminosity given the calibration of Lin et al. (2019):

$$\left(\frac{\text{SFR}_{\text{CO}}}{[M_{\odot} \text{yr}^{-1}]} \right) = 4.67 \times 10^{-10} \left(\alpha_{\text{CO}} \frac{L_{\text{CO}}}{[\text{K km s}^{-1} \text{pc}^{-2}]} \right)^{1.05} \quad (2.12)$$

This leads to the following relation between the $H\alpha$ luminosity and the IR and CO luminosity, respectively.

$$\log \left(\frac{L_{\text{IR}}}{[\text{erg s}^{-1}]} \right) = \log \left(\frac{L_{\text{H}\alpha}}{[\text{erg s}^{-1}]} \right) + 2.14 \quad (2.13)$$

$$\log \left(\frac{L_{\text{CO}}}{[\text{K km s}^{-1} \text{pc}^2]} \right) = 0.95 \log \left(\frac{L_{\text{H}\alpha}}{[\text{erg s}^{-1}]} \right) - 31.05 \quad (2.14)$$

Comparing the three luminosities with each other in Fig. 2.9 we find that the CARS sample and the training sample from the xCG are significantly offset with respect to the predicted relation between $H\alpha$ and IR luminosity. Despite this, the relation between L_{CO} and $L_{\text{H}\alpha}$ as

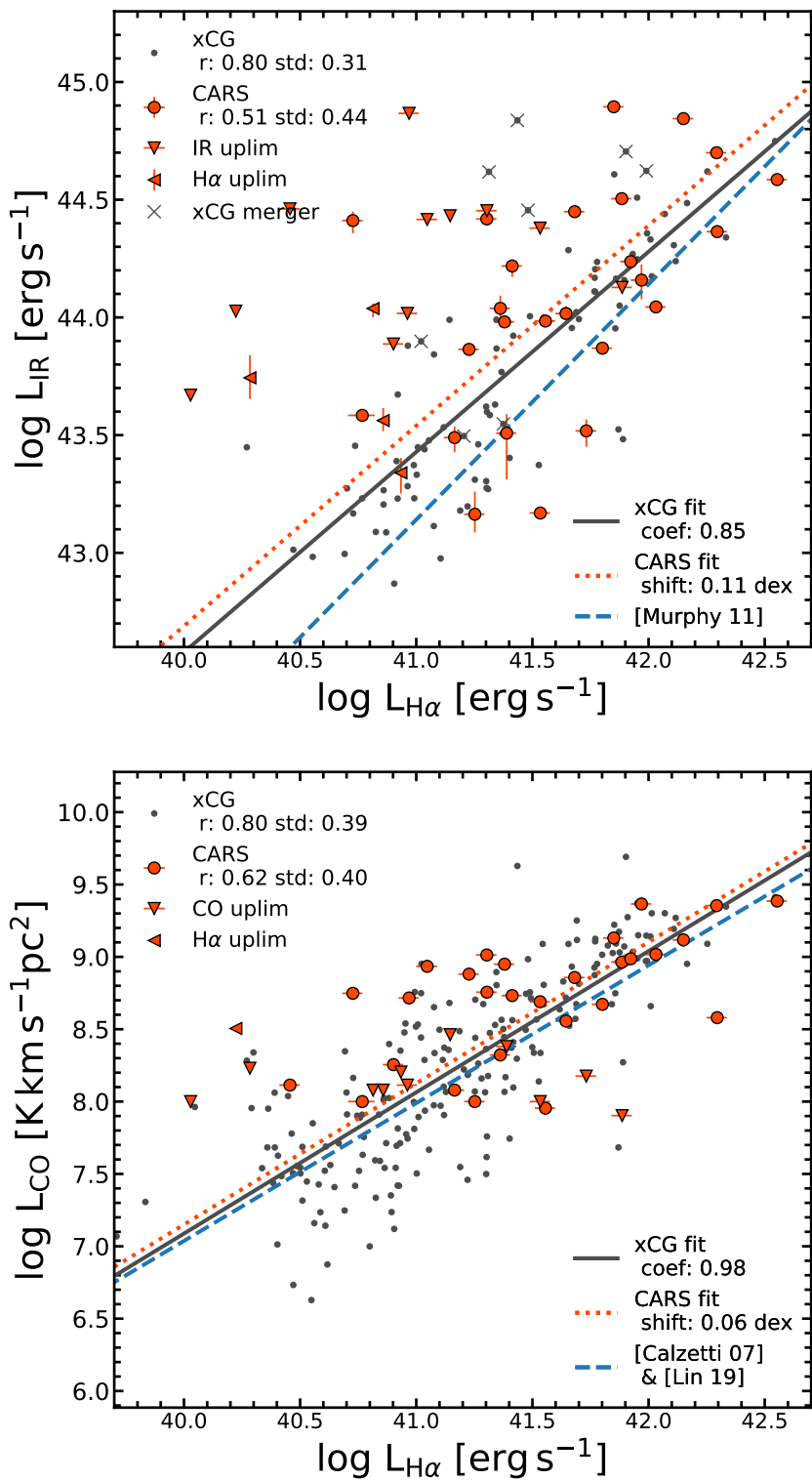


Figure 2.9: 8–1000 μ m IR luminosity L_{IR} (*left panel*) and the CO (1–0) luminosity L_{CO} (*right panel*) plotted against $H\alpha$ luminosity. The training sample from the xCG (gray dots) is compared to the CARS objects (red circles and triangles for the 5σ upper limits). Galaxy mergers in the xCG sample as classified by GalaxyZoo2 are additionally marked (black crosses) on the left panel. The blue dashed line corresponds to Eq. 2.13 and Eq. 2.14 are derived by the combination of literature calibrations as described in the main text. The black lines represent a linear relation fitted to the xCOLD GASS reference sample, see Eq. (2.15) and Eq. (2.16). The red dotted line is fitted to the CARS objects with the same slope as the black line, therefore highlight the shift in the normalization.

predicted from the combined Calzetti et al. (2007) and Lin et al. (2019) calibrations agree well with our data. This points to the notion that either the theoretical assumption made by Murphy et al. (2011) is inaccurate or that some of the ongoing star formation is completely obscured in $H\alpha$ which cannot be recovered with an extinction correction. Nevertheless, the xCG non-AGN sample can be used as a reference because the impact of extinction on the FIR/ $H\alpha$ ratio should be comparable to our AGN host galaxies. We therefore performed a linear fit directly on the xCG data and obtained the following relation which are shown as the black lines in Fig. 2.9:

$$\log\left(\frac{L_{\text{IR}}}{[\text{erg s}^{-1}]}\right) = 0.85 \log\left(\frac{L_{H\alpha}}{[\text{erg s}^{-1}]}\right) + 8.55 \quad (2.15)$$

$$\log\left(\frac{L_{\text{CO}}}{[\text{K km s}^{-1} \text{pc}^2]}\right) = 0.97 \log\left(\frac{L_{H\alpha}}{[\text{erg s}^{-1}]}\right) - 31.95 \quad (2.16)$$

Even though the CARS sample scatter is close to the comparison sample scatter, the CARS galaxies are on average located ~ 0.2 dex above the fitted L_{IR} to $L_{H\alpha}$ trend. The question here is whether this offset has a physical meaning or is just caused by low-number statistics and unknown biases of the CARS sample. Here, we claim that this offset is physical, based on two sets of evidence: 1) the CARS data are in a good agreement with the non-AGN reference sample on the L_{CO} to $L_{H\alpha}$ plot; 2) the training sample also has a few galaxies, located at similarly high $L_{\text{IR}}/L_{H\alpha}$ ratios which drive the offset in the CARS sample. The xCG objects in this specific area of the $L_{\text{IR}}/L_{H\alpha}$ diagram are almost exclusively populated with galaxy mergers according to the GalaxyZoo2 classification (Willett et al. 2013; Hart et al. 2016). Those mergers seem to have a lower instantaneous $\text{SFR}_{H\alpha}$ compared to the slightly longer timescale IR SFR, which can be expected from the rapid star formation history evolution and bursts of star formation on 100 Myr timescale that are observed and predicted by detailed galaxy simulation (e.g., Mihos et al. 1992; Barnes 2004; Springel et al. 2005; Di Matteo et al. 2008; Hopkins et al. 2013). Considering that the offset for the CARS sample is mainly caused by individual galaxies with similarly high $L_{\text{IR}}/L_{H\alpha}$ ratio, as in the non-AGN merger sample, some AGN host galaxies potentially had higher SFR in the past (over a ~ 100 Myr timescale).

Whether the potential difference in the star formation history is caused by a recent excess of star formation, which might actually be linked to a delayed BH growth (e.g., Wild et al. 2010), or by ongoing suppression of star formation as expected from AGN feedback remains unclear. To shed light on these different possibilities we discuss the difference between current and recent star formation as probed by $H\alpha$ and FIR emission in the following for individual objects where more information is available and can be interpreted.

2.4.3 Individual comparison of current and recent SFRs

In the previous subsection we compared different SFR tracers for the CARS sample with respect to the non-AGN comparison sample. Now we look at the SFR difference derived from the different SFR proxies for individual CARS galaxies and try to discuss the potential origins. We visualize the SFR results together with host galaxy morphologies and an indication for the AGN variability in Fig. 2.10. The AGN variability is set here by the brightness

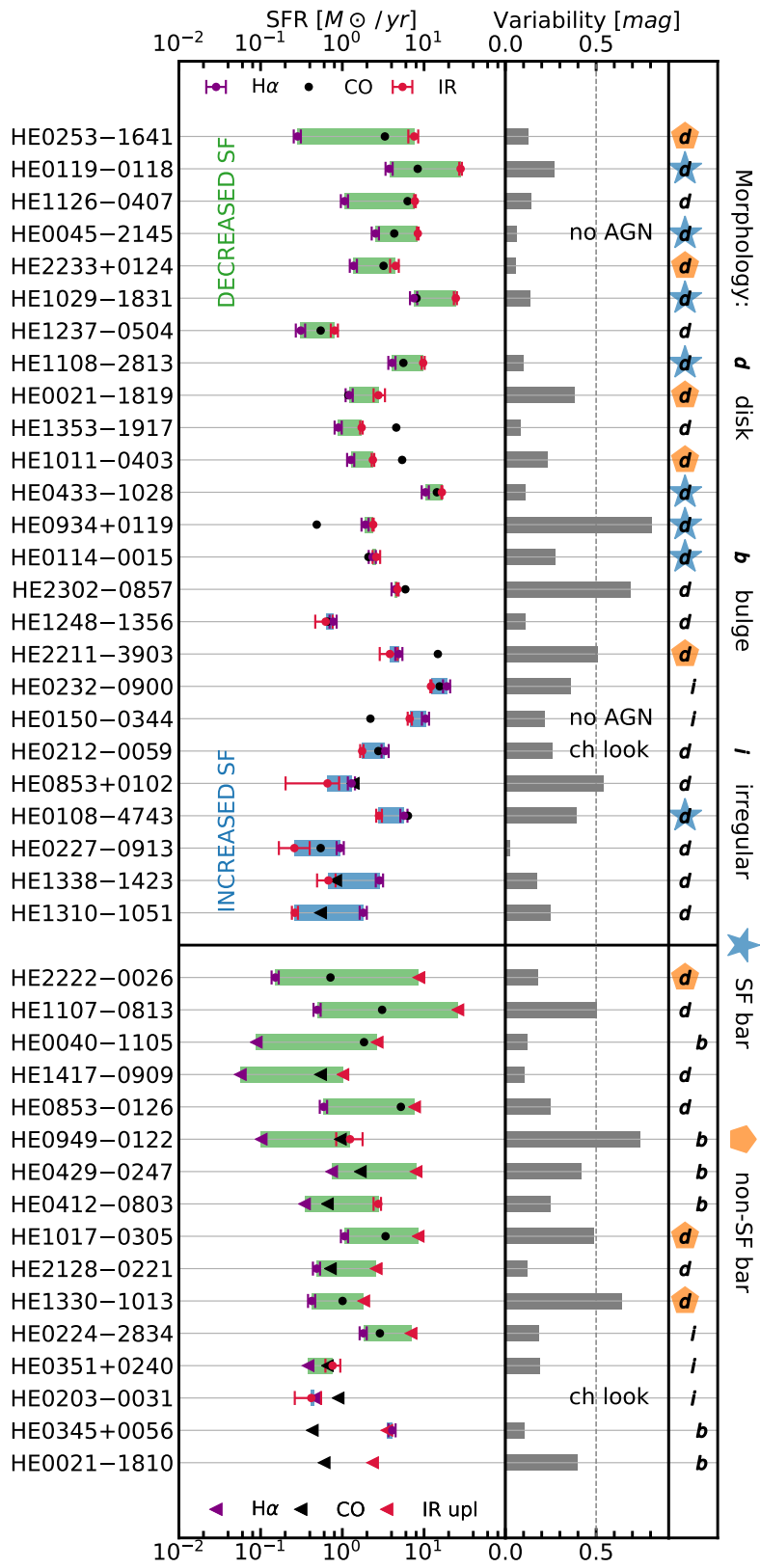


Figure 2.10: Comparison of SFR measurements for individual objects. *Left column:* H α -, IR-, and CO(1-0)-based SFRs for the CARS objects sorted by the SFR $_{\text{IR}} - \text{SFR}_{\text{H}\alpha}$ difference. *Central column:* near infrared variability; the objects with no AGN or known changing look AGN are also marked here. *Right column:* morphology of the host galaxies. Lower panel contains the objects with either H α and/or IR SFR uncertainties (upper limits or missing data).

difference in the NIR photometry between old 2MASS and more recent VISTA or PANIC observations separated by a few years. The H α -, IR- and CO-based SFR are again defined according to Eq. (2.2) and Eq. (2.1), respectively. We plot objects with upper limits in either of the SFR traces separately, as any difference between the SFR cannot be inferred on an individual basis.

The sign of the relative difference of H α - and IR-based SFR is highlighted in green and blue color when the IR-based SFR is higher or lower compared to H α , respectively. Assuming that the SFR timescale is the prime physical explanation for the difference (e.g., Hayward et al. 2014; Davies et al. 2015), where H α probes more recent star formation than the IR, we can in principle differentiate between declining or enhanced star formation. In Fig. 2.10 we order the objects from the strongest decline to the highest enhancement in SFR. The objects HE0253–1641, HE0119–0118, HE1126–0407, HE0045–2145, HE2233+0124 and HE1029–1831 belong to the declining SFR group and HE0150–0340, HE0212–0059, HE0853+0102, HE0108–4743, HE0227–0913, HE1338–1423, and HE1310–1051 belong to the galaxies with potentially enhanced star formation. Below we discuss different scenarios for those individual cases that may provide physical explanations, but certainly require further tests and observations to verify.

All of these galaxies are disk-dominated and none are bulge-dominated or strongly interacting systems. Strong interactions therefore seem to play a minor role, but we still identify cases where this might be important but not obvious. In addition, bars might suppress the star formation dynamically due to bar quenching (e.g., Khoperskov et al. 2018; Fraser-McKelvie et al. 2020), but we identified nonstar forming and star forming bars in the decreasing SF group, based on the analysis of Neumann et al. (2019). While the majority of the galaxies with declining SFR are indeed barred galaxies, most of them appear star-forming contrary to expectation if they would suppress star formation. AGN or starburst-driven winds may play a role in individual cases of HE 1126–0407 and HE 0045–2145, which have both declining SFR. HE 1126–0407 (aka PG 1126–041) is known to have a powerful ultra-fast outflow driven by the AGN (Wang et al. 1999; Giustini et al. 2011) which may couple more efficiently on kpc scales (Marasco et al. 2020) as the galaxy is significantly inclined with respect to our line-of-sight and central AGN engine orientation. Furthermore, HE 0045–2145 was misclassified in the Hamburg/ESO survey because of the broader lines caused by a starburst-driven outflow (Nevin et al. in prep.). In both cases the outflow might be related to the anticipated decline in SFR. The targets HE 0253–1641 and HE 0119–0118 show high gas dispersion in the AGN-ionized region on kpc scales (see Fig. B.1 in Husemann et al. 2022) which also points to a past or ongoing galactic outflow event in these systems. Such outflow signatures are much weaker in HE 2233+0124, but the galaxy is also more edge on with a misaligned ionization cone similar to HE 1126–0407 so that the impact of the AGN may be amplified. The cause of the potential decline in the SFR of HE 1029–1831 is less clear, but the stellar population modeling in high-angular NIR IFU spectroscopy with SINFONI revealed a recent circumnuclear starburst about 100 Myr ago that is rapidly declining (Busch et al. 2015). Although the cause of this decline is hard to directly link to AGN feedback or simple gas consumption, it clearly supports the timescale interpretation of the difference in the H α and FIR-based SFR.

For the objects with increased SFR, we identified HE 1310–1051 to exhibit a strong interaction with a minor companion (Husemann et al. 2014) and HE 0150–0344 to be a

strongly interacting non-AGN system. In those two cases, the interactions are most likely responsible for a recent burst of star formation. We cannot pin-point any obvious reasons why the star formation may be enhanced in HE 0212–0059, HE 0853+0102, HE 0108–4743, HE 0227–0913 and HE 1338–1423, but we note that the bolometric luminosity is close to the Eddington luminosity for the last three sources as reported in Husemann et al. (2022) due to their rather low BH mass with respect to the AGN luminosity. This is consistent with the scenario discussed in Husemann et al. (2022) that low BH mass AGN are likely to be observed in earlier phase of the AGN cycle. In this case, the circumnuclear starburst would be observed much closer than 100 Myr in time with respect to its peak activity. Indeed, narrow-line Seyfert 1 galaxies as high-Eddington ratio AGN show systematically higher SFR based on PAH emission detected with Spitzer (Sani et al. 2010) compared to the broad-line Seyfert 1 counterparts with lower Eddington ratios. This highlights the intriguing connection between the AGN and the circumnuclear starburst, where AGN with increasing SFR are potentially young AGN in a fueling mode powered by the starburst.

Lastly, we obtained some information on AGN variability as a side-product of our analysis when we compared old 2MASS NIR photometry with the more recent VISTA or PANIC observations. Interestingly, we see that the targets with declining SFR show systematically less variability on a few tens of years timescale. It is still speculative whether this points to a much more stable energy output of the AGN on longer timescales and thereby enhancing the impact as a cumulative effect of energy release over time. However, it shows that the process of AGN feedback is complex and the time evolution of the AGN phase with respect to the galaxy needs to be considered as well to get a comprehensive picture. Indeed, in current self-regulated feedback models (Gaspari et al. 2020 for a review) the AGN is expected to flicker on-off with rapid variability that increases toward low-mass systems often due to the chaotic cold accretion feeding the SMBH (e.g., Gaspari et al. 2015; Tremblay et al. 2018; Rose et al. 2019).

2.5 Summary and conclusions

In this chapter, we presented a complete census of the integrated SFR properties across the entire CARS sample using the multiwavelength data set available for this local AGN host galaxy sample. In particular, we inferred robust stellar masses and IR-based SFR from panchromatic SED modeling with AGNFITTER and H α -based SFR from a careful analysis of spatially resolved optical emission-line diagnostics with our new RAINBOW algorithm. Using the large xCG sample of local non-AGN galaxies as a control and training set we built different models to predict the SFR for our AGN host galaxies to investigate the role of the AGN in terms of star formation feedback. Our main conclusions from this analysis can be summarized as follows:

- We find that stellar mass alone is an insufficient proxy for the expected SFR in AGN host galaxies. The cold gas content and possibly the metallicity are crucial to consider in order to avoid artificial trends with AGN parameters that could mimic expected AGN feedback trends.
- No systematic suppression of SFR could be detected with respect to the non-AGN galaxy reference sample and there is also no trend with AGN luminosity.

- A potential link between lower than expected SFRs and the axis ratio b/a of the AGN host galaxies was identified. As our sample contains only unobscured AGN, the central engine (and thus the ionization cones) of low b/a systems must be mis-aligned with the galaxy rotation axis for inclined disks, leading to a higher cross-section of the AGN radiation field which can interact with the galaxy disk. This tentative trend is much weaker and currently insignificant for the SFR+gas model given the low-number of strongly inclined systems, but it may imply that such mis-alignments could amplify the coupling of the released AGN energy with the cold gas disk of the galaxy and thereby impact star formation more efficiently. This should be confirmed with bigger AGN host galaxies samples.
- Interpreting the IR and H α SFR tracers as proxies for the recent star formation history on ~ 100 Myr and ~ 5 Myr timescales respectively, we identified systems with decreasing or increasing SFR. The declining SFR cases might often be associated with galactic outflows while the increasing SFR cases can be associated with interaction or potentially with a young AGN phase.

That we cannot find any strong evidence for a global positive or negative AGN feedback on the SFR across the entire CARS sample is in agreement with various recent studies reporting no immediate impact of AGN on the star formation (e.g., Scholtz et al. 2020). We emphasize that predicting the expected SFR of galaxies is difficult, and using stellar mass alone may not be sufficient. The cold gas mass is fundamental, and its use in such relations allows one to capture the significant scatter in the star-forming main sequence (as already demonstrated in several works for the non-AGN population; e.g. Colombo et al. 2020; Popesso et al. 2020). Despite the lack of a global and obvious impact of AGN on star formation, we discover subtle effects that should be investigated in the future. Most importantly, the relative orientation of the AGN central engine and associated ionization cones may be relevant for the cross-section of release AGN energy and the cold gas of the galaxy. This is most prominent in disk galaxies and previously studied in several individual cases (e.g., Cecil et al. 2001; Morganti et al. 2015; Mahony et al. 2016; Mukherjee et al. 2018; Husemann et al. 2019), but CARS reveals a potential systematic trend that should be explored with larger samples.

The nondetection of a relation of AGN luminosity, BH mass and Eddington ratio with the global SFR may be related to the different time scales of the AGN phase and star formation in galaxies. In case the AGN phase is short, there would not be enough time passed to see the impact on the global star formation when selecting AGN samples rather than post-starburst system as discussed in the review of Alexander & Hickox (2012) and in Hickox et al. (2014). Indeed, the CARS sample suggests a potential correlation with the duration of a luminous AGN phase as a function of BH mass (Husemann et al. 2022), which is further corroborated by current models of AGN feedback self-regulated via chaotic cold accretion (e.g., Gaspari et al. 2020). The predicted durations are on the order of 1 Myr for a single AGN phase which would be clearly too short to suppress the star formation in the entire host galaxy and can explain our observations. Still, the circumnuclear SFR could be affected on these timescales. We observed interesting patterns of increasing and decreasing SFR by comparing the IR and H α SFR tracers among the sample that we can partially attribute to outflows, circumnuclear star formation and galaxy interaction. This highlights the potential of this approach, and also the complexity in the galaxy properties to be considered. We plan to

expand the diagnostics of the star formation history determination by inferring radio-based SFR for the CARS sample which probe intermediate SFR timescale of a few tens of Myr, filling the gap in the H α and IR-based SFRs. Furthermore, we expand our SFR investigation by zooming into the circumnuclear region of the galaxies in the CARS sample in the future. This requires the construction of an appropriate control sample with similar resolution which was beyond the scope of this thesis.

Overall, we identify cold gas content, relative AGN engine orientation with respect to the host galaxy, as well as the time domain variability as potential key parameters that need to be explored in the future to understand the impact of AGN on their galaxy on a population wide basis. This leads to obvious challenges in the sample selection, sample size and parameter space to be measured to gain more insights into the putative AGN feedback process.

Acknowledgments

We thank the anonymous referee for helpful comments that improved the quality of the manuscript.

We thank Mischa Schirmer for his support with the usage of the updated Theli pipeline v3.

Based on observations collected at the European Organization for Astronomical Research in the Southern Hemisphere under ESO programme 094.B-0345(A) and 095.B-0015(A).

Based on observations collected at the Centro Astronómico Hispano-Alemán (CAHA) at Calar Alto, operated jointly by Junta de Andalucía and Consejo Superior de Investigaciones Científicas (IAA-CSIC).

This project used data obtained with the Dark Energy Camera (DECam), which was constructed by the Dark Energy Survey (DES) collaboration. Funding for the DES Projects has been provided by the US Department of Energy, the US National Science Foundation, the Ministry of Science and Education of Spain, the Science and Technology Facilities Council of the United Kingdom, the Higher Education Funding Council for England, the National Center for Supercomputing Applications at the University of Illinois at Urbana-Champaign, the Kavli Institute for Cosmological Physics at the University of Chicago, Center for Cosmology and Astro-Particle Physics at the Ohio State University, the Mitchell Institute for Fundamental Physics and Astronomy at Texas A&M University, Financiadora de Estudos e Projetos, Fundacao Carlos Chagas Filho de Amparo á Pesquisa do Estado do Rio de Janeiro, Conselho Nacional de Desenvolvimento Científico e Tecnológico and the Ministério da Ciência, Tecnologia e Inovacao, the Deutsche Forschungsgemeinschaft and the Collaborating Institutions in the Dark Energy Survey.

Based on observations at Cerro Tololo Inter-American Observatory, NSF's NOIRLab (NOIRLab Prop. ID 2017A-0914; PI: Grant Tremblay), which is managed by the Association of Universities for Research in Astronomy (AURA) under a cooperative agreement with the National Science Foundation.

The Pan-STARRS1 Surveys (PS1) and the PS1 public science archive have been made possible through contributions by the Institute for Astronomy, the University of Hawaii, the Pan-STARRS Project Office, the Max-Planck Society and its participating institutes, the Max Planck Institute for Astronomy, Heidelberg and the Max Planck Institute for Extraterrestrial Physics, Garching, The Johns Hopkins University, Durham University, the University of Edinburgh, the Queen's University Belfast, the Harvard-Smithsonian Center for Astrophysics, the Las Cumbres Observatory Global Telescope Network Incorporated, the National Central University of Taiwan, the Space Telescope Science Institute, the National Aeronautics and Space Administration under Grant No. NNX08AR22G issued through the Planetary Science Division of the NASA Science Mission Directorate, the National Science Foundation Grant No. AST-1238877, the University of Maryland, Eotvos Lorand University (ELTE), the Los Alamos National Laboratory, and the Gordon and Betty Moore Foundation.

This publication makes use of data products from the Wide-field Infrared Survey Explorer, which is a joint

project of the University of California, Los Angeles, and the Jet Propulsion Laboratory/California Institute of Technology, funded by the National Aeronautics and Space Administration.

Herschel is an ESA space observatory with science instruments provided by European-led Principal Investigator consortia and with important participation from NASA.

This publication makes use of data products from the Two Micron All Sky Survey, which is a joint project of the University of Massachusetts and the Infrared Processing and Analysis Center/California Institute of Technology, funded by the National Aeronautics and Space Administration and the National Science Foundation.

This research has made use of the NASA/IPAC Infrared Science Archive, which is funded by the National Aeronautics and Space Administration and operated by the California Institute of Technology.

This research has made use of the APASS database, located at the AAVSO web site. Funding for APASS has been provided by the Robert Martin Ayers Sciences Fund.

Supported by the international Gemini Observatory, a program of NSF's NOIRLab, which is managed by the Association of Universities for Research in Astronomy (AURA) under a cooperative agreement with the National Science Foundation, on behalf of the Gemini partnership of Argentina, Brazil, Canada, Chile, the Republic of Korea, and the United States of America.

The SDSS is managed by the Astrophysical Research Consortium for the Participating Institutions. The Participating Institutions are the American Museum of Natural History, Astrophysical Institute Potsdam, University of Basel, University of Cambridge, Case Western Reserve University, University of Chicago, Drexel University, Fermilab, the Institute for Advanced Study, the Japan Participation Group, Johns Hopkins University, the Joint Institute for Nuclear Astrophysics, the Kavli Institute for Particle Astrophysics and Cosmology, the Korean Scientist Group, the Chinese Academy of Sciences (LAMOST), Los Alamos National Laboratory, the Max-Planck-Institute for Astronomy (MPIA), the Max-Planck-Institute for Astrophysics (MPA), New Mexico State University, Ohio State University, University of Pittsburgh, University of Portsmouth, Princeton University, the United States Naval Observatory, and the University of Washington.

3

Discovery of a global [C II] $158\mu\text{m}$ line excess in AGN HE 1353–1917

The [C II] $\lambda 158\mu\text{m}$ line is one of the strongest far-infrared (FIR) lines and an important coolant in the interstellar medium of galaxies that is accessible out to high redshifts. The excitation of [C II] is complex and can best be studied in detail at low redshifts. Here we report the discovery of the highest global [C II] excess with respect to the FIR luminosity in the nearby AGN host galaxy HE 1353–1917. This galaxy is exceptional among a sample of five targets because the AGN ionization cone and radio jet directly intercept the cold galactic disk. As a consequence, a massive multiphase gas outflow on kiloparsec scales is embedded in an extended narrow-line region. Because HE 1353–1917 is distinguished by these special properties from our four bright AGN, we propose that a global [C II] excess in AGN host galaxies could be a direct signature of a multiphase AGN-driven outflow with a high mass-loading factor.

3.1 Introduction

The [C II] $157.74\mu\text{m}$ emission line arises from the fine-structure transition $^2\text{P}_{3/2} \rightarrow ^2\text{P}_{1/2}$ of the ground state of singly ionized carbon C^+ (ionization potential of 11.2 eV). Working as a coolant in multiple phases of the interstellar medium (ISM), the [C II] line is one of the brightest emission lines in the far-infrared; it contributes 0.1–0.3% to the FIR luminosity.

The [C II] line has been calibrated as a probe for the cold gas content and associated star formation rates (SFR) in galaxies (Stacey et al. 1991; Boselli et al. 2002; Herrera-Camus et al. 2015). However, using the [C II] line as an SFR tracer is complex because of the multiple mixed excitation mechanisms of the line. In local star-forming galaxies, 66–82% of [C II] arises from the neutral gas of photodissociation regions (PDRs), and the rest comes from the ionized phase (Croxall et al. 2017). The mechanism of dust infrared emission, on the other hand, is rather simple: dust preferentially absorbs UV radiation from the stellar population and therefore is sensitive to the bright young stars. The infrared luminosity has been well calibrated as an SFR tracer at $\text{SFR} > 1 M_{\odot}\text{yr}^{-1}$ (Hirashita et al. 2003; Murphy et al. 2011) so that the [C II] and FIR luminosity are expected to be correlated.

At the highest SFRs, luminous and ultra-luminous infrared galaxies ((U)LIRGs) exhibit the so-called [C II] line deficit (Helou et al. 2001; Malhotra et al. 2001; Luhman et al. 2003), where [C II] becomes unreliable as an SFR indicator (Díaz-Santos et al. 2013). The origin of

the line deficit is still debated and is directly connected to physical processes that are crucial for understanding the [C II] excitation mechanisms.

Active galactic nuclei (AGN) are able to affect the [C II]/FIR ratio in several ways: they can increase the infrared luminosity through dust heating (Herrera-Camus et al. 2018a); act as an additional source of the [C II] excitation; or suppresses the [C II] line through the overionization of C⁺ to C^{2+,3+}, etc. with their hard radiation field (Langer & Pineda 2015). *Herschel* surveys of nearby galaxies such as KINGFISH (Smith et al. 2017) and *shining* (Herrera-Camus et al. 2018b) found no link between the [C II] line emission and AGN luminosity, but these AGN may be not luminous enough to outshine the star formation.

Given its brightness, the [C II] line is the most important ISM diagnostic at high redshifts that can be observed with unprecedented spatial resolution and depth on submillimeter interferometers. The sample of the observed high-redshift objects includes starburst and AGN-dominated systems, with the [C II]/FIR ratios spanning a wide range from 0.02% to 5% (e.g., Gullberg et al. 2015; Brisbin et al. 2015; Decarli et al. 2018). In order to provide an interpretation, we need to investigate the [C II] emission in local galaxies and determine the effect of luminous AGN.

In this chapter, we present [C II] line observations with the Stratospheric Observatory For Infrared Astronomy (Temi et al. 2014) for five nearby ($0.024 < z < 0.040$) luminous Seyfert 1 AGN host galaxies from the Close AGN Reference Survey to investigate the impact of AGN on the global [C II] luminosity.

3.2 Observations and analysis

3.2.1 SOFIA/FIFI-LS observations

We observed five CARS objects with the Far Infrared Field-Imaging Line Spectrometer (FIFI-LS; Klein et al. (2014)) on board SOFIA. The objects were picked to cover a broad range of SFRs ($1\text{--}11 M_{\odot} \text{yr}^{-1}$) and avoid the strong atmospheric absorption in the redshifted [C II] line wavelength region. The SFR estimates were initially based on the predictions calculated from the AGN-subtracted extinction-corrected H α line from observations obtained with the Mult-Unit Spectroscopic Explorer (MUSE, Bacon et al. 2010, section 3.2.2). The properties of the observed galaxies are listed in Table 3.1.

The observations were performed during SOFIA Cycle 4 (plan ID 04_0056, PI: Husemann) and Cycle 5 (plan ID 05_0077, PI: Husemann). FIFI-LS is a double-beam spectrometer that covers $1' \times 1'$ in the red channel (105–200 μm) and $0.5' \times 0.5'$ in the blue channel (50–125 μm), split up into 5×5 spatial pixels. We tuned the setups to cover the [C II] line in the red channel with spectral resolution of $R \sim 1200$ (250 km s^{-1}) and either [O III] 88 μm or [O I] 63 μm in the blue channel, depending on atmospheric transmission.

The pipeline-processed data are provided by the FIFI-LS team. We used LEVEL_3 science-ready data, which consist of a number of ~ 30 second exposures, to apply an additional selection (see Appendix A.2 for details) and background subtraction, and constructed data cubes with $6''$ sampling using the DRIZZLE algorithm (Fruchter & Hook 1997). To derive total [C II] line fluxes from the FIFI-LS cubes, we summed the spectra within an aperture with $36''$ diameter and fit the line shape with Gaussian profiles. The HE 1108–2813 and HE 2211–3903 spectra are well modeled by a single-Gaussian component, while the spectra

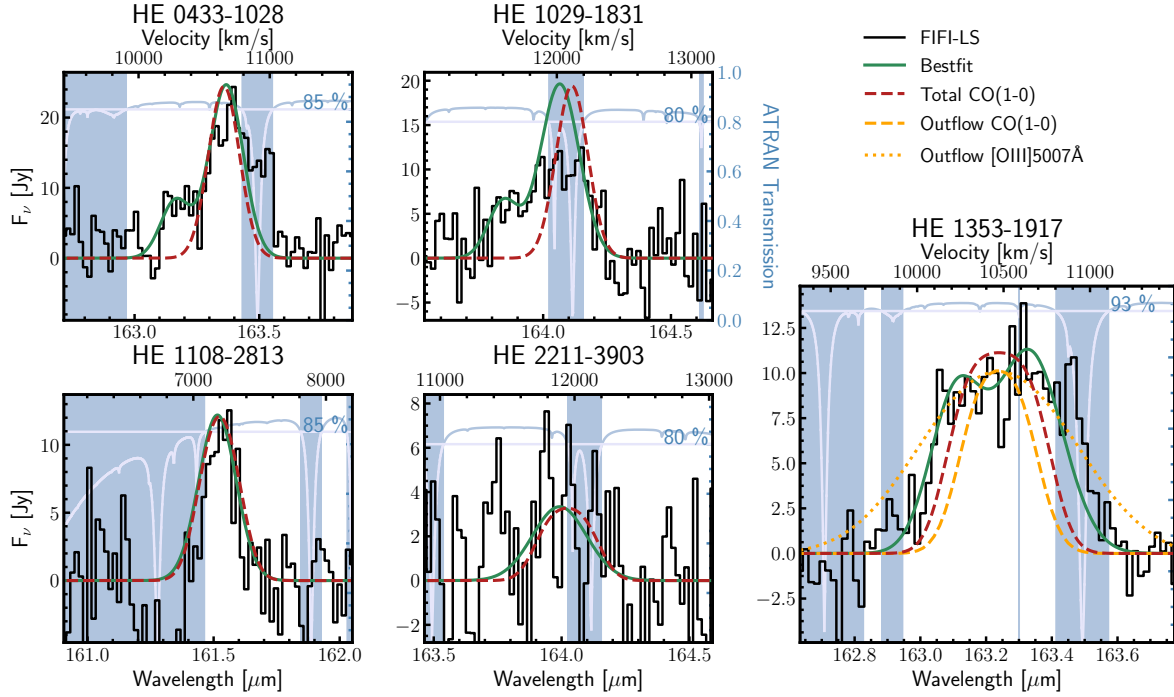


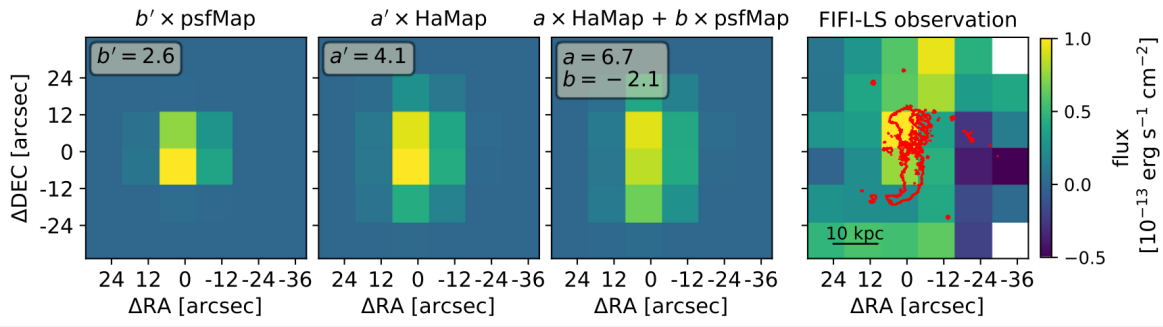
Figure 3.1: SOFIA/FIFI-LS [C II] spectra (black lines) for each object integrated within $36''$ diameter apertures. The CO(1–0) and best-fit Gaussian or double-Gaussian profiles are shown as red dashed and solid green lines, respectively. The CO(1–0) and [O III] 5007Å line profiles of the HE 1353–1917 outflow are shown as orange dashed and dotted lines. The comparison line profiles are degraded to the spectral resolution of SOFIA. The atmospheric transmission curves are shown in blue, and the shaded regions of low transmission are excluded from the analysis.

of HE 0433–1028, HE 1029–1831 and HE 1353–1917 require two Gaussian components. The spectra and the fitting results together with the excluded wavelength ranges due to the strong atmospheric absorption regions¹³ are shown in Fig. 3.1. In addition, we have analyzed the blue channel FIFI-LS data for HE 1353–1917 to estimate the upper limit of the [O III] 88 μm emission line flux $< 4.8 \times 10^{-13}$. The [C II] best-fit shape was used in the [O III] upper limit estimation, taking into account the spectral resolution of $R \sim 670$ (450 km s^{-1}) for the observed wavelengths.

HE 0433–1028 [C II] MAP

The FIFI-LS data of HE 0433–1028 is reported in Busch et al. (2018) as the first spatially-resolved SOFIA FIR observations of a nearby AGN. The [C II] line map is compared with the extinction-corrected and AGN-decontaminated H α line emission from MUSE and is found to be mainly matching the extended star formation with some additional flux present.

¹³Based on the ATRAN tool by Steve Lord,
<https://atran.arc.nasa.gov/cgi-bin/atran/atran.cgi>



The three models (left) are compared: a point source, an extended star formation emission predicted with $H\alpha$, and their linear combination. Each model is fitted to the observed $[C\text{ II}]$ line map from FIFI-LS obtained by integrating over the wavelength interval from $163.2\ \mu\text{m}$ to $163.43\ \mu\text{m}$. It becomes apparent that the line distribution is extended. In the fourth panel, the observed $[C\text{ II}]$ emission line map is shown with the overlaid red contours of $H\alpha$ from the MUSE cube.

Previous studies (e.g. Sargsyan et al. 2014) already suggested that $[C\text{ II}]$ can serve as a star formation estimator also in AGN but noted an increased scatter and a systematic overestimate of SFR in AGN by a median factor of 1.4. However, since the integrated measurements were compared, it was unclear whether the increased scatter comes from an additional component associated with the AGN or globally different scaling factors between $[C\text{ II}]$ and SFR. With FIFI-LS spatially-resolved $[C\text{ II}]$ observations and $H\alpha$ comparison data, we see that in HE 0433–1028, the extended emission of $[C\text{ II}]$ and $H\alpha$ are statistically matching, and yield scaling factors are consistent with inactive galaxies, with an additional flux excess North and South of the bar.

The material and the figure are taken from Busch et al. (2018).

3.2.2 VLT/MUSE observations

All five CARS targets were observed with MUSE at the Very Large Telescope (VLT) under ESO programs 094.B-0345(A) and 095.B-0015(A). The MUSE data cover $1' \times 1'$ FoV at a $0''.2$ spatial sampling and a wavelength coverage of $4650\text{--}9300\ \text{\AA}$ with $R \sim 2500$. Integration times range from $400\text{--}900\ \text{s}$ split up into two or three exposures, which are rotated by 90° against each other for cosmic-ray rejection and better image cosmetics. The data were reduced with the standard MUSE pipeline (version 1.6.0, Weilbacher et al. 2012, 2014).

As a first step of the post-processing, we subtract the bright point-like AGN emission from the reconstructed datacube using QDEBLEND^{3D} (page 30). Afterward we model the stellar continuum and ISM emission lines in the AGN-subtracted datacube with PYPARADISE (page 34).

In Fig. 3.2 we show the classical Baldwin-Philips-Terlevich (BPT, Baldwin et al. 1981) diagrams and corresponding spatial maps for the targeted galaxies after binning 8×8 pixels. Essentially, the BPT diagnostic diagrams highlight different dominating ionization mechanisms. The face-on galaxies display line ratios that are mainly consistent with star formation or intermediate line ratios between star formation and AGN excitation. The edge-on galaxy

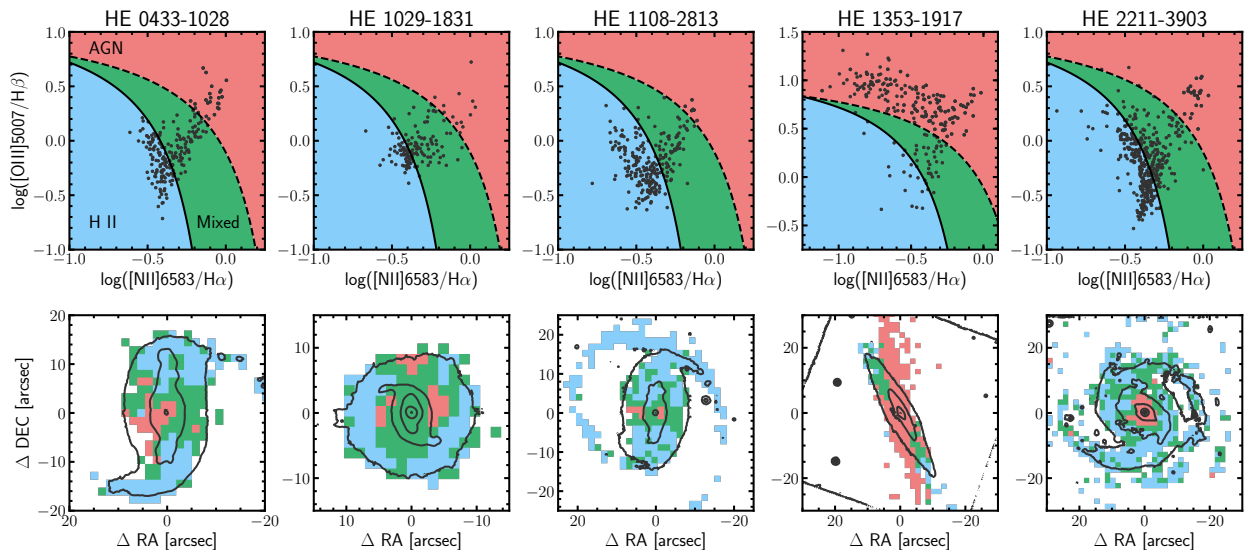


Figure 3.2: *Upper panel:* MUSE BPT diagnostic diagrams with empirical dividing lines. The solid line shows data from Kauffmann et al. (2003) and the dashed line from Kewley et al. (2001). The colors represent AGN ionization (red), ionization by H II regions (blue), and mixed regime (green). *Lower panel:* MUSE emission line $1.6'' \times 1.6''$ binned maps color-coded according to the BPT diagram regions; white-light contours are overplotted in black.

HE 1353–1917 is instead dominated by AGN photoionization. The fraction of AGN excitation to the extinction-corrected H α for HE 1353–1917 is $>80\%$, whereas a fraction of $<40\%$ is found for all face-on galaxies.

3.2.3 SED fitting and FIR luminosities

We constructed spectral energy distributions (SEDs) for all targets using publicly available broad-band photometry from the following catalogs: the *Herschel*/SPIRE Point Source Catalogue (Schulz et al. 2017), the AKARI/FIS Bright Source Catalogue (Yamamura et al. 2009), the 2MASS Extended Source Catalog (Jarrett et al. 2000), and the GALEX Source Catalog (Bianchi et al. 2017). For the following datasets we applied aperture measurements on the survey images: *Herschel*/PACS images from the Herschel Science Archive¹⁴, WISE Image Atlas (Cutri et al. 2011), optical *grizy* photometric images¹⁵ from the Pan-STARRS DR1 (Chambers et al. 2016), and Swift/UVOT images from the Barbara A. Mikulski Archive for Space Telescopes¹⁶.

We obtained the FIR (42.5–122.5 μm) luminosities through SED fitting with AGNFITTER (Calistro Rivera et al. 2016). AGNFITTER uses an MCMC approach and various template libraries to model the SED as a super-position of emission from an AGN accretion disk, a torus of AGN-heated dust, stellar light from the galaxies, and cold dust in star-forming regions. The AGNFITTER output SED models are shown in Appendix A.1 Fig. A.3 (the models used in this chapter do not take into account AGN constraints and differ from the

¹⁴HSA, <http://archives.esac.esa.int/hsa/whsa/>

¹⁵available at <http://ps1images.stsci.edu>

¹⁶MAST, <http://archive.stsci.edu/>

Table 3.1: Measured galaxy properties

Object	D_L [Mpc]	$F_{[\text{C II}]}$ 10^{-13} [erg/s/cm ²]	$F_{\text{FIR}}(42.5\text{--}122.5 \mu\text{m})$ 10^{-11} [erg/s/cm ²]
HE 0433–1028	156.4	6.13 ± 0.45	9.41 ± 0.05
HE 1029–1831	177.7	5.32 ± 0.83	9.82 ± 0.33
HE 1108–2813	104.7	2.65 ± 0.24	11.86 ± 0.32
HE 1353–1917	154.0	5.07 ± 0.32	1.11 ± 0.04
HE 2211–3903	175.2	1.17 ± 0.41	1.94 ± 0.25

models shown in Fig. A.2; but the FIR part does not depend on this change much) and the FIR (42.5–122.5 μm) luminosities are listed in the Table 3.1.

3.3 Results and discussion

The [C II] and FIR luminosities of our five targets are shown in Fig. 3.3 in comparison to a large literature compilation of low-redshift galaxies from Herrera-Camus et al. (2018a). Four of the CARS targets lie within the 3σ region of the mean relation (apparently, the [C II] emission is matching the star formation traced by $\text{H}\alpha$, for example, see HE 0433–1028 [C II] MAP box on page 61), while HE 1353–1917 lies above the relation with more than 7σ significance. The outlier has the strongest deviation from the mean trend (observed to the date of Smirnova-Pinchukova et al. 2019 publication, later LARS 5 with [C II]/FIR $\sim 9\%$ was observed also with SOFIA/FIFI-LS, Puschnig et al. 2020) at low redshift, with an unprecedented global [C II] line excess of an order of magnitude. AGN hosts and LINERs tend to be below the relation in the (U)LIRG regime $L_{\text{FIR}} > 10^{11} L_{\odot}$ and more likely show [C II] line deficits.

Based on the FIR and AGN-subtracted extinction-corrected $\text{H}\alpha$ luminosity, we expected HE 1353–1917 to be the faintest target in [C II], but it turned out to be the brightest source of our sample. While all galaxies have similar metallicities, stellar masses, and AGN bolometric luminosities, the obvious dissimilarity is the edge-on orientation of HE 1353–1917. When we consider the unobscured nature of this AGN, this means that the AGN ionization cone directly pierces the gas-rich disk of the galaxy. This leads to a large biconical extended narrow-line region (ENLR) that is oriented almost along the disk axis on kiloparsec scales, as clearly shown in Fig. 3.2. In addition, a massive multiphase outflow on kiloparsec scales with a mass outflow rate of $\dot{M}_{\text{out}} \sim 10\text{--}100 M_{\odot} \text{yr}^{-1}$ is detected in this galaxy, as discussed in detail by Husemann et al. (2019), while less prominent outflows are detected in the other four galaxies (Singha et al. 2022). The global SFR of $\sim 2 M_{\odot} \text{yr}^{-1}$ implies an integrated mass-loading factor of ~ 10 or more that has a similar scale as the observed [C II] excess.

Several powering sources may contribute to the [C II] line excess in HE 1353–1917, but the challenge is to distinguish the dominant [C II] line excitation mechanism. As highlighted in Fig. 3.3, the [C II] line luminosity of HE 1353–1917 cannot be powered by the star formation alone. The SFRs calculated from the extinction-corrected $\text{H}\alpha$ ($\text{SFR}_{\text{H}\alpha} = 1.23 \pm 0.03 M_{\odot} \text{yr}^{-1}$) and 42.5–122.5 μm luminosity ($\text{SFR}_{\text{FIR}} = 2.3 \pm 0.1 M_{\odot} \text{yr}^{-1}$) can account for only about 25% of the observed [C II] line luminosity ($\text{SFR}_{[\text{C II}]} = 2.286 \cdot 10^{-43} \times L_{[\text{C II}]}^{1.034}$, Herrera-Camus et al.

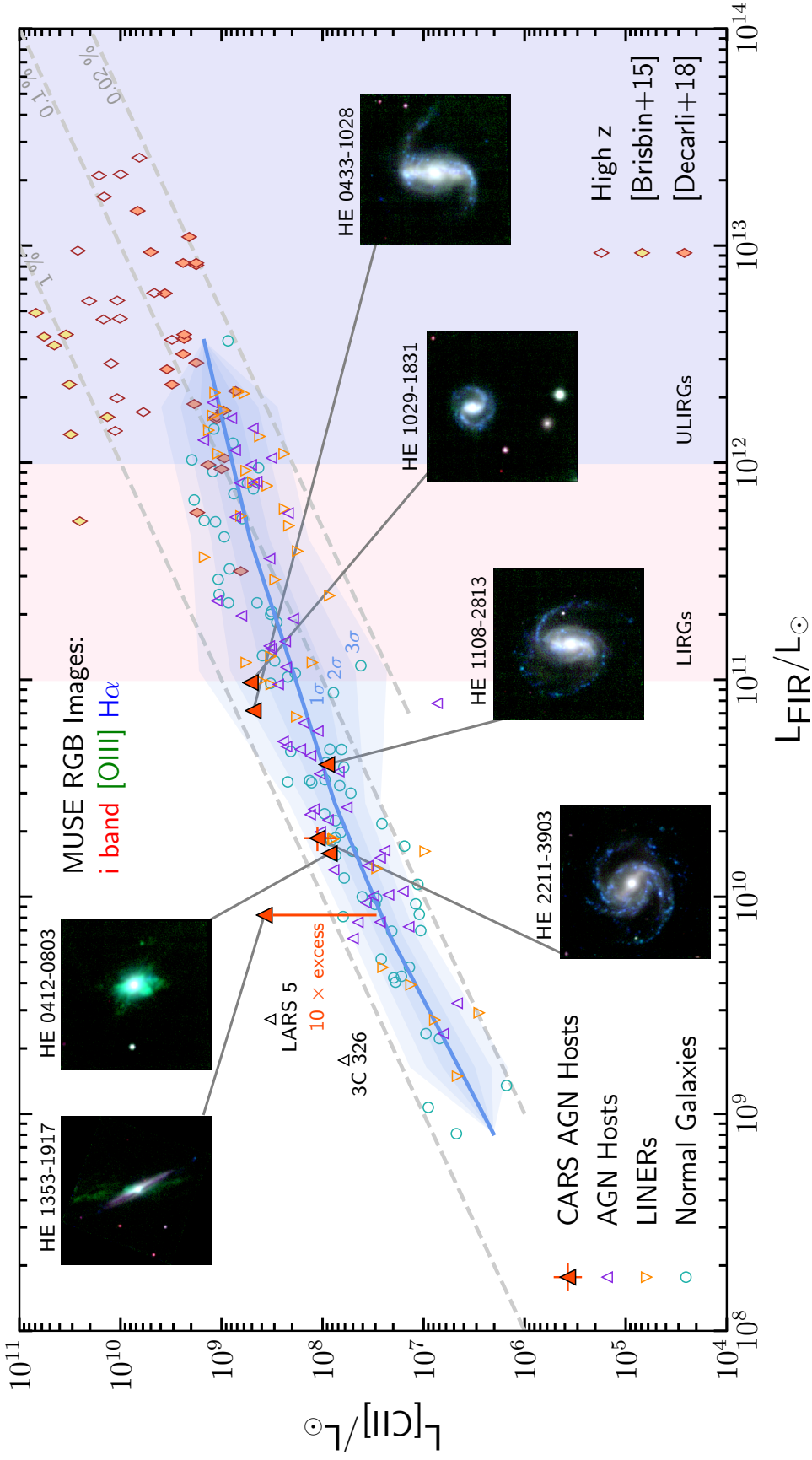


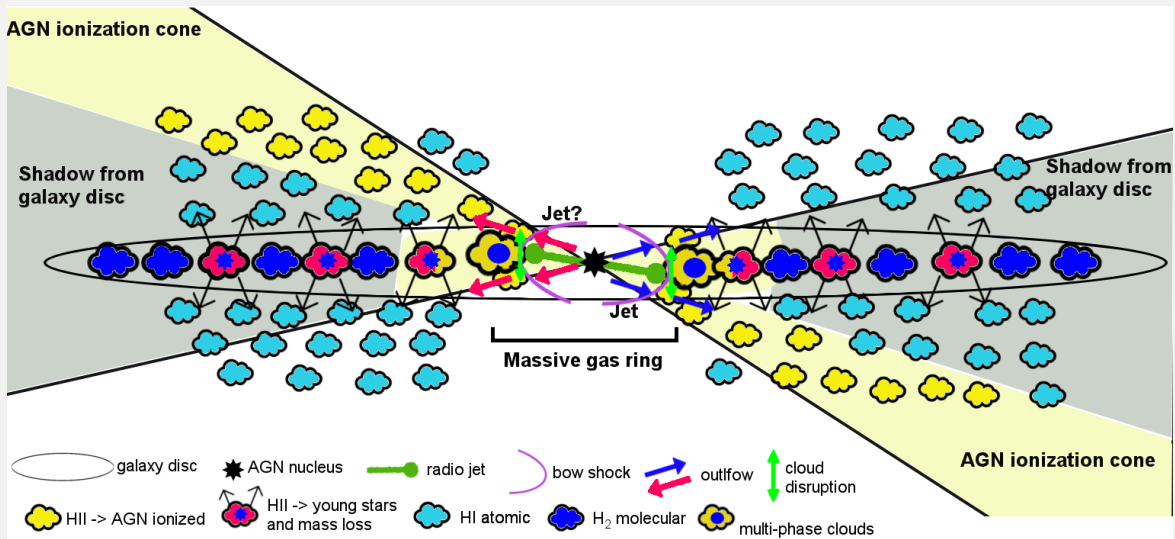
Figure 3.3: [C II] line luminosity as a function of FIR luminosity. Our five CARS targets (plus one follow-up, see section 3.5) are shown as red triangles compared to the literature compilation of Herrera-Camus et al. (2018a): normal star-forming and star-burst galaxies (green circles), AGN host galaxies (purple triangles), LINER galaxies (orange upside-down triangles), and high-redshift galaxies including the samples from Brisbin et al. (2015) and Decarli et al. (2018) (brown diamonds). The blue line is the mean of the low-redshift galaxies distribution, and the blue-shaded areas correspond to 1, 2, and 3 σ . Pink and purple shades represent LIRG $L_{\text{FIR}} > 10^{11}$ and ULIRG $L_{\text{FIR}} > 10^{12}$ regimes. The luminosities for 3C 326 are taken from Guillard et al. (2015) and for LARS 5 are taken from Puschignig et al. (2020) (black triangles).

2015). X-ray dominated regions (XDRs) produced by the hard X-ray photons from an AGN may contribute and even dominate the PDR [C II] emission. From the scaling relation $L_{[\text{C II}], \text{XDR}} = 2 \times 10^{-3} L_{2-10\text{keV}}$ by Stacey et al. (2010), we estimate an XDR contribution of only 10% given an X-ray luminosity of $L_{2-10\text{keV}} = 1.69 \times 10^{43} \text{erg s}^{-1}$ (Husemann et al. 2019).

[C II] emission can originate in any gas phase that is illuminated by UV photons. Using other line and continuum diagnostics, we can obtain some idea of which phases contribute to the [C II] emission, for example, 66–82 % for the neutral phase and the rest for the ionized phase in local star-forming galaxies (Croxall et al. 2017). However, these fractions do not necessarily remain the same in the ENLR of an AGN. How much of the [C II] emission originates from an ENLR has not been systematically explored so far. If the ionized gas phase produces more than 20–40 % of [C II] as in PDR paradigm, then it can explain the observed [C II] excess. In HE 1353–1917 only $\sim 20\%$ of $\text{H}\alpha$ originates from star-forming regions and $\sim 80\%$ comes from the AGN-ionized regions. If we naively assume that 20 % of the [C II] flux originates from star formation, the $[\text{C II}]_{\text{SF}}$ of HE 1353–1917 falls within 3σ of the [C II]–FIR relation.

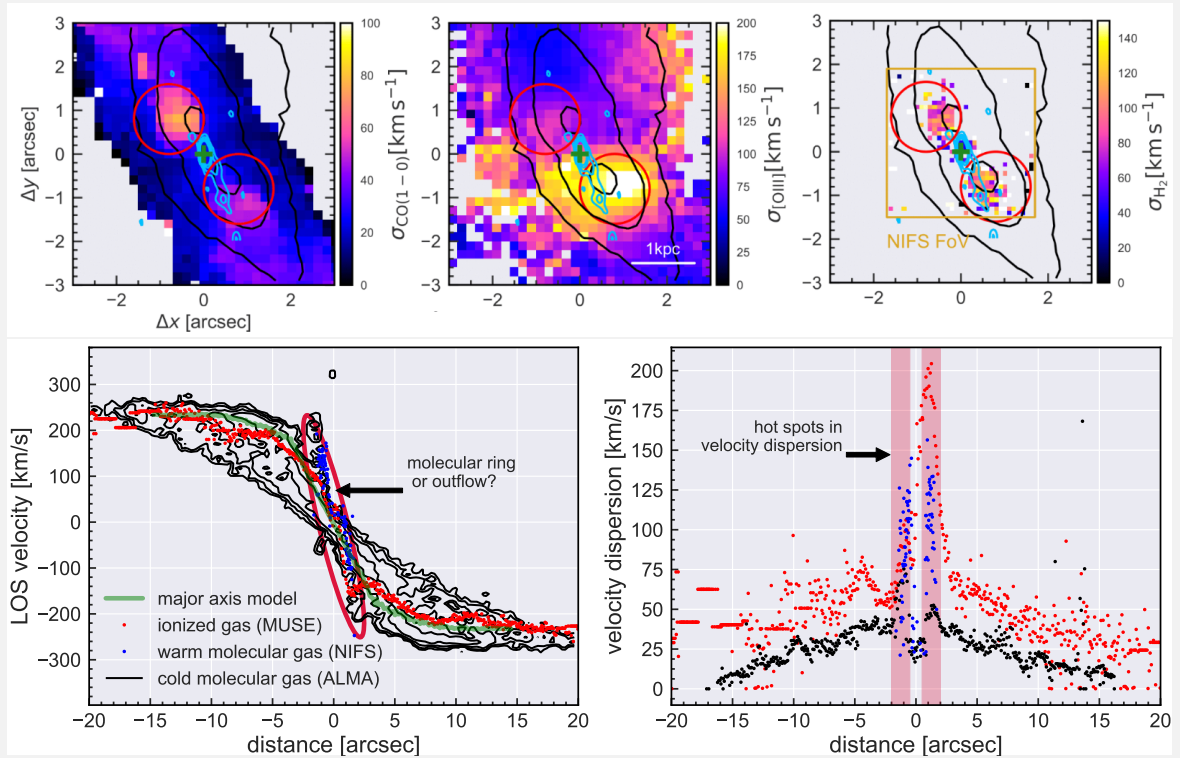
HE 1353–1917 STRUCTURE

In Husemann et al. (2019) HE 1353–1917 is analysed in detail with the observations from VLT/MUSE, Gemini-NIFS, ALMA, and VLA. Our understanding of the galaxy’s configuration is such, that the AGN ionization cones which are observed as a large biconical ENLR and a radio jet are nearly parallel to the galaxy disk (or perpendicular to the rotation axis of the disk).



The AGN ionization is then able to illuminate extra-planar material above the disk plane. The jet directly intercepts the cold gas disk of this galaxy, hitting the inner wall of a molecular gas ring which significantly enhances the cloud turbulence and disrupts the clouds in the vertical direction. The fast outflow in the ionized gas is then accelerated, either by the radiation pressure or the hot outflow from the jet, and

moving around the dense material at the inner edge of the dense gas ring in the disk plane.



The two well-defined regions highlighted in red circles on both sides of the nucleus in the cold-gas kinematics exhibit high velocity dispersion. On the multi-phase position-velocity diagram (PVD) along the major axis of the galaxy based on the CO(1-0), H₂[1 – 0S(1)] and [O II] ionized gas kinematic maps the LOS velocity and, in particular, the velocity dispersion most strongly deviates from the kinematical model in all gas phases about 1''5–2''0 away from the center on both sides. The warm molecular gas, which typically arises in strong shocks, is only detected at the location of those two “hot spots” supporting the notion that it is indeed a special region within the galaxy. Most importantly, we detect an extra-ordinary high velocity dispersion in the ionized gas phase at the same location, but only on one side of the galaxy centre. Given the high inclination and dust content of the disk, the assumption is that we cannot see the optical emission lines of the ionized gas on the other side of the nucleus due to the high obscuration.

A fast multi-phase outflow about ~1 kpc away from the nucleus is detected in the ionized gas ($v_{\text{max}} \sim 1000 \text{ km/s}$) and molecular gas ($v_{\text{max}} \sim 300 \text{ km/s}$). This region of the outflow appears as a distinct feature in the PVD and is coincident with jet-like radio emission at 10 GHz represented by light blue contours as detected with the VLA. Warm molecular emission is also directly associated with the radio jet location. This co-location implies that the ISM is heated directly through a fast moving shock, which is hitting the dense, cold gas disk of the galaxy.

The material and the figures are taken from Husemann et al. (2019).

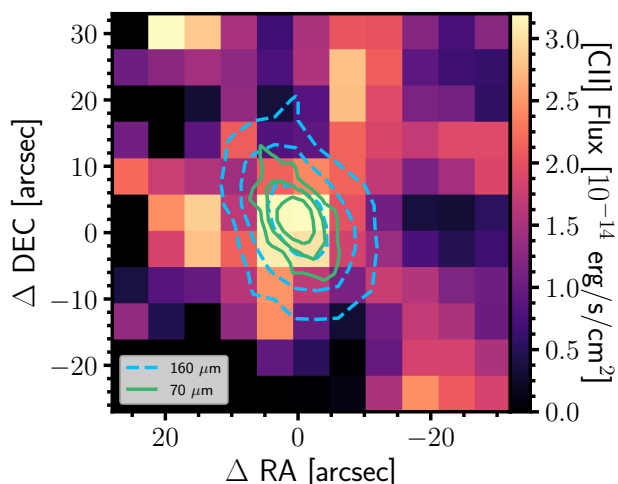


Figure 3.4: SOFIA/FIFI-LS [C II] line flux map of HE 1353 – 1917. The contours represent Herschel PACS 70 (solid green lines) and 160 μm (blue dashed line) photometric observations.

Dissipation of the kinetic energy of shocks and outflows can also have important consequences on the [C II] emission, as theoretically explored by Lesaffre et al. (2013). [C II]/FIR ratios of 3–7% are detected in between merging galaxies (Appleton et al. 2013; Peterson et al. 2018) and locally within galaxies (Appleton et al. 2018). On the global scale, the radio galaxy 3C 326 emits around 3% of FIR in [C II] line for which jet-driven turbulence is likely responsible (Guillard et al. 2015). Nesvadba et al. (2010) estimated an outflow rate in 3C 326 of $\dot{M}_{\text{out}} \sim 35 M_{\odot} \text{yr}^{-1}$, compared to the SFR $\sim 0.1 M_{\odot} \text{yr}^{-1}$ (Ogle et al. 2007), brings a mass-loading factor of >10 similar to that found in HE 1353–1917. HE 1353–1917 has a global [C II]/FIR ratio of $4.3 \pm 0.4\%$ and a radio-jet powering the multiphase gas outflow (Husemann et al. 2019). The [C II] line width of $760 \pm 60 \text{ km s}^{-1}$ is broader than the CO(1-0) line for cold molecular gas outflow $\sim 210 \text{ km s}^{-1}$, but narrower than the ionized gas outflow $\sim 1020 \text{ km s}^{-1}$ (see Fig. 3.1). [C II] therefore likely traces the interface between the warm and cold gas phase within the outflow. We can relate the region where the [C II] excess occurs to the center of the galaxy (Fig. 3.4) where the brightest region of the ENLR and the kpc-scale multi-phase outflow are indeed located. The [O III] upper limit implies a line ratio limit of $[\text{O III}]/[\text{C II}] < 0.96$, which suggests that the pure AGN ionization in the ENLR is not the primary cause for the [C II] excess. Hence, the observations are firm evidence that the [C II] line excess in HE 1353–1917 is related to the multiphase outflow initiated by the jet.

High-redshift galaxies span an entire range between [C II] deficient and normal regimes with [C II]/FIR ratios from 0.02% to 5%. The large scatter in the ratios may be caused by the order-of-magnitude difference in spatial resolutions, for instance, $18''$ for CSO, Brisbin et al. (2015) with average ratio of 1.8% and $1''$ for ALMA, Decarli et al. (2018) with average ratio of 0.08%, as low-resolution observations can include a larger fraction of intergalactic [C II] emission. Several high-redshift QSO have shown a [C II] enhancement (Maiolino et al. 2009; Wagg et al. 2010), which was interpreted as due to a low metallicity given the high [C II]/FIR and [C II]/CO(1–0) ratios in local dwarf galaxies. We measured [C II]/FIR $\sim 4\%$ and [C II]/CO(1–0) $\sim 10^4$ for HE 1353–1917, which can neither be explained by intergalactic [C II] emission nor by a low metallicity.

3.4 Conclusion

We presented the discovery of a global [C II] line excess in one out of five AGN host galaxies. Based on ancillary information from an extensive multiwavelength analysis of this galaxy as part of the CARS survey, we can directly connect the [C II] line excess in HE 1353–1917 to the impact of the AGN that drives a massive multiphase outflow on kiloparsec scales embedded in an ENLR (Husemann et al. 2019). The detection of such a global [C II] excess in AGN host galaxies is of crucial importance for the interpretation of [C II] line observations and the detection of massive gas outflows in luminous high-redshift AGN host galaxies. Given the evidence of HE 1353–1917 and the similar outflow seen in 3C 326, we propose that a significant [C II] line excess in luminous AGN, if detected, can be used as an inference for a multiphase AGN outflow with a high mass-loading factor even at high redshifts.

Acknowledgments

We thank the anonymous referee for helpful comments that improved the quality of the manuscript.

Based on observations made with the NASA/DLR Stratospheric Observatory for Infrared Astronomy (SOFIA). SOFIA is jointly operated by the Universities Space Research Association, Inc. (USRA), under NASA contract NNA17BF53C, and the Deutsches SOFIA Institut (DSI) under DLR contract 50 OK 0901 to the University of Stuttgart.

Based on observations collected at the European Organization for Astronomical Research in the Southern Hemisphere under ESO programme 094.B-0345(A) and 095.B-0015(A).

3.5 Follow-up observations

I proposed a follow-up SOFIA/FIFI-LS observation for another CARS AGN host galaxy to test if the discovered [C II] line excess in HE 1353–1917 is primarily linked to the ENLR or a multi-phase outflow. For this purpose, we chose HE 0412–0803, an elliptical galaxy with a low molecular gas content ($< 0.5 \times 10^9 M_{\odot}$, Bertram et al. 2007) but an extraordinary prominent ENLR and an AGN-driven ionized gas outflow. The two galaxies HE 1353–1917 and HE 0412–0803 are similar in terms of AGN luminosity and dominance of the ENLR, while the molecular gas content differs dramatically. The AGN ionized $H\alpha$ flux of HE 0412–0803 is nine times brighter than in HE 1353–1917 while the low molecular gas content limits the amount of shocked cold gas, which means that if the [C II] excess is caused by the ionized gas in the ENLR, SOFIA will detect an AGN-driven [C II] line excess. This observation helps us confirm or exclude our proposed [C II] excitation mechanism.

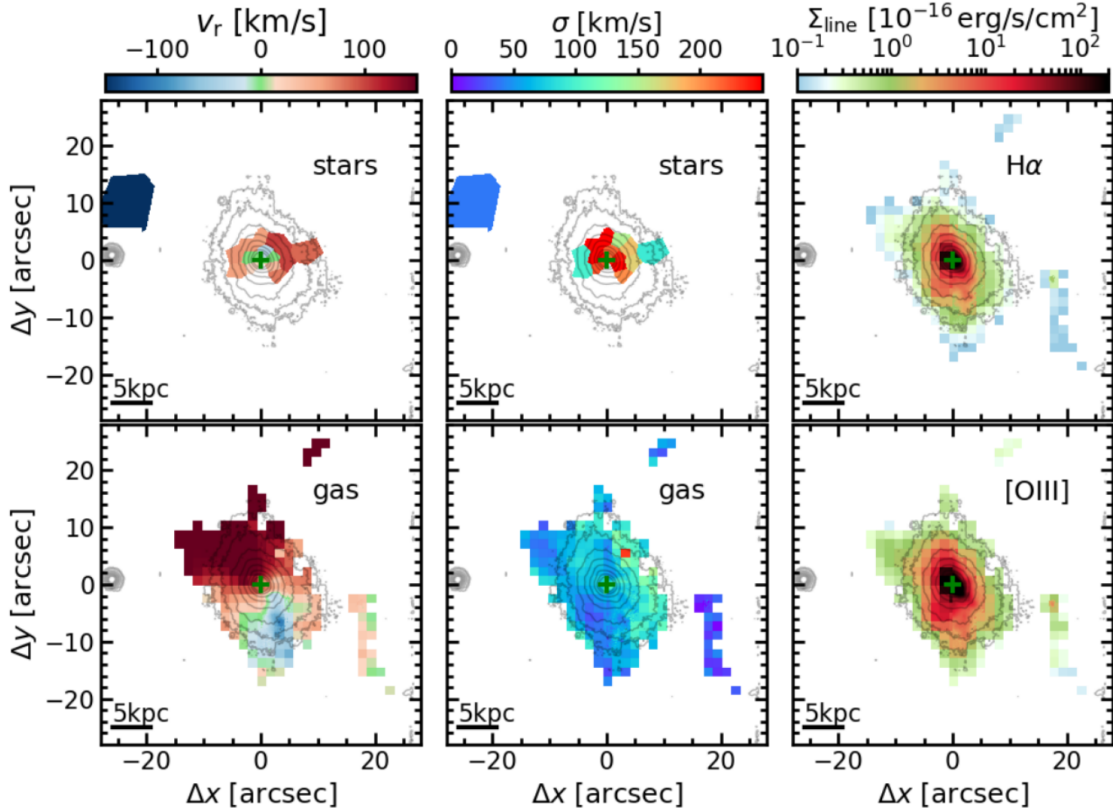


Figure 3.5: Results of the continuum and emission-line modeling (see PYPARADISE box on page 34) for HE 0412–0803. The radial velocity and the velocity dispersion of the stars and gas are shown in the first two columns, and the surface brightness maps of the $H\alpha$ and [O III] are shown in the right column. The figure is taken from Husemann et al. (2022).

3.5.1 No [C II] excess

The observations took place during SOFIA Cycle 7 (plan ID 07_0117, PI: Smirnova-Pinchukova) with the [C II] $158\mu\text{m}$ line in the red channel and [O III] $88\mu\text{m}$ line in the blue

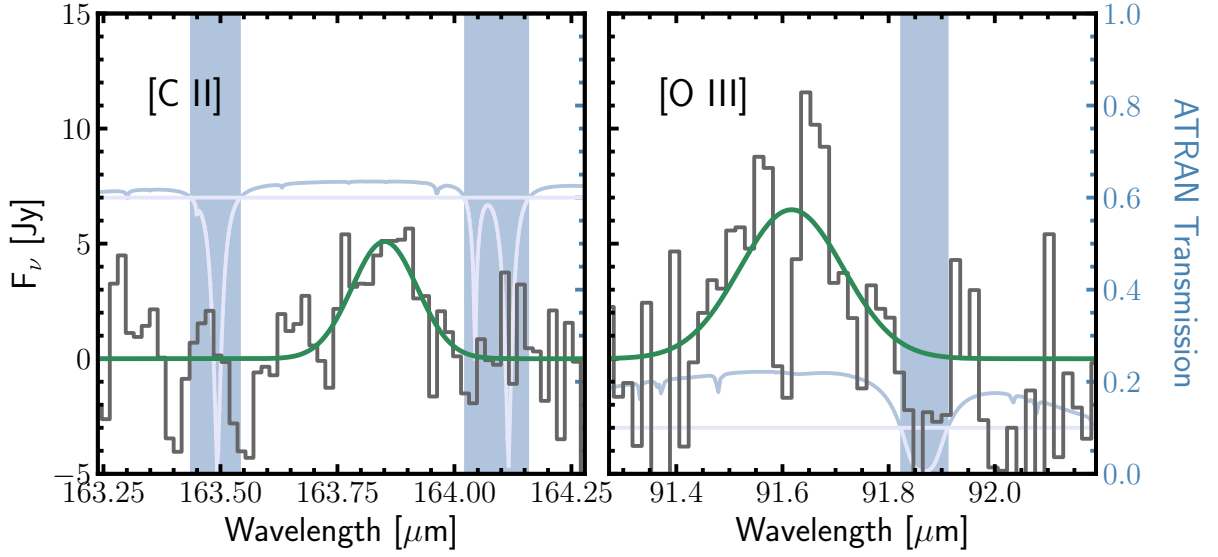


Figure 3.6: SOFIA/FIFI-LS [C II] and [O III] spectra (black lines) for HE 0412–0803 integrated within $36''$ diameter apertures. The best-fit Gaussian profiles are shown as solid green lines. The atmospheric transmission curves are shown in blue, and the shaded regions of low transmission are excluded from the fit.

channel. Observational characteristics and the modified data reduction are similar to the described before in section 3.2.1. HE 0412–0803 did not require any additional LEVEL_3 file selection (as described in Appendix A.2 for the previous observations), and a single Gaussian component was enough to fit the spectra within $36''$ diameter aperture (Fig. 3.6).

The [C II] flux of $1.012 \pm 0.216 \times 10^{-13}$ [erg/s/cm²] and the global [C II]/FIR ratio of 0.54% for HE 0412–0803 is in agreement with the low-redshift galaxies compilation from Herrera-Camus et al. (2018a), so no [C II] line excess is detected for the proposed galaxy. This means that the dominant ENLR alone cannot cause the [C II] excess, and the multiphase outflow in HE 1353–1917 is most likely responsible for the high [C II]/FIR ratio. Unlike in the previous observations, the [O III] 88.36 μ m emission line ($^3P_1 \rightarrow ^3P_0$ transition) that originates in the narrow-line region of AGN or H II regions with photon energies higher than ~ 35 eV, was also detected in the blue channel. The detected [O III] flux of $5.66 \pm 1.18 \times 10^{-13}$ [erg/s/cm²] results in [O III]/FIR = 0.032 and [O III]/[C II] ~ 5.6 . These ratios are among the highest values in the mentioned low-redshift sample (Herrera-Camus et al. 2018a), with the mean [O III]/FIR around 10^{-3} .

3.5.2 VLA puzzle

HE 0412–0803 was also observed on the Karl G. Jansky Very Large Array (16B-084, PI: Pérez-Torres) as part of the CARS survey. The observations took place on 5 January 2017 at C-band (centered at 6 GHz with a bandwidth of 4 GHz) and on 27 November 2016 at X-band (centered at 10 GHz with a bandwidth of 4 GHz) in the A configuration. The data reduction was performed with the standard CASA 6.2.1.7 procedure. The images have spatial resolutions of about $0''.33$ and $0''.2$ with RMS of 7.02μ Jy/beam and 8.39μ Jy/beam for C-band and X-band respectively. They reveal the spatially resolved

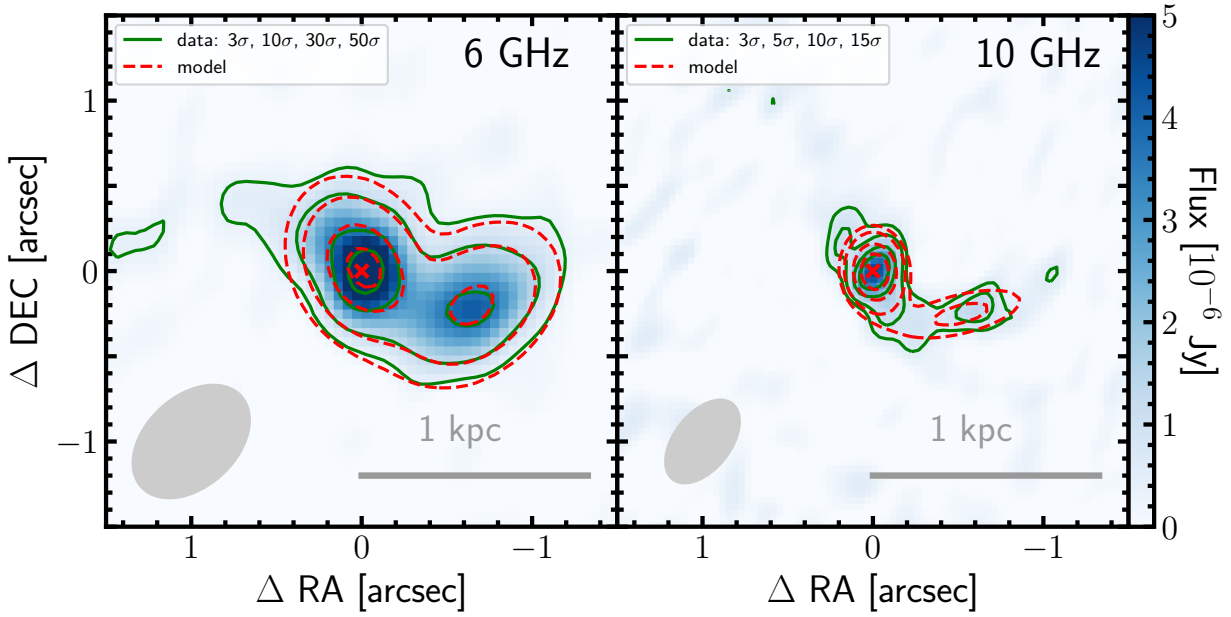


Figure 3.7: VLA C- and X-band continuum images of HE 0412–0803 with green contours representing $n\sigma$ levels, the red cross indicating the optical center, and the beam size shown in grey. Note that the flux density is in [Jy/pixel] (not in [Jy/beam]) to allow comparison while beam sizes are different. The two elliptical Gaussian components model is shown as red dashed contours with similar contour levels.

structure of two misaligned sources we call the primary and the secondary source (see Fig.3.7). The optical Seyfert 1 AGN source resides in the center of the primary radio source with robust accuracy of 13 mas for C-band and 4 mas for X-band. The parameters of the two elliptical Gaussian components model fitted with CASA tool are listed in Table 3.2.

The origin of the observed radio structure most certainly cannot be star formation. The MUSE H α total $\text{SFR}_{\text{H}\alpha} < 0.3$ (Table 2.4), the CO(1–0) $\text{SFR}_{\text{CO}} < 0.7$ (according to the CO(1–0) flux from Bertram et al. 2007 and equation 2.12), and the infrared SFR_{IR} is $4.2^{+0.2}_{-0.3}$ (Table 2.2). The NRAO VLA Sky Survey (NVSS, Condon et al. 1998) flux density

Table 3.2: Parameters of the two elliptical Gaussian component model.

	C-band			X-band			α^d
	F_{peak}^a [$\mu\text{Jy} / \text{beam}$]	$F_{\text{integrated}}^b$ [μJy]	PA ^c [deg]	F_{peak}^a [$\mu\text{Jy} / \text{beam}$]	$F_{\text{integrated}}^b$ [μJy]	PA ^c [deg]	
Primary	289.8 ± 9.5	611 ± 28	28.5 ± 4.2	157.0 ± 9.8	273 ± 25	point source	–1.2
Secondary	172.8 ± 9.4	436 ± 32	118 ± 16	45.1 ± 8.0	163 ± 37	100.8 ± 6.8	–2.6

^a Peak flux density.

^b Integrated flux density.

^c Beam deconvolved position angle.

^d Spectral index calculated as $\alpha = \log(F_{\text{peak}}^{\text{C-band}} / F_{\text{peak}}^{\text{X-band}}) / \log(\nu^{\text{C-band}} / \nu^{\text{X-band}})$.

is measured to be $8240 \mu\text{Jy}/\text{beam}^{17}$, which is the total flux of the galaxy considering $15''$ size of the beam. The corresponding total radio continuum $\text{SFR}_{\text{RC}}/[\text{M}_{\odot}\text{yr}^{-1}] = 0.75 \times 10^{-21} L_{1.4\text{GHz}}/[\text{WHz}^{-1}]$ (Heesen et al. 2014) would be $\sim 19 \text{M}_{\odot}/\text{yr}$, that is much higher than the other estimates.

Negative spectral indexes (also listed in Table 3.2) indicate synchrotron and inverse Compton emission, and therefore jet nature of the sources. NVSS total flux comparison with the estimations of 1.4 GHz flux ($F_{1.4\text{GHz}}$ estimated $\sim \left(\frac{1.4}{6}\right)^{\alpha} F_{6\text{GHz}} > F_{1.4\text{GHz}}$) show that the spectrum is likely not a simple power-law. We also do not resolve a core of the jet that is characterised by flat ($\alpha \sim 0$) or inverted ($\alpha > 0$) spectral indices.

There are two remaining scenarios capable of explaining the observed structure, with the two jet sources originating in one SMBH, the center of the Seyfert 1 AGN, or with the jets independently belonging to the two separate SMBHs. If this is one jet that comes from the Seyfert 1 AGN (the AGN resides in the brighter primary radio source), then what we see is a bent geometry where the jet changed the initial direction. This could happen due to interactions with the ISM (e.g., Wang et al. 2000; Lanz et al. 2015; Kukreti et al. 2022) or environmental interactions resulting in ram pressure and gas stripping (e.g., McBride & McCourt 2014; Gendron-Marsolais et al. 2021). We do not observe dense ISM that could heavily impact the jet direction, as there is not much CO(1–0) detected and no [C II] excess related to the shocked multiphase outflow. Nevertheless, the explanation with the ISM – jet interaction cannot be excluded because it could heat the gas leading to the observed lack of CO(1–0) flux. The MUSE gas kinematics map excludes gas stripping, HE 0412–0803 rather demonstrates signs of a major merger remnant with its elliptical morphology and mismatch of stellar versus gas kinematics (Fig. 3.5). This leads to another possible explanation, where both radio continuum sources are associated with two unresolved cores with their jets. In this dual AGN scenario, the primary radio source corresponds to the bright Seyfert 1 AGN that outshines its optically faint AGN companion visible as the secondary radio source.

While the existing data is not enough to distinguish the preferred scenario, future observations of HE 0412–0803 are needed to give a comprehensive answer. Singha et al. (2022) finds an extended structure in the center of HE 0412–0803, but MUSE Wide Field Mode (WFM) spatial resolution is not enough to resolve the central region of interest. Narrow Field Mode (NFM) observations with their resolution of $0''.025$ per pixel are, on the other hand, able to track the stellar kinematics within the central kiloparsec area and solve this VLA puzzle. Radio observations that track smaller spatial scales can also resolve the jet structure better and give us an idea of where the jet core (or cores) is.

¹⁷Available at <https://www.cv.nrao.edu/nvss/>.

Since the times when Edwin Hubble confirmed the extragalactic nature of the spiral nebulae, many things in our understanding of the Universe have changed. It is the galaxies that put the dark matter in the perspective of our world-built. Studies of stellar motions in galaxies and galactic motions in galaxy clusters show significant amounts of unseen matter. It is the galaxies that introduced the necessity of dark energy and led to such knowledge of space-time behavior. Standard candle supernova in distant galaxies show the expansion of the Universe to vary with redshift. This expansion is now described with a well-established Λ CDM cosmology as a framework of extragalactic astrophysics. What else the humanity finds out thoroughly investigating galaxies and their evolution?

In the current scientific paradigm, the picture of galaxy evolution is relatively complete but blurred. We know that galaxies and galaxy clusters form in the knots of the dark matter web, we know that the stars form in the cold molecular clouds; that star-formation in galaxies is affected by supernova and AGN feedback, morphological and environmental factors; the BHs accrete material, merge, and grow up to enormous weights of SMBHs; that galaxies are going through many stages during their life, evolving, merging with other galaxies, shining with AGN, quenching star formation and rejuvenating it again... But the details of every process open hundreds of questions. Digging into the elements of the galaxy evolution sharpens the picture, and the clearer we see, the more we understand the physics of the world we are living in.

Summary and outlook

In this thesis, I applied the best methods and approaches I could use; some of them were novel. Here, I summarize the results of my work and convey my hopes that the seeds I planted will grow valuable for "sharpening the picture of galaxy evolution".

My task in the CARS data release preparation was handling the star formation analysis described in Chapter 2. I accurately gathered and prepared all available photometry from the catalogs and image archives (section 2.2.1, 3.2.3) complimented by broad-band observations the CARS team performed (section 2.2.3), including the WFI observations I participated at La Silla observatory, to model the SEDs. As we deal with AGN, I tried to match the photometry with the observation dates closer to each other to avoid AGN variability impacts; as a by-product of this attempt, I list the NIR variability later in section 2.4.3. For the

modelling I modified the AGNFITTER package by Calistro Rivera et al. (2016), adding the constraints to the accretion disk model with direct AGN g and i magnitudes, obtained from the 2D image synthesis with GALFIT, as described in section 2.3.1 and the QDEBLEND^{3D} box on page 30. This modification allowed to reduce the uncertainty of the calculated parameters, especially the stellar mass. The option of providing the AGN constraints for the SED fitting of AGN host galaxies is being implemented in newer codes such as FORTESFIT by David Rosario (2019) therefore, the AGNFITTER results for the CARS sample are useful for the comparison and verification of the codes.

I utilized MUSE IFU cubes, the core dataset of CARS, rich with both spatial and spectral information, to obtain the recent SFRs (section 2.3.2). The new approach to handling BPT mixing sequences (section 2.3.2.2) led to the development of the RAINBOW code, which has a clear idea (inspired as a consequent increase of basis spectra by Davies et al. 2017) and simple usage. Combined with, again, a novel BPT morphologies approach (section 2.3.2.3), it allowed me to handle the diverse BPT variations of predominantly star-forming, AGN-dominated, or merging AGN hosts. I understand that new methods are not necessarily the best or optimal ones. Of course, the BPT morphology approach plus mixing sequence modeling with RAINBOW is more complicated than the demarcation line approach (section 2.3.2.1); it has some ambiguities in defining the spatial boundaries of the BPT morphology populations and in picking the basis spectra. Nevertheless, with some machine learning solutions, this novel approach will be applicable for much larger IFU surveys such as MaNGA, SAMI galaxy survey (Croom et al. 2021), and the future Hector galaxy survey (PI: Julia Bryant) to leverage the complete information content of the data.

With the obtained stellar masses and H α - and IR-based SFRs, I re-calibrated the SFMS for the CARS AGN hosts. The statistical characteristics and the equations in section 2.4.1 allow us to predict SFRs for the AGN host galaxies using stellar masses, cold gas contents, and metallicities (section 2.3.3). As finding any trends between AGN parameters and star formation is a challenge for observational astronomy, we propose the mutual orientation of AGN ionization cones and galactic disk, which is quantified as galaxy inclination in our research, given that we have only type 1 AGN, for further investigations. The idea is that if such AGN orientation allows the radiation to affect the host galaxy in a more efficient way, we observe AGN feedback effects more likely (see, for example, HE 1353–1917 STRUCTURE box on page 66).

As the title of the thesis is "Comparison of different star formation tracers in nearby AGN host galaxies", the comparison is made in section 2.4.2. Such matching can unveil the star formation history and help draw statistical connections between star formation and galactic events like AGN or merging. This is indeed a promising approach for understanding AGN feedback, as with H α the recent star formation on the timescales of 5 Myr is traced, with IR longer timescales of 100 Myr, allowing to indicate whether the SFR is increasing or decreasing. There is also a potential to add radio-based SFR that traces intermediate timescales of 15-20 Myr.

I analyzed CARS as a statistical sample, but it is also a collection of individual galaxies with their peculiar features. In section 2.4.3 the possible physical reasons for the decreasing and increasing star formation history traits are discussed. I thereby propose more of the subtle trends that we cannot clearly explain for future studies, observations, statistical checks, and modeling. Why do we see star-forming bars in the galaxies with declining SFR?

Don't bars dynamically support SFR suppression? Are early stages of AGN associated with the increasing SFR because of the circumnuclear starbursts that fuel AGN, and therefore are a reason AGN started to shine? Do less variable AGN have a more stable energy output and suppress star formation better?

Some individual cases are worth looking into with great detail, as they may represent an entire group of galaxies and provide statistical explanations. HE 1353–1917, the main character of Chapter 3, is an excellent example of the [C II] excess galaxies. Another example is LARS 5, the galaxy from Lyman- α Reference Survey, which I helped to analyze in Puschnig et al. (2020). Those discoveries would be impossible without a modified data reduction. Extragalactic sources are fainter than what SOFIA with FIFI-LS used to observe, so I took the intermediate data reduction step and applied the DRIZZLE algorithm to avoid over-smoothing of the low SNR data, together with some additional background subtraction and frame selection (section 3.2.1); only then the [C II] flux was possible to extract correctly. The data reduction modifications were not implemented in the official FIFI-LS data reduction, as extragalactic observations are not so common for the instrument, and the future possibilities are closed now together with SOFIA. Still, I was figuring as a contact person to check if there is any signal possible to infer from the low SNR data. The description in section 3.2.1 and Appendix A.2 and the availability of the DRIZZLE code at https://gitlab.com/SPiIrina/drizzle_fifi are sufficient if any FIFI-LS archival data is required to be analyzed.

The high-redshift galaxies exhibit a large scatter in the [C II]/FIR, and the detailed analysis of nearby [C II] excess cases is key to interpreting this scatter. The [C II] line is often used as a SFR tracer detectable with ALMA for the high- z galaxies, right when they have a peak of star formation at redshifts 1 – 3. With this work and the support of other literature cases, I claim that in AGN galaxies, the high [C II]/FIR is an indication of a multiphase AGN outflow, and the [C II] line alone is not informative of the SFR.

The follow-up SOFIA observations of HE 0412–0803 (section 3.5) were dedicated to confirming the scenario of multiphase outflow being responsible for the [C II] excess (or adding more points to the alternative ENLR scenario). While no [C II] excess is detected in HE 0412–0803 as there are likely no significant amounts of cold gas, this galaxy turned out to be intriguing on its own. In section 3.5.2 I discuss the origins of the double-sourced radio continuum structure of HE 0412–0803 observed with VLA. Whether HE 0412–0803 has a jet that changed its direction for an unknown reason or this galaxy hosts a dual AGN as a result of major merging — only the observations of the inner kiloparsec area will be able to give us an answer. While the CARS team already proposed this source for the upcoming ALMA cycle, other high-resolution observations with, for example, optical MUSE NFM or radio VLBA can reveal the nature of the two radio sources we see on the VLA images.

Overall, this thesis gives the perspective of handling SFR accessed by multiple tracers in the conditions of AGN contamination. AGN studies are still at the peak of their relevance for a decade, with more projects coming up. Bigger ground-based and space telescopes, bigger bases of radio interferometers, and better data analysis capabilities with machine learning, not to mention better experience in handling big data. Recent surveys, including CARS, show the power of the multiwavelength approach; soon, with the new observational windows such as gravitational waves and high-energy particles joining the "spectrum", the

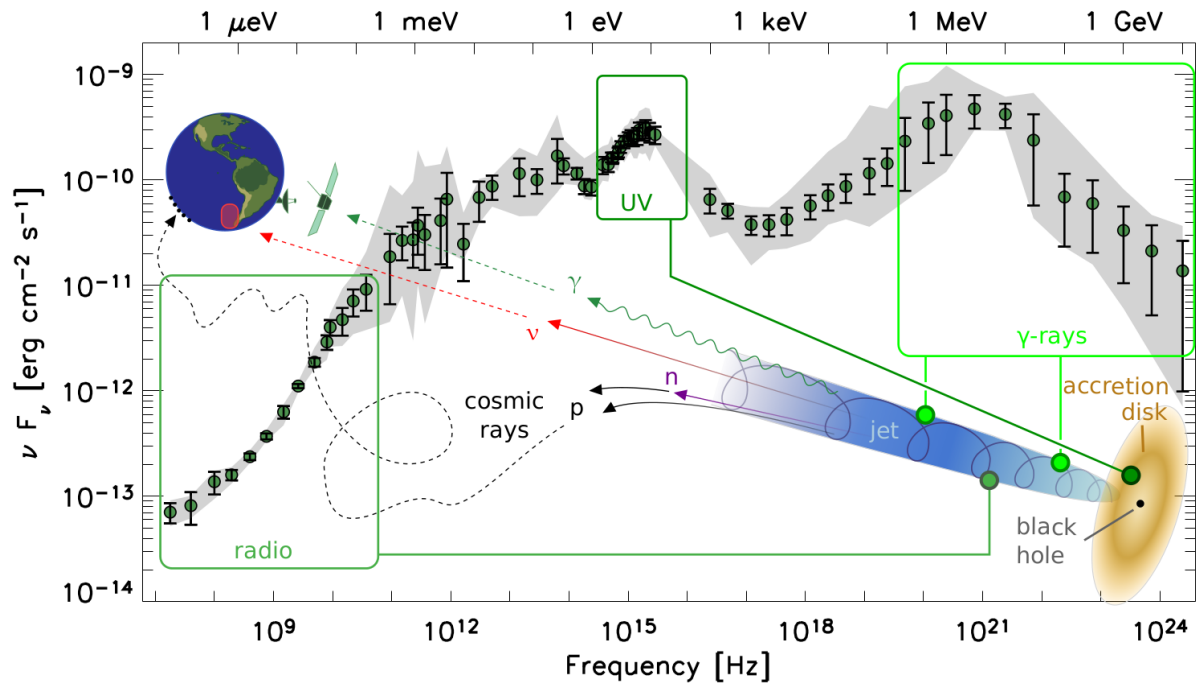


Figure 4.1: An illustration of AGN multi-messenger emission taken from Rani et al. (2019). The background spectral energy distribution of 3C 273 and its variations spanning from 4 to 44 years of observations depending on the wavelength is taken from Soldi et al. (2008).

multi-messenger era comes. This will lead to a fuller population of black hole demographics, a better understanding of black hole growth and jet physics, more cases of dual AGN and connections with galaxy mergers, direct imaging of the inner AGN structures, and a better understanding of AGN fueling and feedback.

A.1 Figures for the CARS objects

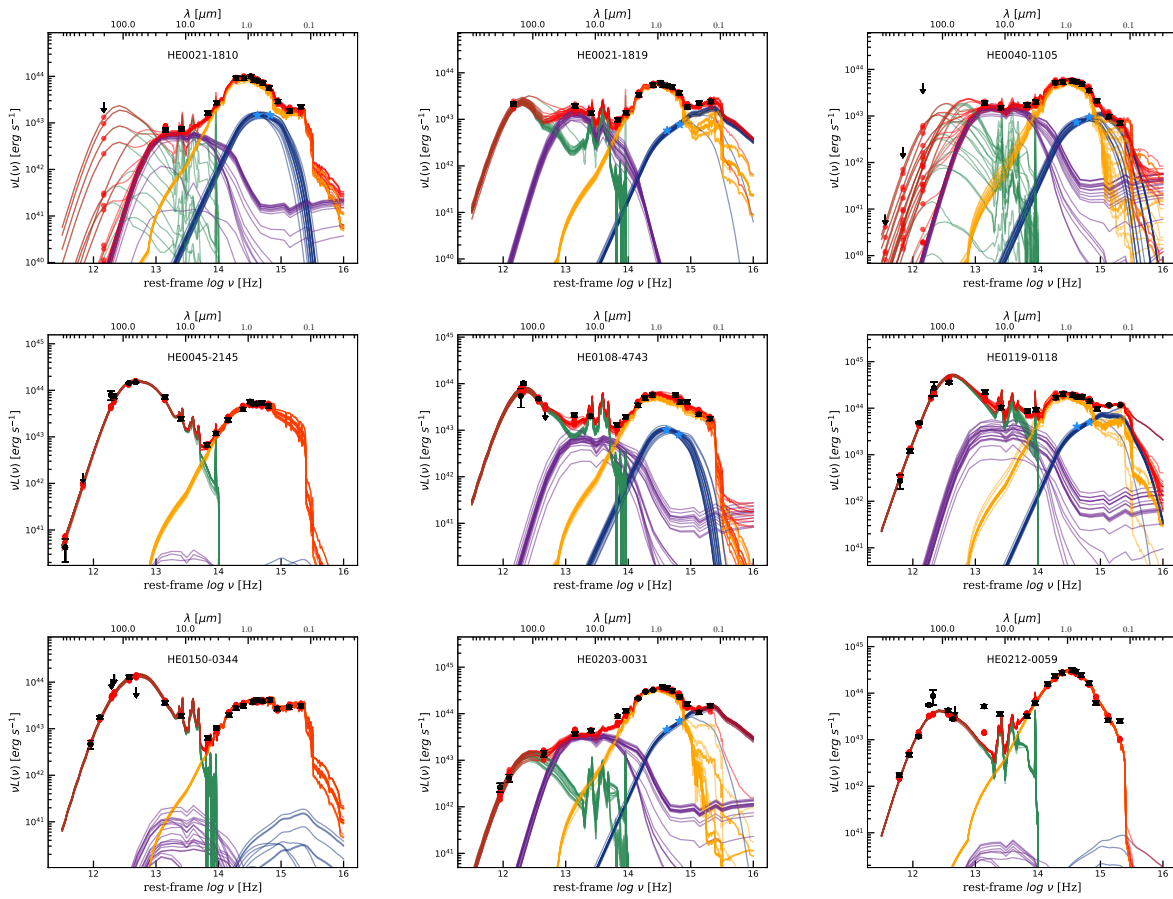


Figure A.2: Overview of the AGNFITTER SED modeling results for the entire CARS sample. Black data points represent the measured panchromatic photometry collected for each object. Upper limits are highlighted as black arrows. The red dots are the predicted photometry for MCMC relations from the superposition of individual SED components. The red, yellow, blue, purple and green lines correspond to the total SED, the stellar component, the AGN component, the hot dust component and the cold dust component, respectively.

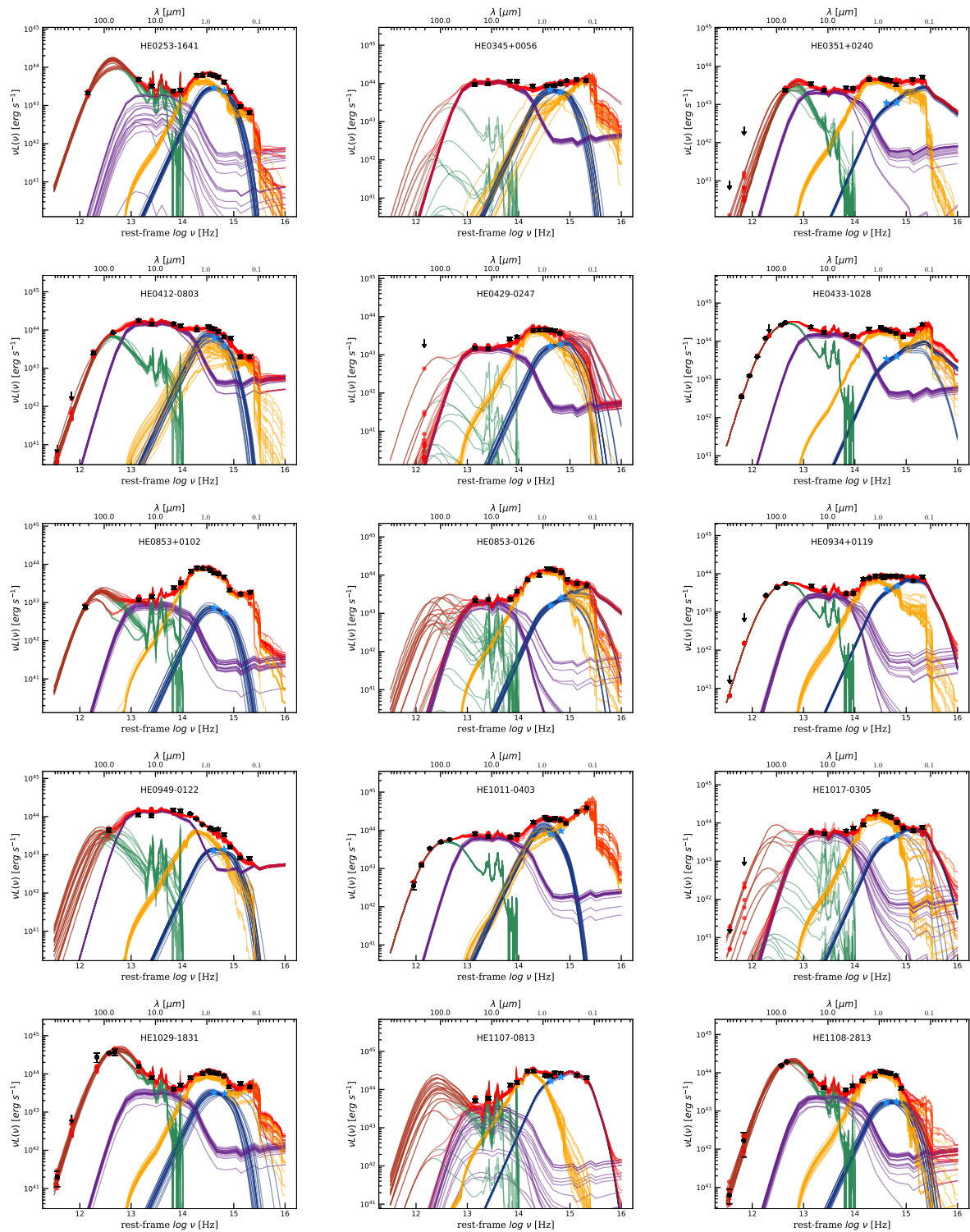


Figure A.2: continued.

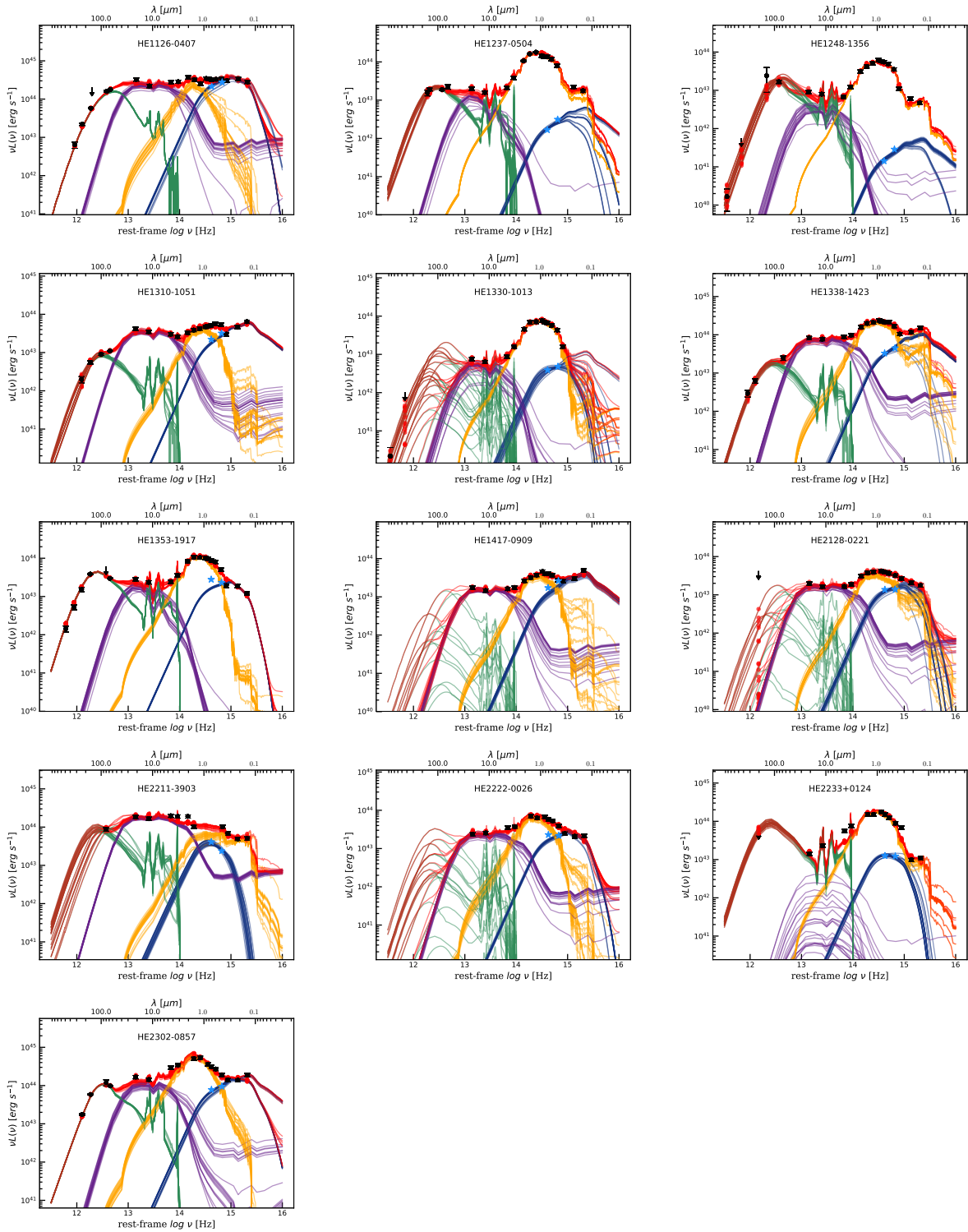


Figure A.2: continued.

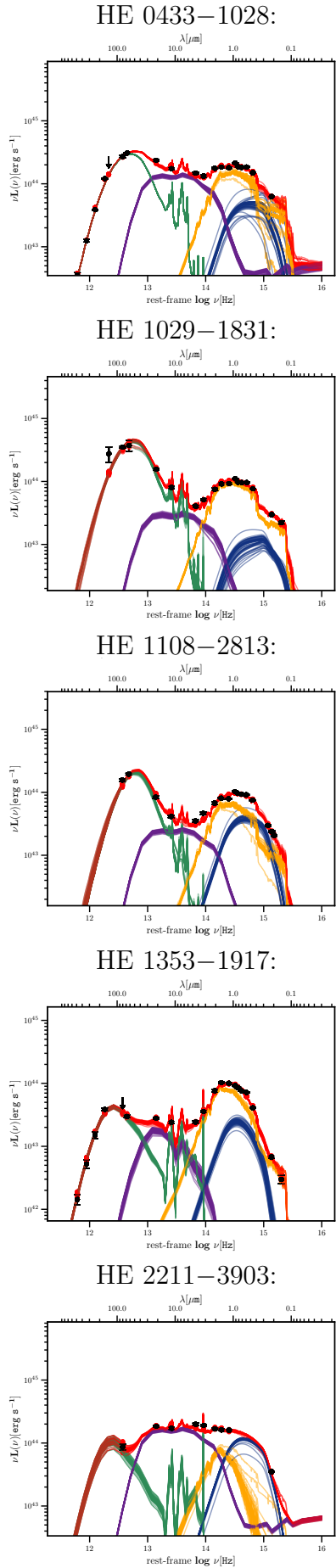


Figure A.3: Reconstructed SED for the five CARS objects observed with FIFI-LS and best-fit SED model determined by AGNFITTER (Calistro Rivera et al. 2016). 50 MCMC realizations fit to the broadband photometric data (black points with error bars) are shown. The model description is similar to the one in Fig. A.2; the AGN constraints are not introduced.

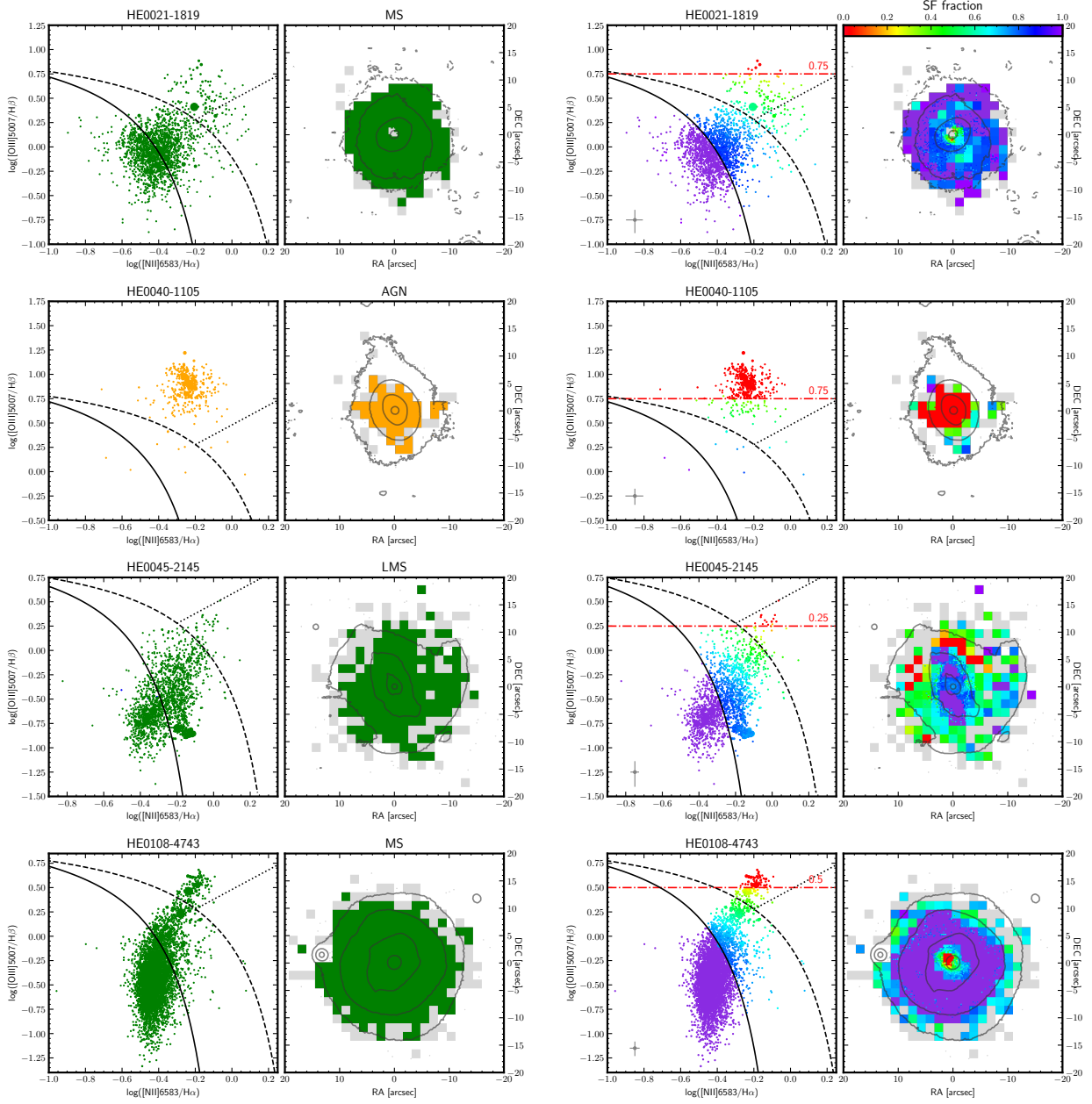


Figure A.4: BPT morphology and RAINBOW results for the sample. The BPT and a spatial map for each galaxy show SF fraction. The red dotted line shows the threshold for the AGN basis spaxels. The contours on the maps represent MUSE whitelight contours. The gray pixels on the maps represent those pixels, where $H\alpha$ SNR is more than 3σ , but the other lines are weaker so the datapoint cannot be shown on a BPT.

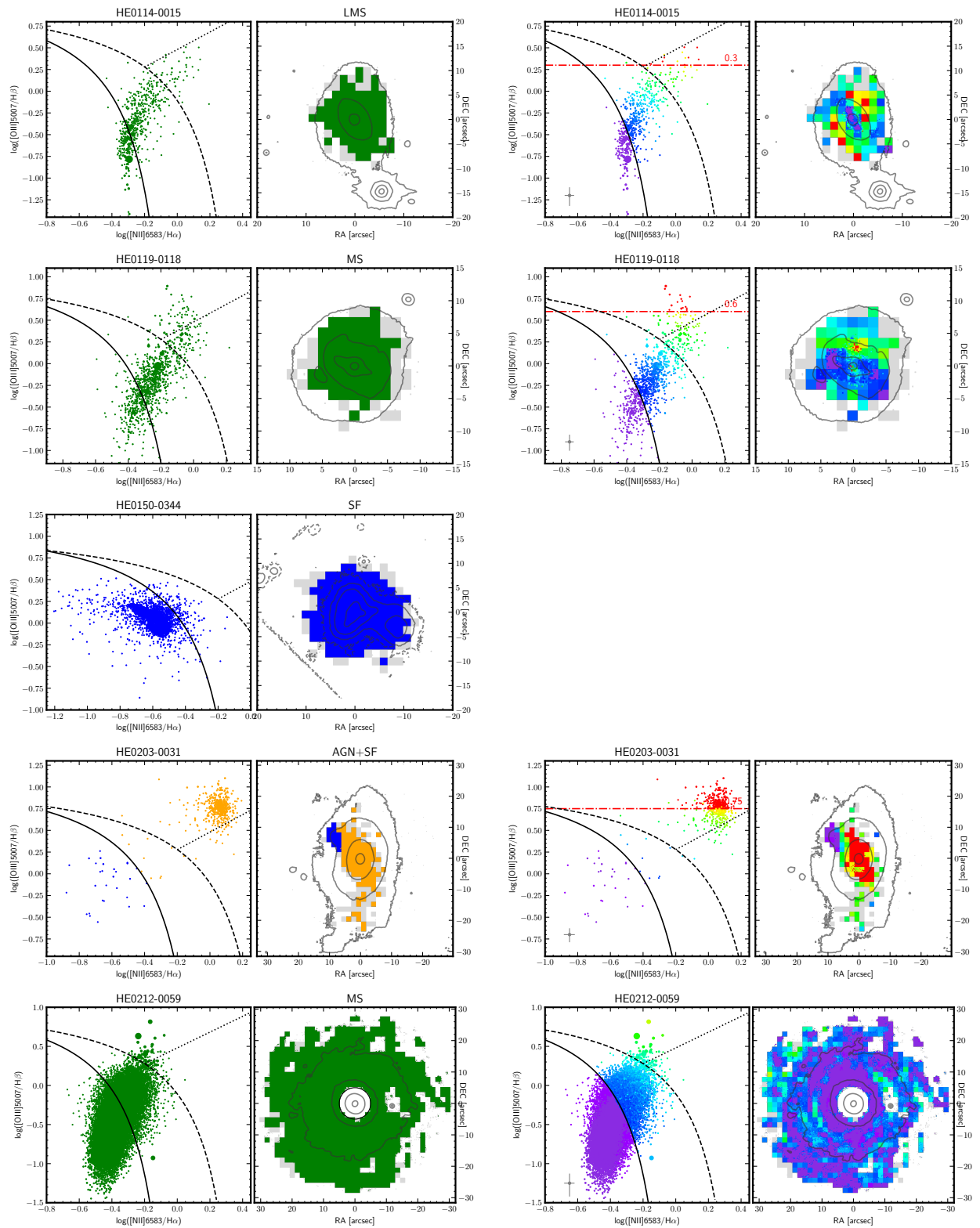


Figure A.4: continued.

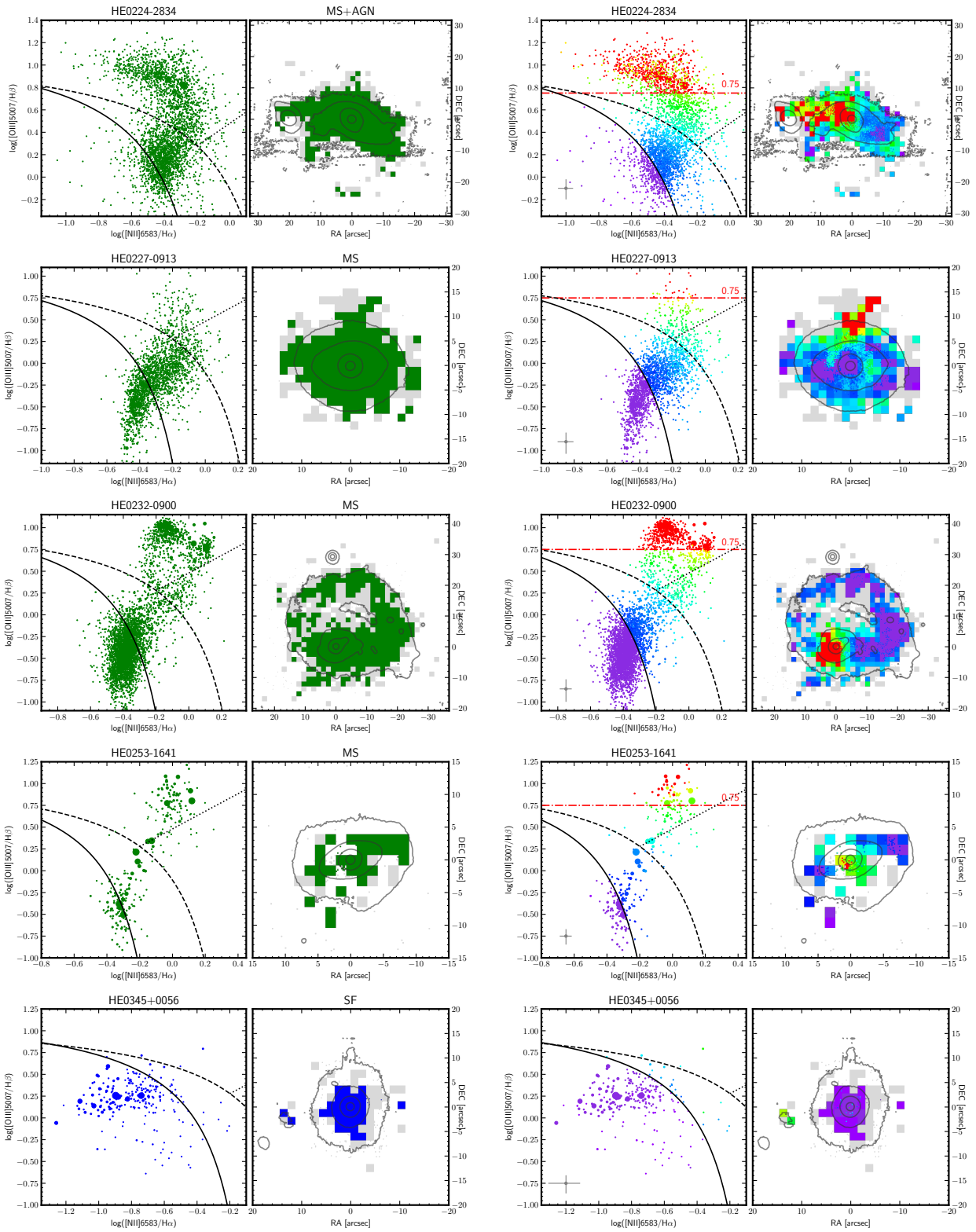


Figure A.4: continued.

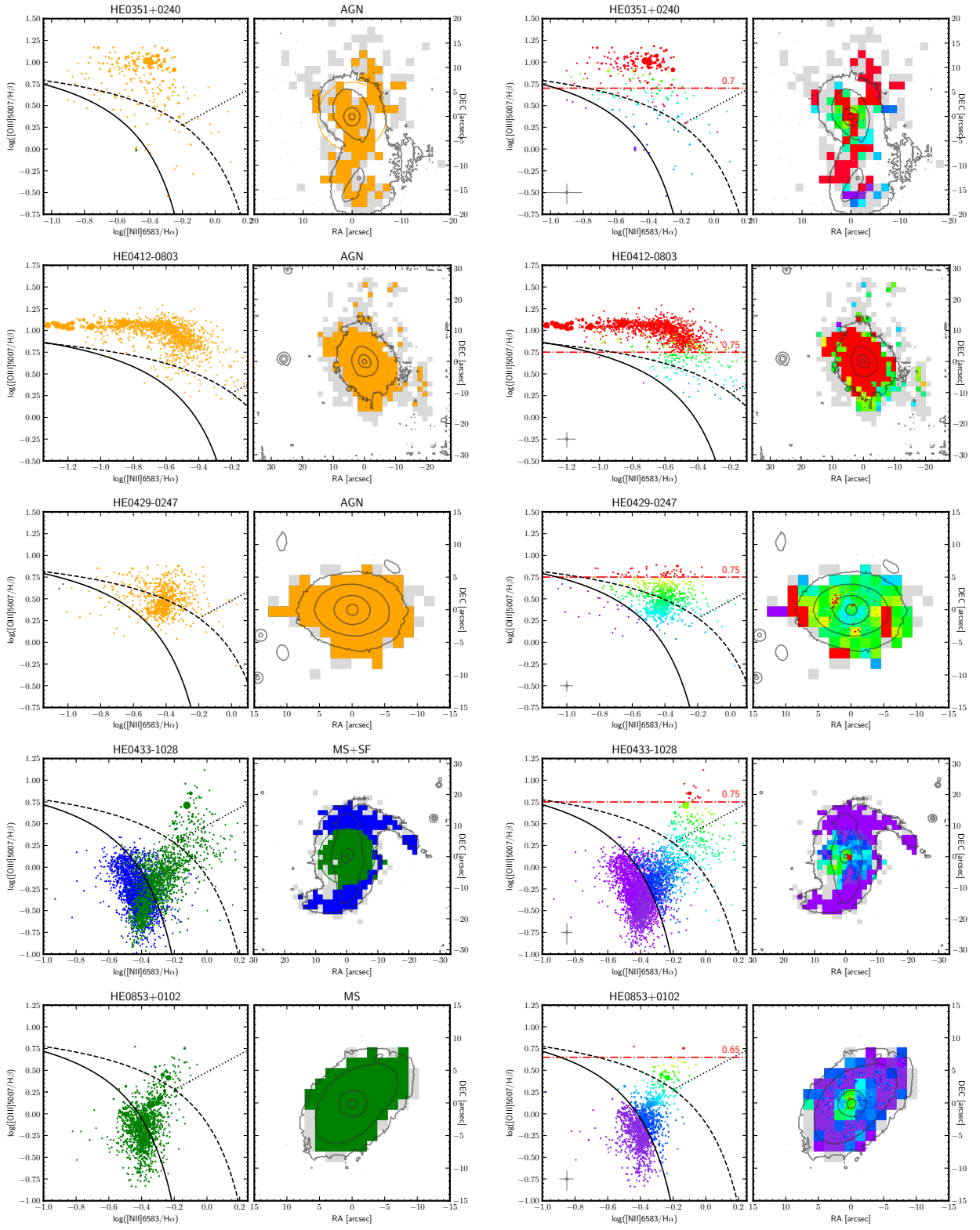


Figure A.4: continued.

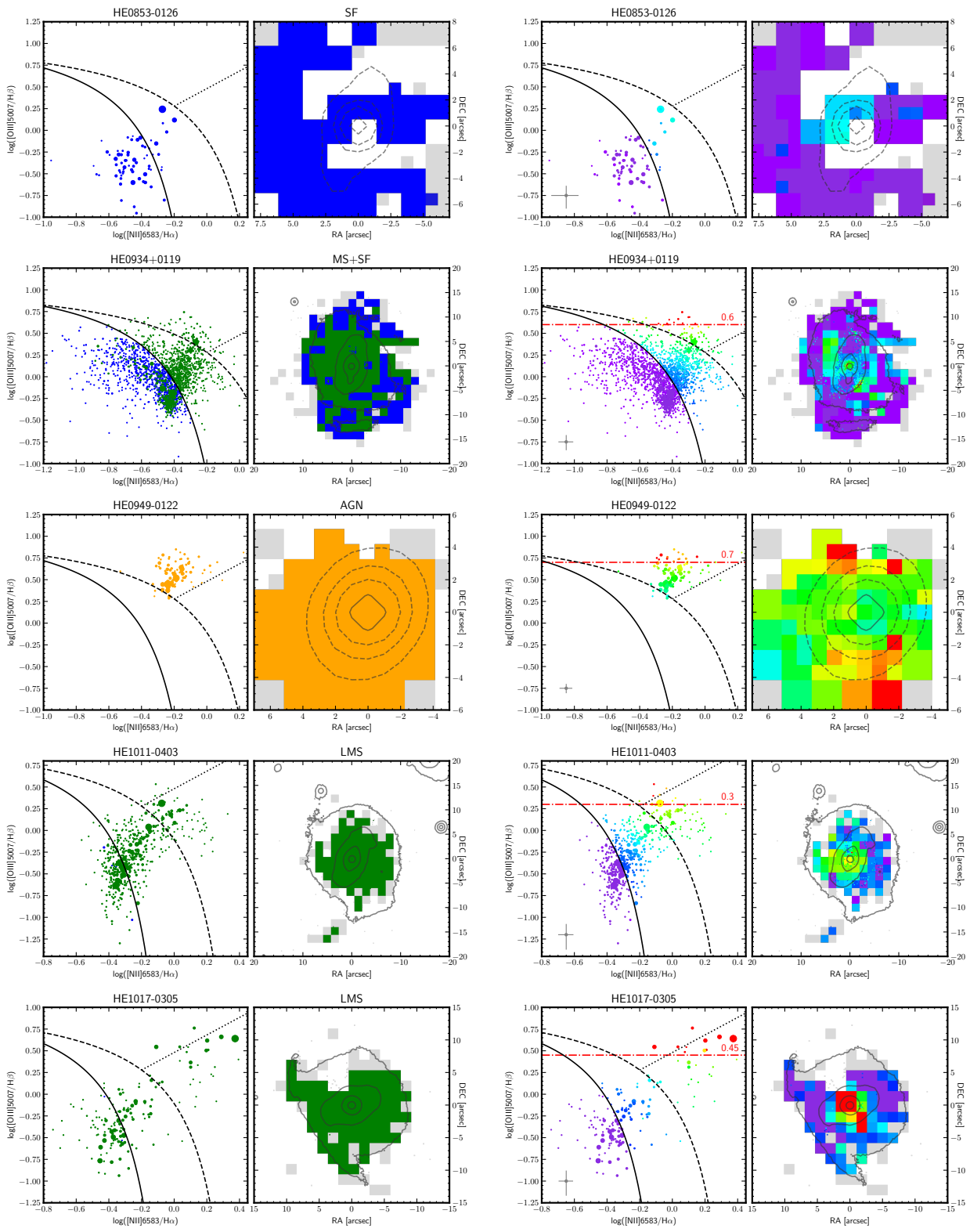


Figure A.4: continued.

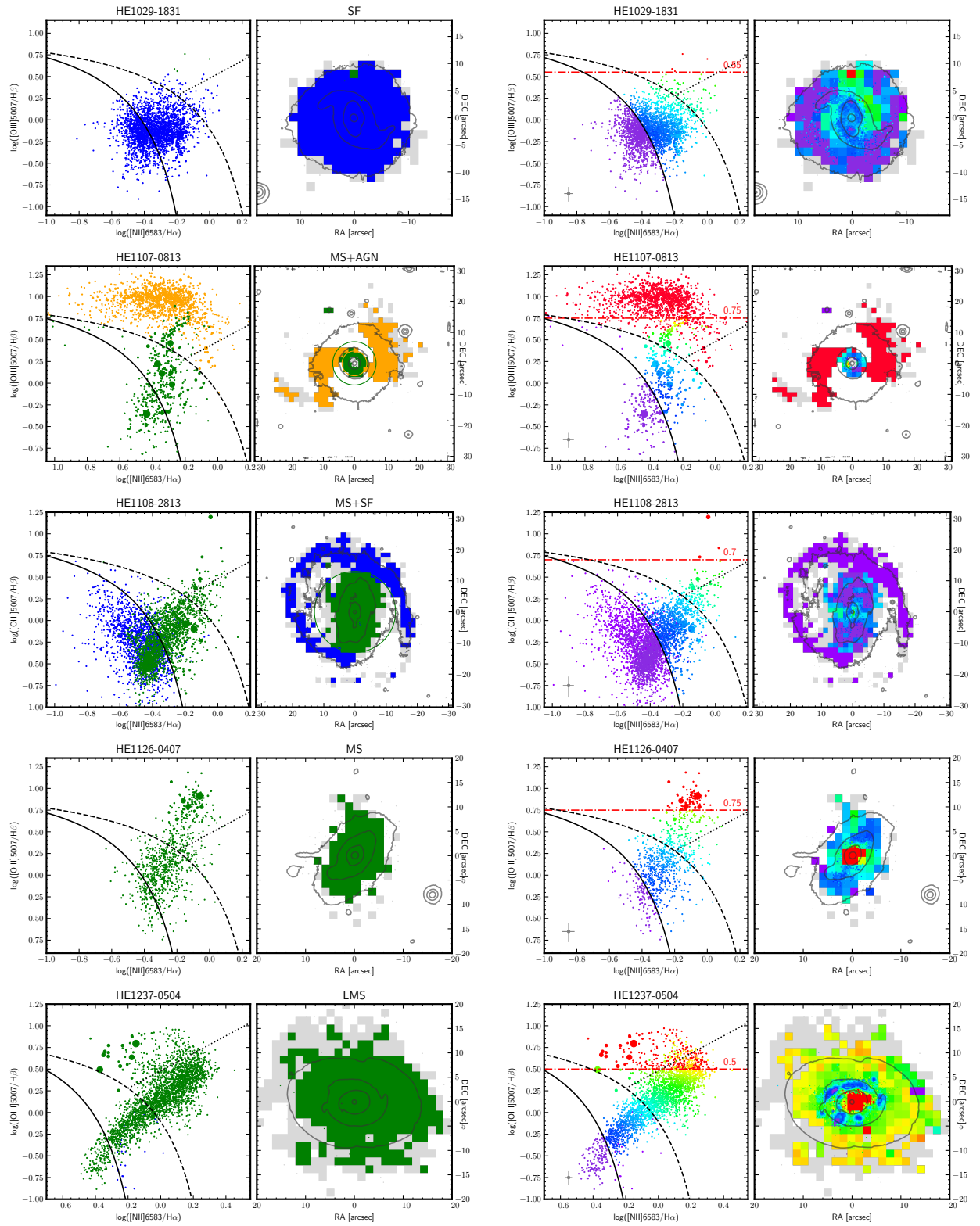


Figure A.4: continued.

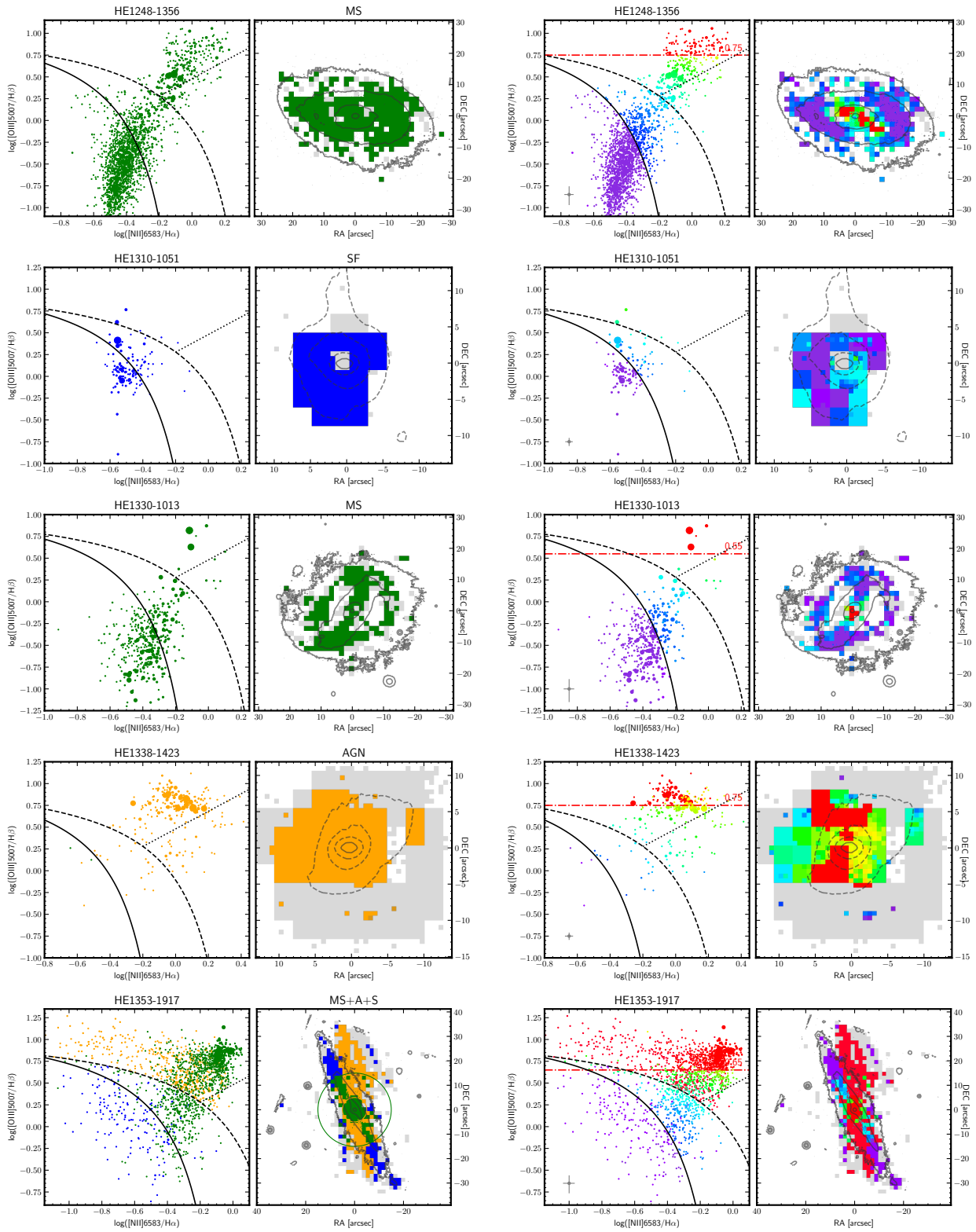


Figure A.4: continued.

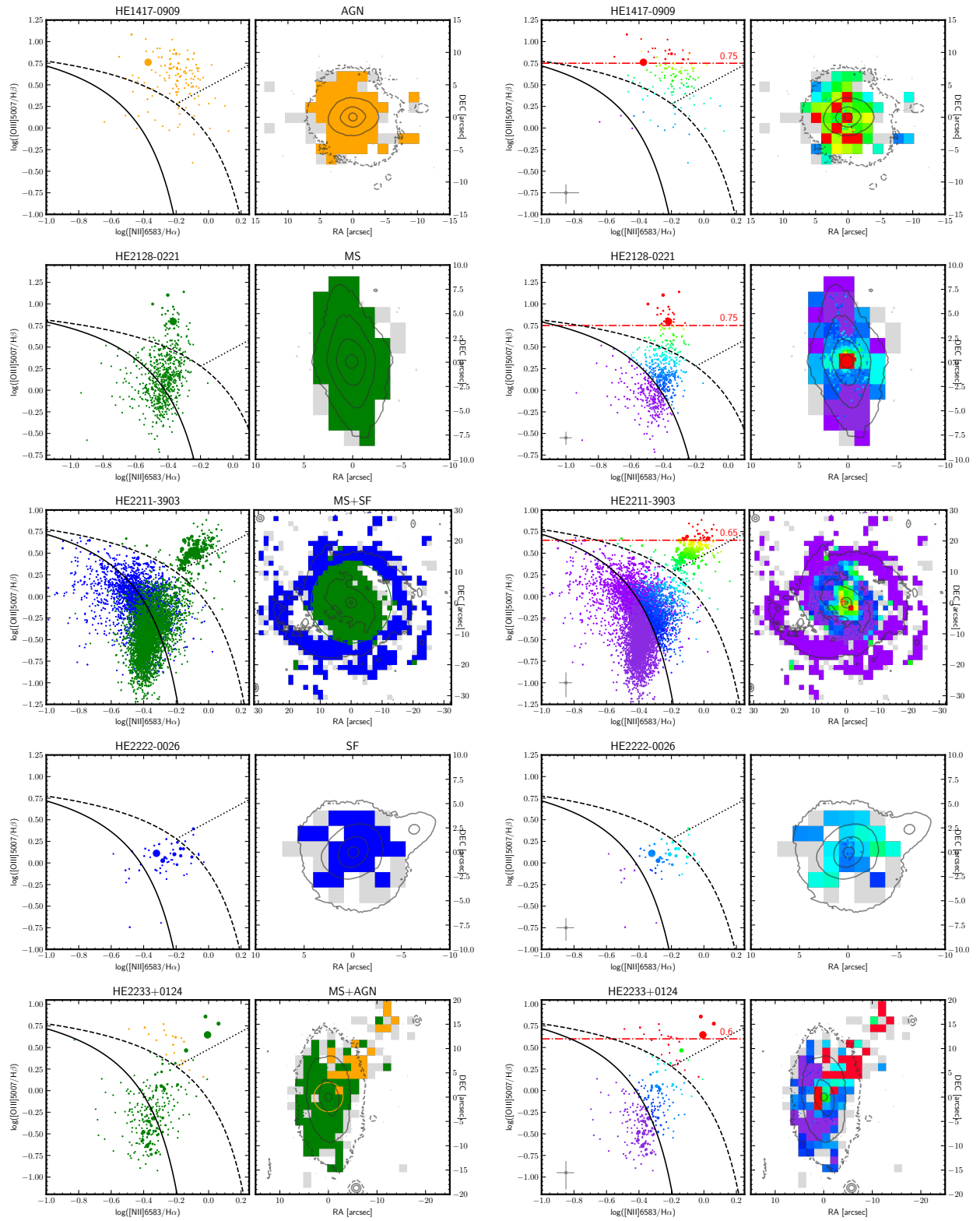


Figure A.4: continued.

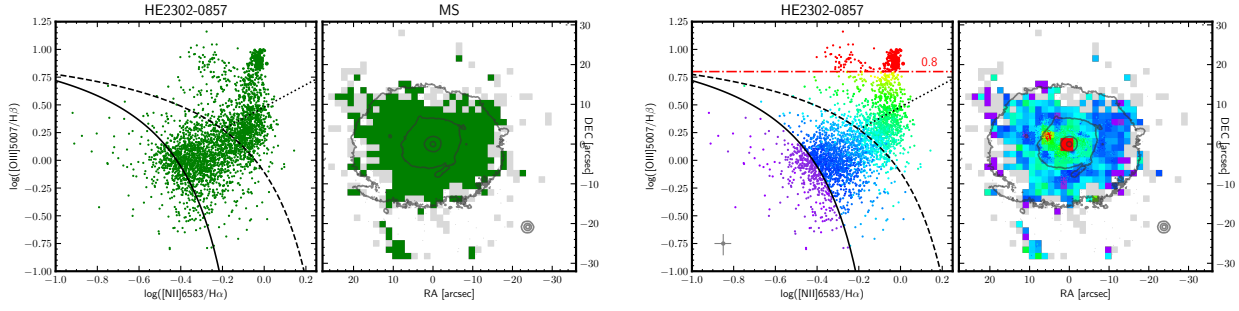


Figure A.4: continued.

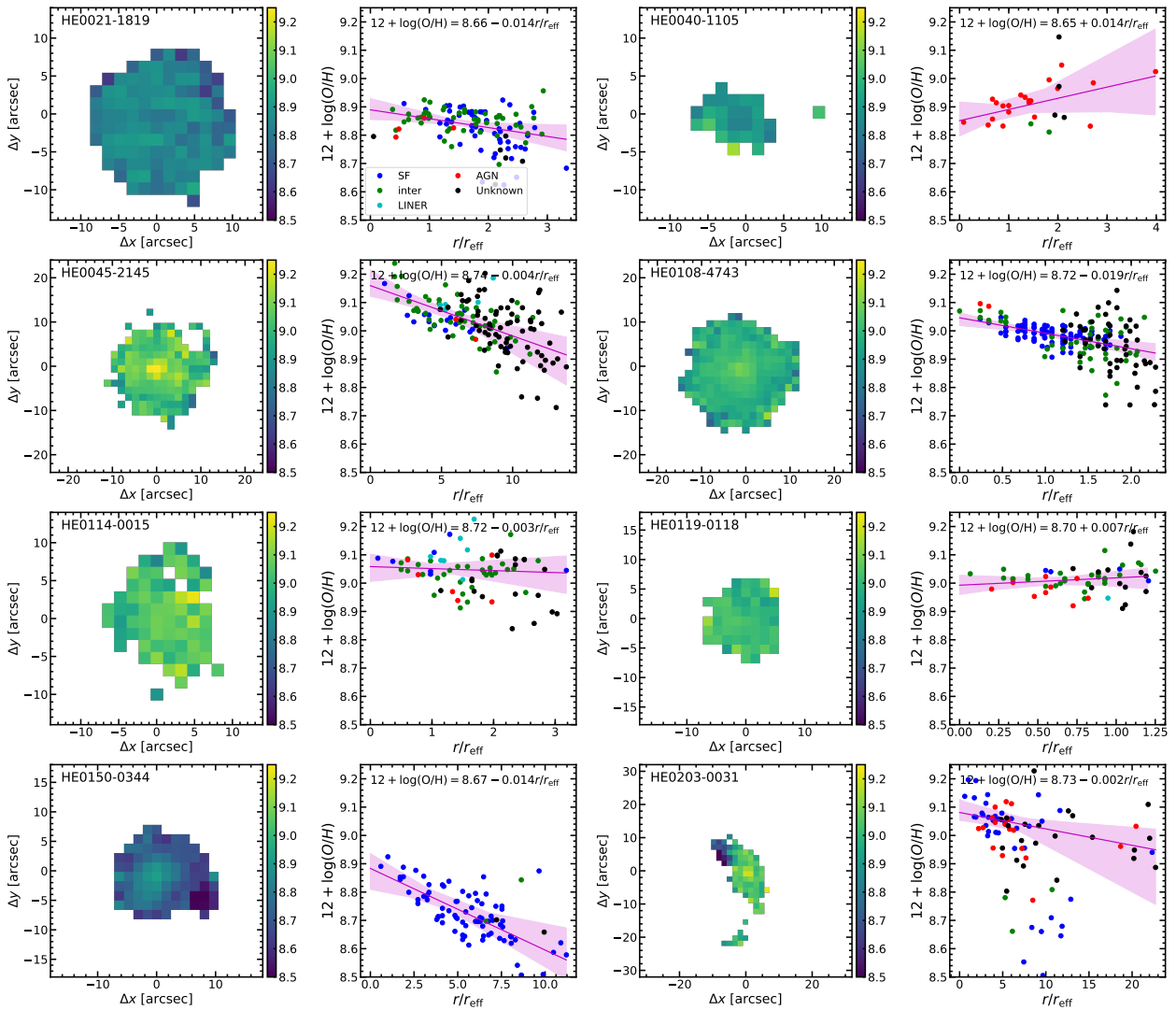


Figure A.5: Same as Fig. 2.5 for the entire sample.

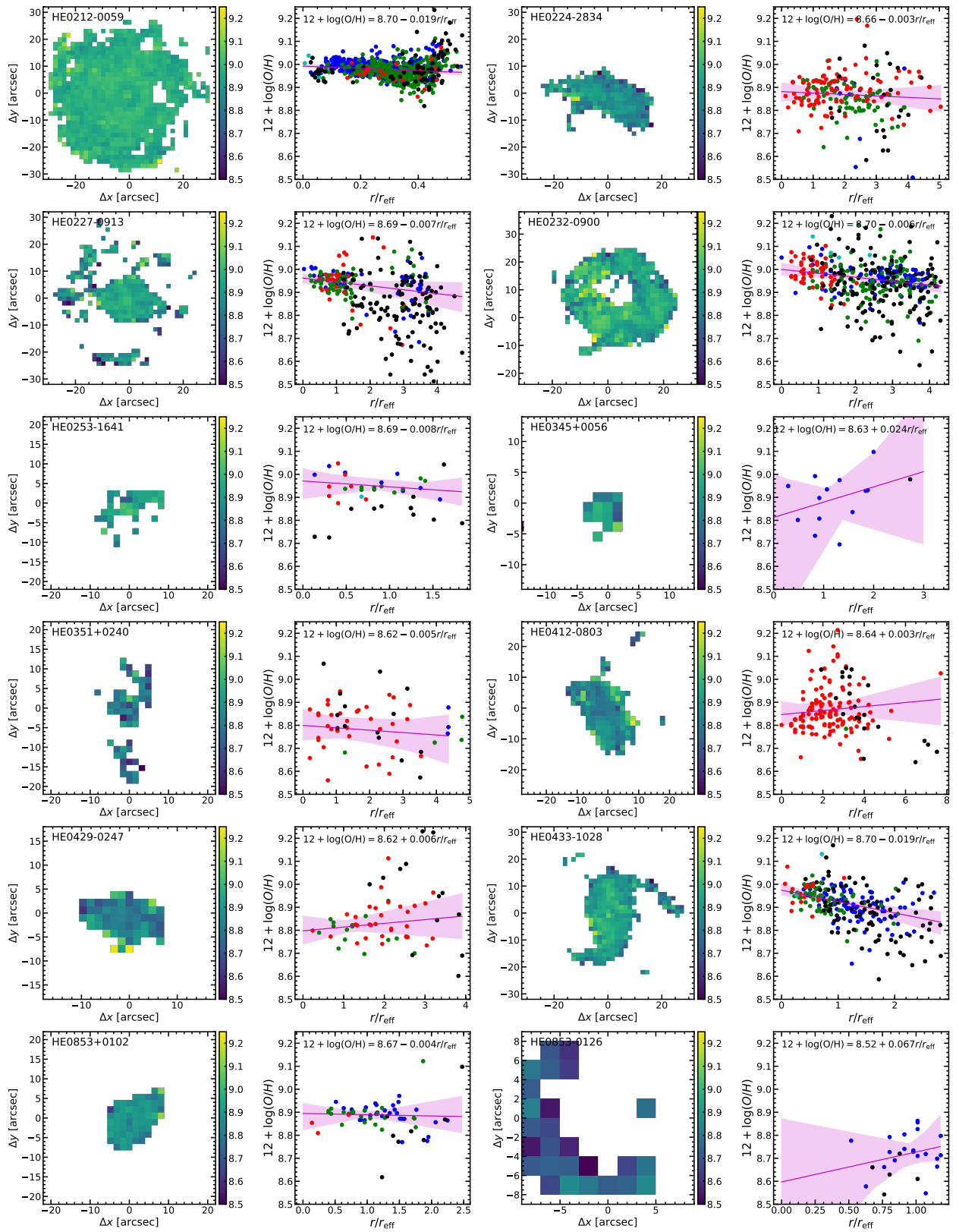


Figure A.5: continued.

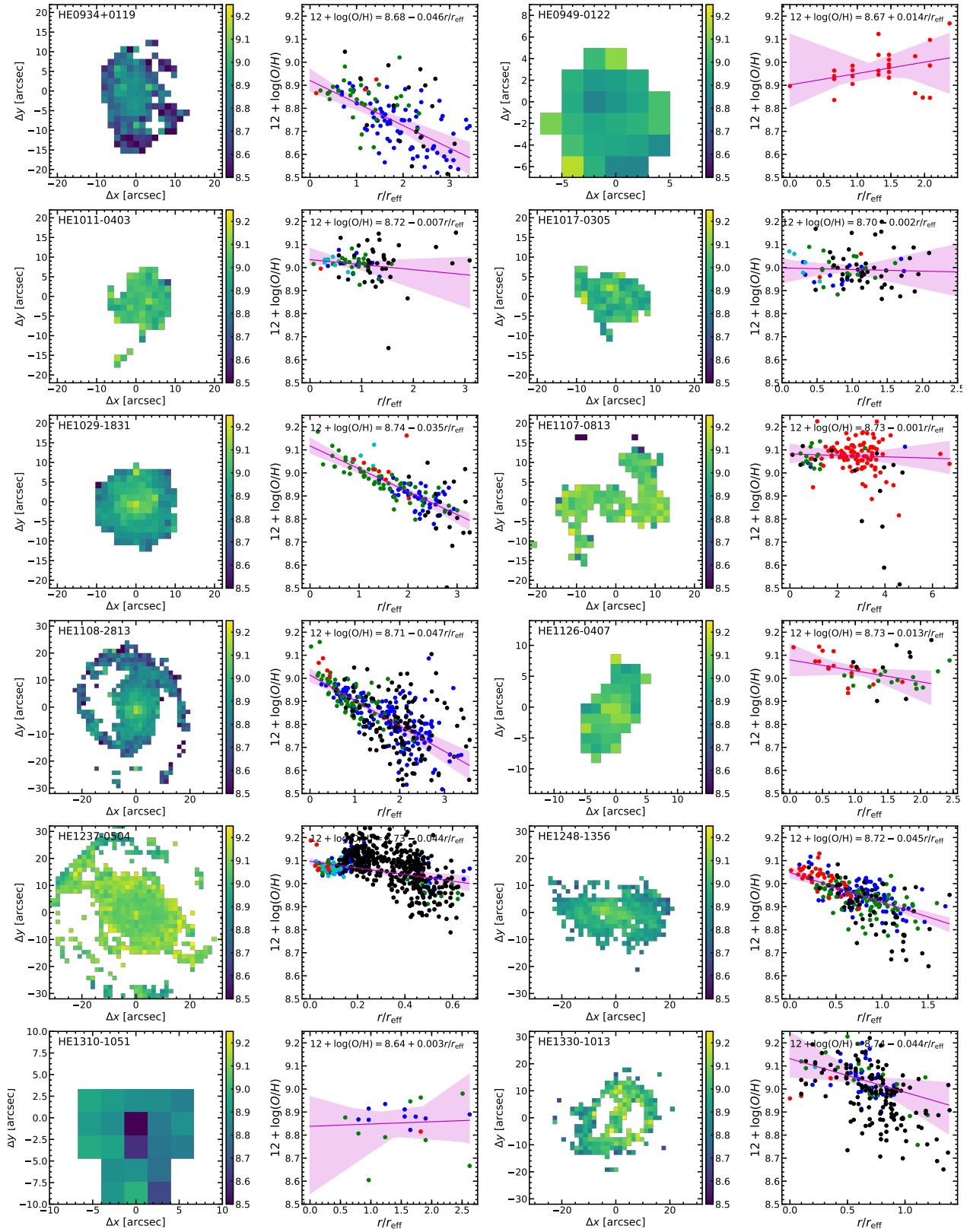


Figure A.5: continued.

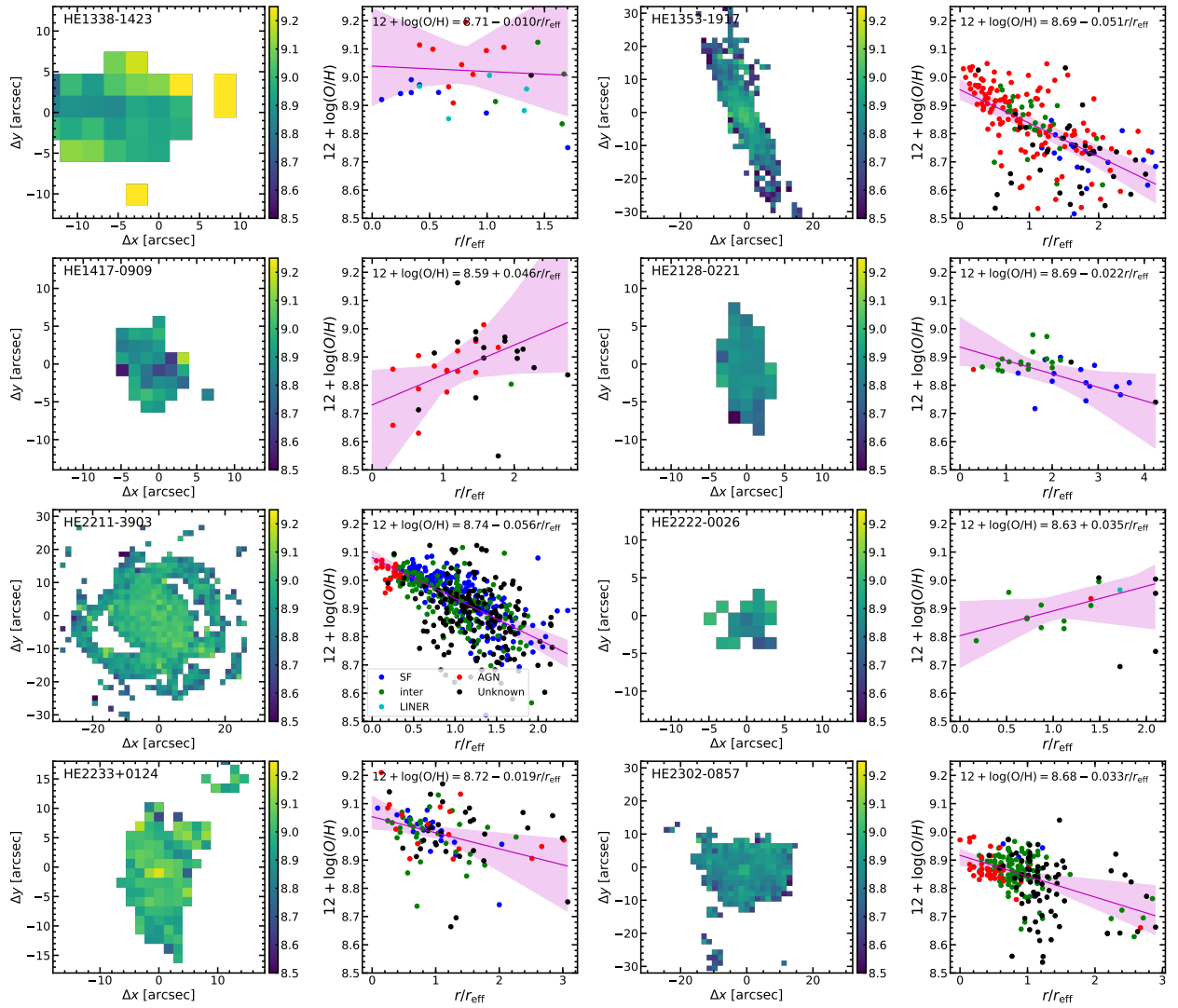


Figure A.5: continued.

A.2 FIFI-LS time window selection

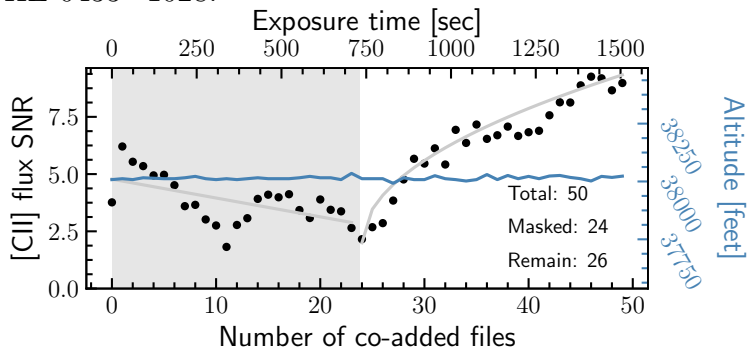
Although SOFIA reduces the water vapor absorption to 99% of the ground level, the atmospheric variations still play a perceptible role and affect the quality of the FIFI-LS data. To probe this effect, we used the science-ready LEVEL_3 pipeline output files. Each file corresponds to only ~ 30 seconds of exposure time and cannot be examined independently due to the high levels of noise. Calculating [C II] line flux signal-to-noise ratio (SNR) of cumulatively summed files allows us to trace the trends of the SNR and therefore judge the atmospheric conditions. Ideally, the trend should rise as the square root function. If the SNR remains the same or even decreases when exposure time is added, we assume that an atmospheric variation degrades the quality and exclude those time windows from the analysis, as shown with the shaded areas in Fig. A.6.

To calculate the SNR as a function of the exposure time, we fit a fixed Gaussian shape taken from the fitting result before the additional selection to the spectra, summed within the $36''$ diameter aperture. In the case of HE 1353–1917, when the line shape is not Gaussian, the procedure still works similarly because only relative trends are important in this analysis. Masking the spectral regions with strong atmospheric absorption lines is, conversely, very important for the flux estimations. The first few values of the SNR as a function of the coadded files are unreliable, but the overall trends remained when we performed the reverse-order coadding test.

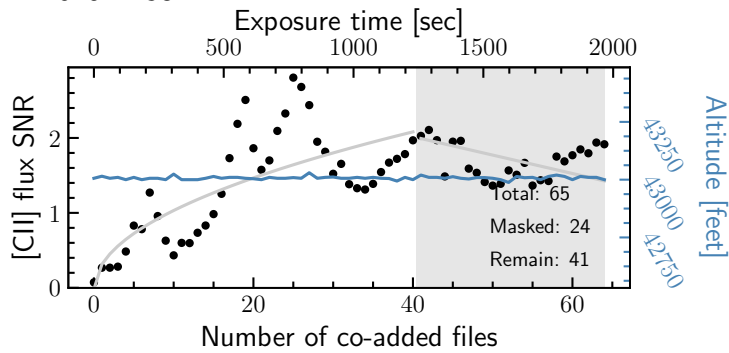
The rapid altitude shifts also affect the SNR trends as seen in the case of HE 1353–1917 and HE 2211–3903. In the last 15 files for HE 2211–3903 the altitude is higher and of much better quality, but we decided not to exclude the majority of the files from the analysis and kept all of them.

Even though the selection due to atmospheric conditions is performed in the reduction pipeline, our additional selection technique helps to increase SNR of the detection by excluding the poor quality artifact-rich files.

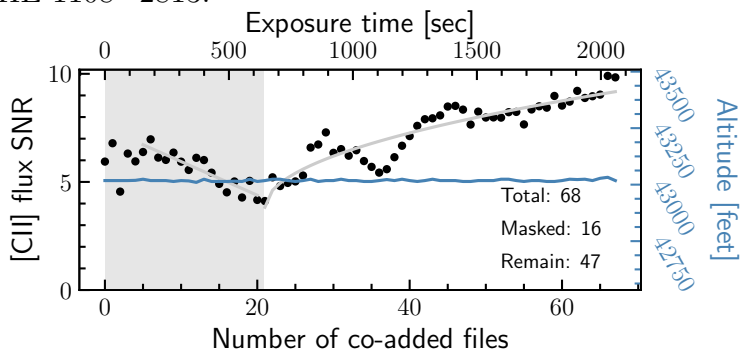
HE 0433–1028:



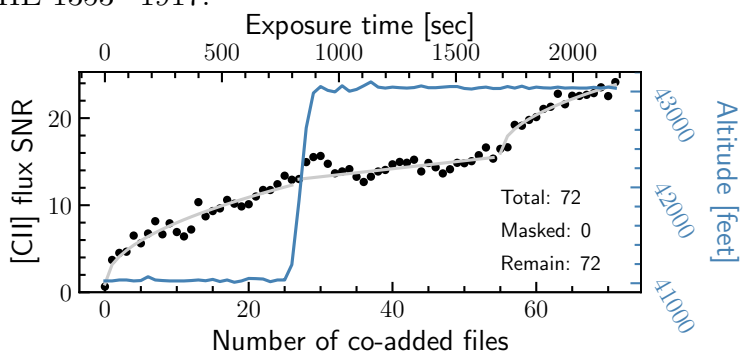
HE 1029–1831:



HE 1108–2813:



HE 1353–1917:



HE 2211–3903:

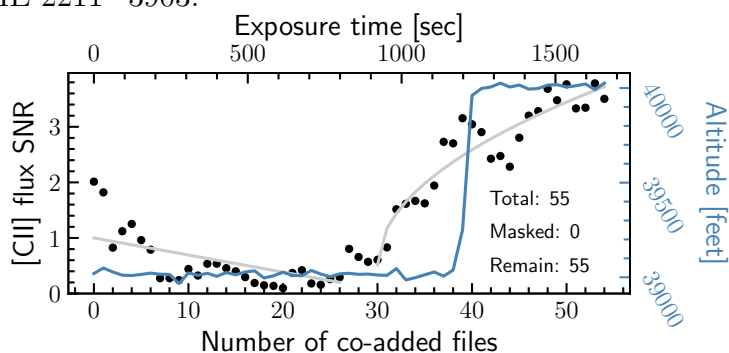


Figure A.6: [CII] line SNR as a function of the cumulatively coadded exposures (black circles). The trends (gray lines) are purely subjective and are shown to guide the eye. The shaded areas cover the time windows and associated files that were excluded from the further analysis. The corresponding altitudes of SOFIA are shown as blue lines.

Publications

The following published papers are involved in this thesis:

Leading author:

- **Smirnova-Pinchukova, I.**, Husemann, B., Davis, T. A., Smith, C. M. A., Singha, M., Tremblay, G. R., Klessen, R. S., Powell, M., Connor, T., Baum, S. A., Combes, F., Croom, S. M., Gaspari, M., Neumann, J., O’Dea, C. P., P evrez-Torres, M., Rosario, D. J., Rose, T., Scharw achter, J., Winkel, N.
"The Close AGN Reference Survey (CARS). No obvious signature of AGN feedback on star formation, but subtle trends"
Astronomy & Astrophysics, Volume 659, id.A125, 38 pp. (2022).
- **Smirnova-Pinchukova, I.**, Husemann, B., Busch, G., Appleton, P., Bethermin, M., Combes, F., Croom, S., Davis, T. A., Fischer, C., Gaspari, M., Groves, B., Klein, R., O’Dea, C. P., P evrez-Torres, M. A., Scharw achter, J., Singha, M., Tremblay, G. R., Urrutia, T.
"The Close AGN Reference Survey (CARS). Discovery of a global [C II] 158 μ m line excess in AGN HE 1353–1917"
Astronomy & Astrophysics, Volume 626, id.L3, 7 pp. (2019).

Contributing author:

- Husemann, B., Singha, M., Scharw achter, J., McElroy, R., Neumann, J., **Smirnova-Pinchukova, I.**, Urrutia, T., Baum, S. A., Bennert, V. N., Combes, F., Croom, S. M., Davis, T. A., Fournier, Y., Galkin, A., Gaspari, M., Enke, H., Krumpke, M., O’Dea, C. P., P evrez-Torres, M., Rose, T., Tremblay, G. R., Walcher, C. J.
"The Close AGN Reference Survey (CARS). IFU survey data and the BH mass dependence of long-term AGN variability"
Astronomy & Astrophysics, Volume 659, id.A124, 40 pp. (2022).
- Singha, M., Husemann, B., Urrutia, T., O’Dea, C. P., Scharw achter, J., Gaspari, M., Combes, F., Nevin, R., Terrazas, B. A., P evrez-Torres, M., Rose, T., Davis, T. A., Tremblay, G. R., Neumann, J., **Smirnova-Pinchukova, I.**, Baum, S. A.
"The Close AGN Reference Survey (CARS). Locating the [O III] wing component in

luminous local Type 1 AGN"

Astronomy & Astrophysics, Volume 659, id.A123, 47 pp. (2022).

- Puschnig, J., Hayes, M., Östlin, G., Cannon, J., **Smirnova-Pinchukova, I.**, Husemann, B., Kunth, D., Bridge, J., Herenz, E. C., Messa, M., Oteo, I.
"The Lyman Alpha Reference Sample. XI. Efficient turbulence-driven Ly α escape and an analysis of IR, CO, and [C II]158 μ m"
Astronomy & Astrophysics, Volume 644, id.A10, 29 pp. (2020).
- Husemann, B., Scharwächter, J., Davis, T. A., Pérez-Torres, M., **Smirnova-Pinchukova, I.**, Tremblay, G. R., Krumpe, M., Combes, F., Baum, S. A., Busch, G., Connor, T., Croom, S. M., Gaspari, M., Kraft, R. P., O'Dea, C. P., Powell, M., Singha, M., Urrutia, T.
"The Close AGN Reference Survey (CARS). A massive multi-phase outflow impacting the edge-on galaxy HE 1353–1917"
Astronomy & Astrophysics, Volume 627, id.A53, 28 pp. (2019).
- Neumann, J., Gadotti, D. A., Wisotzki, L., Husemann, B., Busch, G., Combes, F., Croom, S. M., Davis, T. A., Gaspari, M., Krumpe, M., Pérez-Torres, M. A., Scharwächter, J., **Smirnova-Pinchukova, I.**, Tremblay, G. R., Urrutia, T.
"The Close AGN Reference Survey (CARS). Comparative analysis of the structural properties of star-forming and non-star-forming galaxy bars"
Astronomy & Astrophysics, Volume 627, id.A26, 26 pp. (2019).
- Busch, G., Husemann, B., **Smirnova-Pinchukova, I.**, Eckart, A., Baum, S. A., Combes, F., Croom, S. M., Davis, T. A., Fazeli, N., Fischer, C., Gaspari, M., Klein, R., Krumpe, M., McElroy, R., O'Dea, C. P., Pérez-Torres, M. A., Powell, M. C., Sánchez-Monge, Á., Scharwächter, J., Tremblay, G. R., Urrutia, T.
"The Close AGN Reference Survey (CARS): SOFIA Detects Spatially Resolved [C II] Emission in the Luminous AGN HE 0433–1028"
The Astrophysical Journal Letters, Volume 866, Issue 1, article id. L9, 6 pp. (2018).

Bibliography

- Abazajian, K. N., Adelman-McCarthy, J. K., Agüeros, M. A., et al. 2009, *ApJS*, 182, 543
- Abbott, B. P., Abbott, R., Abbott, T. D., et al. 2016, *Phys.Rev.Lett*, 116, 061102
- Abraham, R. G., & van den Bergh, S. 2001, *Science*, 293, 1273
- Aird, J., Coil, A. L., Moustakas, J., et al. 2012, *ApJ*, 746, 90
- Alam, S., Albareti, F. D., Allende Prieto, C., et al. 2015, *ApJS*, 219, 12
- Alexander, D. M., & Hickox, R. C. 2012, , 56, 93
- Alonso-Herrero, A., Pereira-Santaella, M., García-Burillo, S., et al. 2018, *ApJ*, 859, 144
- Antonucci, R. 1993, *ARA&A*, 31, 473
- Appleton, P. N., Guillard, P., Boulanger, F., et al. 2013, *ApJ*, 777, 66
- Appleton, P. N., Diaz-Santos, T., Fadda, D., et al. 2018, *ApJ*, 869, 61
- Baade, D., Meisenheimer, K., Iwert, O., et al. 1999, *The Messenger*, 95, 15
- Bacon, R., Accardo, M., Adjali, L., et al. 2010, in , Vol. 7735, *Ground-based and Airborne Instrumentation for Astronomy III*, 773508
- Baldry, I. K., Glazebrook, K., Brinkmann, J., et al. 2004, *ApJ*, 600, 681
- Baldwin, J. A., Phillips, M. M., & Terlevich, R. 1981, *PASP*, 93, 5
- Balmaverde, B., Marconi, A., Brusa, M., et al. 2016, *A&A*, 585, A148
- Barnes, J. E. 2004, *MNRAS*, 350, 798
- Barth, A. J., Sarzi, M., Rix, H.-W., et al. 2001, *ApJ*, 555, 685
- Beckmann, V., & Shradler, C. R. 2012, *Active Galactic Nuclei*
- Bell, E. F., Wolf, C., Meisenheimer, K., et al. 2004, *ApJ*, 608, 752
- Benson, A. J., Bower, R. G., Frenk, C. S., et al. 2003, *ApJ*, 599, 38
- Bernhard, E., Mullaney, J. R., Daddi, E., Ciesla, L., & Schreiber, C. 2016, *MNRAS*, 460, 902

- Bertram, T., Eckart, A., Fischer, S., et al. 2007, *A&A*, 470, 571
- Bianchi, L., Shiao, B., & Thilker, D. 2017, *ApJS*, 230, 24
- Bing, L., Shi, Y., Chen, Y., et al. 2019, *MNRAS*, 482, 194
- Bischetti, M., Piconcelli, E., Vietri, G., et al. 2017, *A&A*, 598, A122
- Bischetti, M., Feruglio, C., Piconcelli, E., et al. 2021, *A&A*, 645, A33
- Bluck, A. F. L., Maiolino, R., Sánchez, S. F., et al. 2020, *MNRAS*, 492, 96
- Bolatto, A. D., Wolfire, M., & Leroy, A. K. 2013, *ARA&A*, 51, 207
- Bongiorno, A., Merloni, A., Brusa, M., et al. 2012, *MNRAS*, 427, 3103
- Bordoloi, R., Lilly, S. J., Knobel, C., et al. 2011, *ApJ*, 743, 10
- Boselli, A., Fossati, M., Gavazzi, G., et al. 2015, *A&A*, 579, A102
- Boselli, A., Gavazzi, G., Lequeux, J., & Pierini, D. 2002, *A&A*, 385, 454
- Bouché, N., Hohensee, W., Vargas, R., et al. 2012, *MNRAS*, 426, 801
- Bower, R. G., Benson, A. J., Malbon, R., et al. 2006, *MNRAS*, 370, 645
- Bradley, L., Sipócz, B., Robitaille, T., et al. 2020, *astropy/photutils*: 1.0.0, doi:10.5281/zenodo.4044744
- Brammer, G. B., Whitaker, K. E., van Dokkum, P. G., et al. 2009, *ApJL*, 706, L173
- Brinchmann, J., Charlot, S., Heckman, T. M., et al. 2004, arXiv e-prints, astro
- Brisbin, D., Ferkinhoff, C., Nikola, T., et al. 2015, *ApJ*, 799, 13
- Brownson, S., Belfiore, F., Maiolino, R., Lin, L., & Carniani, S. 2020, *MNRAS*, 498, L66
- Brüggen, M., & Kaiser, C. R. 2002, *Nature*, 418, 301
- Bruzual, G., & Charlot, S. 2003, *MNRAS*, 344, 1000
- Bundy, K., Bershady, M. A., Law, D. R., et al. 2015, *ApJ*, 798, 7
- Busch, G., Zuther, J., Valencia-S., M., et al. 2014, *A&A*, 561, A140
- Busch, G., Smajić, S., Scharwächter, J., et al. 2015, *A&A*, 575, A128
- Busch, G., Husemann, B., Smirnova-Pinchukova, I., et al. 2018, *ApJL*, 866, L9
- Calistro Rivera, G., Lusso, E., Hennawi, J. F., & Hogg, D. W. 2016, *ApJ*, 833, 98
- Calzetti, D., Kennicutt, R. C., Engelbracht, C. W., et al. 2007, *ApJ*, 666, 870
- Cárdenas Vázquez, M. C., Dorner, B., Huber, A., et al. 2018, *PASP*, 130, 025003
- Carleton, T., Cooper, M. C., Bolatto, A. D., et al. 2017, *MNRAS*, 467, 4886

Carniani, S., Marconi, A., Maiolino, R., et al. 2017, *A&A*, 605, A105

Catalán-Torrecilla, C., Gil de Paz, A., Castillo-Morales, A., et al. 2017, *ApJ*, 848, 87

Cecil, G., Bland-Hawthorn, J., Veilleux, S., & Filippenko, A. V. 2001, *ApJ*, 555, 338

Chambers, K. C., Magnier, E. A., Metcalfe, N., et al. 2016, arXiv:1612.05560

Chapin, E. L., Berry, D. S., Gibb, A. G., et al. 2013, *MNRAS*, 430, 2545

Chary, R., & Elbaz, D. 2001, *ApJ*, 556, 562

Chen, Z., Faber, S. M., Koo, D. C., et al. 2020, *ApJ*, 897, 102

Cicone, C., Maiolino, R., Sturm, E., et al. 2014, *A&A*, 562, A21

Circosta, C., Mainieri, V., Padovani, P., et al. 2018, *A&A*, 620, A82

Circosta, C., Mainieri, V., Lamperti, I., et al. 2021, *A&A*, 646, A96

Colombo, D., Sanchez, S. F., Bolatto, A. D., et al. 2020, *A&A*, 644, A97

Condon, J. J. 1992, *ARA&A*, 30, 575

Condon, J. J., Cotton, W. D., Greisen, E. W., et al. 1998, *AJ*, 115, 1693

Cresci, G., Mainieri, V., Brusa, M., et al. 2015a, *ApJ*, 799, 82

Cresci, G., Marconi, A., Zibetti, S., et al. 2015b, *A&A*, 582, A63

Croom, S. M., Owers, M. S., Scott, N., et al. 2021, *MNRAS*, 505, 991

Croton, D. J., Springel, V., White, S. D. M., et al. 2006, *MNRAS*, 365, 11

Croxall, K. V., Smith, J. D., Pellegrini, E., et al. 2017, *ApJ*, 845, 96

Curti, M., Mannucci, F., Cresci, G., & Maiolino, R. 2020, *MNRAS*, 491, 944

Cutri, R. M., Wright, E. L., Conrow, T., et al. 2011, Explanatory Supplement to the WISE Preliminary Data Release Products, Tech. rep.

da Cunha, E., Charlot, S., & Elbaz, D. 2008, *MNRAS*, 388, 1595

Dale, D. A., & Helou, G. 2002, *ApJ*, 576, 159

Davies, L. J. M., Robotham, A. S. G., Driver, S. P., et al. 2015, *MNRAS*, 452, 616

Davies, R. L., Kewley, L. J., Ho, I. T., & Dopita, M. A. 2014a, *MNRAS*, 444, 3961

Davies, R. L., Rich, J. A., Kewley, L. J., & Dopita, M. A. 2014b, *MNRAS*, 439, 3835

Davies, R. L., Groves, B., Kewley, L. J., et al. 2016, *MNRAS*, 462, 1616

—. 2017, *MNRAS*, 470, 4974

Decarli, R., Walter, F., Venemans, B. P., et al. 2018, *ApJ*, 854, 97

- Dempsey, J. T., Friberg, P., Jenness, T., et al. 2013, *MNRAS*, 430, 2534
- Denney, K. D., De Rosa, G., Croxall, K., et al. 2014, *ApJ*, 796, 134
- DePoy, D. L., Abbott, T., Annis, J., et al. 2008, in *Society of Photo-Optical Instrumentation Engineers (SPIE) Conference Series*, Vol. 7014, *Ground-based and Airborne Instrumentation for Astronomy II*, 70140E
- Di Matteo, P., Bournaud, F., Martig, M., et al. 2008, *A&A*, 492, 31
- Di Matteo, T., Springel, V., & Hernquist, L. 2005, *Nature*, 433, 604
- Díaz-Santos, T., Armus, L., Charmandaris, V., et al. 2013, *ApJ*, 774, 68
- Dopita, M. A., Kewley, L. J., Sutherland, R. S., & Nicholls, D. C. 2016, *Ap&SS*, 361, 61
- Draper, N. R. 1998, *Applied regression analysis*
- Edge, D. O., Shakeshaft, J. R., McAdam, W. B., Baldwin, J. E., & Archer, S. 1959, *MmRAS*, 68, 37
- Elbaz, D., Dickinson, M., Hwang, H. S., et al. 2011, *A&A*, 533, A119
- Ellison, S. L., Patton, D. R., Simard, L., & McConnachie, A. W. 2008, *AJ*, 135, 1877
- Ellison, S. L., Thorp, M. D., Lin, L., et al. 2020, *MNRAS*, 493, L39
- Fabian, A. C. 2012, *ARA&A*, 50, 455
- Fabian, A. C., Sanders, J. S., Taylor, G. B., et al. 2006, *MNRAS*, 366, 417
- Fanaroff, B. L., & Riley, J. M. 1974, *MNRAS*, 167, 31P
- Farrah, D., Urrutia, T., Lacy, M., et al. 2012, *ApJ*, 745, 178
- Fernández-Ontiveros, J. A., Tristram, K. R. W., Hönig, S., Gandhi, P., & Weigelt, G. 2018, *A&A*, 611, A46
- Ferrarese, L., & Merritt, D. 2000, *ApJL*, 539, L9
- Feruglio, C., Maiolino, R., Piconcelli, E., et al. 2010, *A&A*, 518, L155
- Fitzpatrick, E. L. 1999, *PASP*, 111, 63
- Flores Velázquez, J. A., Gurvich, A. B., Faucher-Giguère, C.-A., et al. 2021, *MNRAS*, 501, 4812
- Foreman-Mackey, D., Hogg, D. W., Lang, D., & Goodman, J. 2013, *PASP*, 125, 306
- Fraser-McKelvie, A., Merrifield, M., Aragón-Salamanca, A., et al. 2020, *MNRAS*, 499, 1116
- Friedmann, A. 1922, *Zeitschrift fur Physik*, 10, 377
- Fruchter, A., & Hook, R. N. 1997, in , Vol. 3164, *Applications of Digital Image Processing XX*, ed. A. G. Tescher, 120–125

Gallimore, J. F., Elitzur, M., Maiolino, R., et al. 2016, *ApJL*, 829, L7

García-Burillo, S., Combes, F., Usero, A., et al. 2014, *A&A*, 567, A125

Gaspari, M., Brighenti, F., & Temi, P. 2015, *A&A*, 579, A62

Gaspari, M., Tombesi, F., & Cappi, M. 2020, *Nature Astronomy*, 4, 10

Gaspari, M., Eckert, D., Etti, S., et al. 2019, *ApJ*, 884, 169

Gendron-Marsolais, M. L., Hull, C. L. H., Perley, R., et al. 2021, *ApJ*, 911, 56

Genzel, R., Tacconi, L. J., Combes, F., et al. 2012, *ApJ*, 746, 69

Giustini, M., Cappi, M., Chartas, G., et al. 2011, *A&A*, 536, A49

Greene, J. E., & Ho, L. C. 2005a, *ApJ*, 627, 721

—. 2005b, *ApJ*, 630, 122

Groves, B. A., Heckman, T. M., & Kauffmann, G. 2006, *MNRAS*, 371, 1559

Guillard, P., Boulanger, F., Lehnert, M. D., et al. 2015, *A&A*, 574, A32

Gullberg, B., De Breuck, C., Vieira, J. D., et al. 2015, *MNRAS*, 449, 2883

Harper, D. A., Runyan, M. C., Dowell, C. D., et al. 2018, *Journal of Astronomical Instrumentation*, 7, 1840008

Harrison, C. M., Alexander, D. M., Mullaney, J. R., et al. 2012, *ApJL*, 760, L15

—. 2016, *MNRAS*, 456, 1195

Hart, R. E., Bamford, S. P., Willett, K. W., et al. 2016, *MNRAS*, 461, 3663

Hayward, C. C., Lanz, L., Ashby, M. L. N., et al. 2014, *MNRAS*, 445, 1598

Heesen, V., Brinks, E., Leroy, A. K., et al. 2014, *AJ*, 147, 103

Helou, G., Malhotra, S., Hollenbach, D. J., Dale, D. A., & Contursi, A. 2001, *ApJL*, 548, L73

Henden, A. A., Welch, D. L., Terrell, D., & Levine, S. E. 2009, in *American Astronomical Society Meeting Abstracts*, Vol. 214, *American Astronomical Society Meeting Abstracts #214*, 407.02

Herrera-Camus, R., Bolatto, A. D., Wolfire, M. G., et al. 2015, *ApJ*, 800, 1

Herrera-Camus, R., Sturm, E., Graciá-Carpio, J., et al. 2018a, *ApJ*, 861, 94

—. 2018b, *ApJ*, 861, 95

Hickox, R. C., Mullaney, J. R., Alexander, D. M., et al. 2014, *ApJ*, 782, 9

Hirashita, H., Buat, V., & Inoue, A. K. 2003, *A&A*, 410, 83

Ho, L. C. 2005, *ApJ*, 629, 680

- Holland, W. S., Bintley, D., Chapin, E. L., et al. 2013, *MNRAS*, 430, 2513
- Hopkins, P. F., Cox, T. J., Hernquist, L., et al. 2013, *MNRAS*, 430, 1901
- Hopkins, P. F., & Elvis, M. 2010, *MNRAS*, 401, 7
- Hopkins, P. F., Hernquist, L., Cox, T. J., & Kereš, D. 2008, *ApJS*, 175, 356
- Hubble, E. P. 1926, *ApJ*, 64, 321
- . 1936, *Realm of the Nebulae*
- Husemann, B., Bennert, V. N., Scharwächter, J., Woo, J.-H., & Choudhury, O. S. 2016a, *MNRAS*, 455, 1905
- Husemann, B., & Harrison, C. M. 2018, *Nature Astronomy*, 2, 196
- Husemann, B., Jahnke, K., Sánchez, S. F., et al. 2014, *MNRAS*, 443, 755
- Husemann, B., Wisotzki, L., Sánchez, S. F., & Jahnke, K. 2013, *A&A*, 549, A43
- Husemann, B., Urrutia, T., Tremblay, G. R., et al. 2016b, *A&A*, 593, L9
- Husemann, B., Scharwächter, J., Davis, T. A., et al. 2019, *A&A*, 627, A53
- Husemann, B., Singha, M., Scharwächter, J., et al. 2022, *A&A*, 659, A124
- Jahnke, K., & Macciò, A. V. 2011, *ApJ*, 734, 92
- Jarrett, T. H., Chester, T., Cutri, R., et al. 2000, *AJ*, 119, 2498
- Kakkad, D., Mainieri, V., Brusa, M., et al. 2017, *MNRAS*, 468, 4205
- Kauffmann, G., Heckman, T. M., Tremonti, C., et al. 2003, *MNRAS*, 346, 1055
- Kennicutt, R. C., J., & Kent, S. M. 1983, *AJ*, 88, 1094
- Kennicutt, Robert C., J. 1989, *ApJ*, 344, 685
- . 1998, *ApJ*, 498, 541
- Kewley, L. J., Dopita, M. A., Sutherland, R. S., Heisler, C. A., & Trevena, J. 2001, *ApJ*, 556, 121
- Kewley, L. J., & Ellison, S. L. 2008, *ApJ*, 681, 1183
- Kewley, L. J., Geller, M. J., & Jansen, R. A. 2004, *AJ*, 127, 2002
- Kewley, L. J., Groves, B., Kauffmann, G., & Heckman, T. 2006, *MNRAS*, 372, 961
- Kewley, L. J., Rupke, D., Jabran Zahid, H., Geller, M. J., & Barton, E. J. 2010, *ApJL*, 721, L48
- Khoperskov, S., Haywood, M., Di Matteo, P., Lehnert, M. D., & Combes, F. 2018, *A&A*, 609, A60
- Kim, M., Ho, L. C., & Im, M. 2006, *ApJ*, 642, 702

Klein, R., Beckmann, S., Bryant, A., et al. 2014, in , Vol. 9147, Ground-based and Airborne Instrumentation for Astronomy V, 91472X

Kormendy, J., & Ho, L. C. 2013, *ARA&A*, 51, 511

Koss, M. J., Strittmatter, B., Lamperti, I., et al. 2021, *ApJS*, 252, 29

Krumpe, M., Husemann, B., Tremblay, G. R., et al. 2017, *A&A*, 607, L9

Kuiper, G. P. 1938, *ApJ*, 88, 472

Kukreti, P., Morganti, R., Shimwell, T. W., et al. 2022, *A&A*, 658, A6

Lacerda, E. A. D., Sánchez, S. F., Cid Fernandes, R., et al. 2020, *MNRAS*, 492, 3073

Laha, S., Ghosh, R., Guainazzi, M., & Markowitz, A. G. 2018, *MNRAS*, 480, 1522

LaMassa, S. M., Cales, S., Moran, E. C., et al. 2015, *ApJ*, 800, 144

Langer, W. D., & Pineda, J. L. 2015, *A&A*, 580, A5

Lanz, L., Ogle, P. M., Evans, D., et al. 2015, *ApJ*, 801, 17

Le Fèvre, O., Saisse, M., Mancini, D., et al. 2003, in *Proc. SPIE*, ed. M. Iye & A. F. M. Moorwood, Vol. 4841, 1671–1681

Lequeux, J., Peimbert, M., Rayo, J. F., Serrano, A., & Torres-Peimbert, S. 1979, *A&A*, 500, 145

Lesaffre, P., Pineau des Forêts, G., Godard, B., et al. 2013, *A&A*, 550, A106

Leung, G. C. K., Coil, A. L., Azadi, M., et al. 2017, *ApJ*, 849, 48

Lin, L., Pan, H.-A., Ellison, S. L., et al. 2019, *ApJL*, 884, L33

Luhman, M. L., Satyapal, S., Fischer, J., et al. 2003, *ApJ*, 594, 758

Lynden-Bell, D. 1969, *Nature*, 223, 690

Mahony, E. K., Oonk, J. B. R., Morganti, R., et al. 2016, *MNRAS*, 455, 2453

Maiolino, R., Caselli, P., Nagao, T., et al. 2009, *A&A*, 500, L1

Maiolino, R., Gallerani, S., Neri, R., et al. 2012, *MNRAS*, 425, L66

Maiolino, R., Russell, H. R., Fabian, A. C., et al. 2017, *Nature*, 544, 202

Malhotra, S., Kaufman, M. J., Hollenbach, D., et al. 2001, *ApJ*, 561, 766

Mannucci, F., Cresci, G., Maiolino, R., Marconi, A., & Gnerucci, A. 2010, *MNRAS*, 408, 2115

Mannucci, F., Belfiore, F., Curti, M., et al. 2021, *MNRAS*, 508, 1582

Marasco, A., Cresci, G., Nardini, E., et al. 2020, *A&A*, 644, A15

Marino, R. A., Rosales-Ortega, F. F., Sánchez, S. F., et al. 2013, *A&A*, 559, A114

Martin, P., & Roy, J.-R. 1994, *ApJ*, 424, 599

Martín-Navarro, I., Shankar, F., & Mezcua, M. 2022, *MNRAS*, 513, L10

Mathur, S. 2000, *MNRAS*, 314, L17

McBride, J., & McCourt, M. 2014, *MNRAS*, 442, 838

McDonald, M., McNamara, B. R., Calzadilla, M. S., et al. 2021, *ApJ*, 908, 85

McElroy, R. E., Husemann, B., Croom, S. M., et al. 2016, *A&A*, 593, L8

McNamara, B. R., & Nulsen, P. E. J. 2007, *ARA&A*, 45, 117

McNamara, B. R., Nulsen, P. E. J., Wise, M. W., et al. 2005, *Nature*, 433, 45

Mignoli, M., Vignali, C., Gilli, R., et al. 2013, *A&A*, 556, A29

Mihos, J. C., Richstone, D. O., & Bothun, G. D. 1992, *ApJ*, 400, 153

Mommert, M. 2017, *Astronomy and Computing*, 18, 47

Morganti, R., Oosterloo, T., Oonk, J. B. R., Frieswijk, W., & Tadhunter, C. 2015, *A&A*, 580, A1

Mortlock, A., Conselice, C. J., Hartley, W. G., et al. 2013, *MNRAS*, 433, 1185

Mukherjee, D., Wagner, A. Y., Bicknell, G. V., et al. 2018, *MNRAS*, 476, 80

Mullaney, J. R., Alexander, D. M., Aird, J., et al. 2015, *MNRAS*, 453, L83

Murphy, E. J., Condon, J. J., Schinnerer, E., et al. 2011, *ApJ*, 737, 67

Nandra, K., Georgakakis, A., Willmer, C. N. A., et al. 2007, *ApJL*, 660, L11

Nascimento, J. C. d., Storchi-Bergmann, T., Mallmann, N. D., et al. 2019, *MNRAS*, 486, 5075

Nelson, D., Pillepich, A., Springel, V., et al. 2018, *MNRAS*, 475, 624

Nesvadba, N. P. H., Lehnert, M. D., De Breuck, C., Gilbert, A. M., & van Breugel, W. 2008, *A&A*, 491, 407

Nesvadba, N. P. H., Boulanger, F., Salomé, P., et al. 2010, *A&A*, 521, A65

Neumann, J., Gadotti, D. A., Wisotzki, L., et al. 2019, *A&A*, 627, A26

Nielsen, N. M., Churchill, C. W., Kacprzak, G. G., Murphy, M. T., & Evans, J. L. 2015, *ApJ*, 812, 83

Noll, S., Burgarella, D., Giovannoli, E., et al. 2009, *A&A*, 507, 1793

Ogle, P., Antonucci, R., Appleton, P. N., & Whysong, D. 2007, *ApJ*, 668, 699

Page, M. J., Symeonidis, M., Vieira, J. D., et al. 2012, *Nature*, 485, 213

Peng, C. Y., Ho, L. C., Impey, C. D., & Rix, H.-W. 2002, *AJ*, 124, 266

Peng, Y.-j., Lilly, S. J., Kovač, K., et al. 2010, *ApJ*, 721, 193

Perna, M., Sargent, M. T., Brusa, M., et al. 2018, *A&A*, 619, A90

Peterson, B. W., Appleton, P. N., Bitsakis, T., et al. 2018, *ApJ*, 855, 141

Pettini, M., & Pagel, B. E. J. 2004, *MNRAS*, 348, L59

Pillepich, A., Springel, V., Nelson, D., et al. 2018, *MNRAS*, 473, 4077

Piotrowska, J. M., Bluck, A. F. L., Maiolino, R., Concas, A., & Peng, Y. 2020, *MNRAS*, 492, L6

Planck Collaboration, Aghanim, N., Akrami, Y., et al. 2020, *A&A*, 641, A6

Popesso, P., Concas, A., Morselli, L., et al. 2020, *MNRAS*, 496, 2531

Powell, M. C., Husemann, B., Tremblay, G. R., et al. 2018, *A&A*, 618, A27

Prevot, M. L., Lequeux, J., Maurice, E., Prevot, L., & Rocca-Volmerange, B. 1984, *A&A*, 132, 389

Puschig, J., Hayes, M., Östlin, G., et al. 2020, *A&A*, 644, A10

Ramos Padilla, A. F., Ashby, M. L. N., Smith, H. A., et al. 2020, *MNRAS*, 499, 4325

Rani, B., Petropoulou, M., Zhang, H., et al. 2019, *BAAS*, 51, 92

Renzini, A., & Peng, Y.-j. 2015, *ApJL*, 801, L29

Ricci, C., Bauer, F. E., Arevalo, P., et al. 2016, *ApJ*, 820, 5

Rosario, D. J. 2019, FortesFit: Flexible spectral energy distribution modelling with a Bayesian backbone, [ascl:1904.011](https://arxiv.org/abs/1904.011)

Rosario, D. J., Alexander, D. M., Moldon, J., et al. 2021, *MNRAS*, 505, 5283

Rose, T., Edge, A. C., Combes, F., et al. 2019, *MNRAS*, 489, 349

Roth, M. M., Kelz, A., Fechner, T., et al. 2005, *PASP*, 117, 620

Saintonge, A., Catinella, B., Tacconi, L. J., et al. 2017, *ApJS*, 233, 22

Salim, S. 2014, *Serbian Astronomical Journal*, 189, 1

Salim, S., Rich, R. M., Charlot, S., et al. 2007, *ApJS*, 173, 267

Salpeter, E. E. 1964, *ApJ*, 140, 796

Sánchez, S. F., Kennicutt, R. C., Gil de Paz, A., et al. 2012, *A&A*, 538, A8

Sánchez, S. F., Rosales-Ortega, F. F., Iglesias-Páramo, J., et al. 2014, *A&A*, 563, A49

Sánchez, S. F., Barrera-Ballesteros, J. K., Sánchez-Menguiano, L., et al. 2017, *MNRAS*, 469, 2121

Sánchez, S. F., Barrera-Ballesteros, J. K., López-Cobá, C., et al. 2019, *MNRAS*, 484, 3042

Sanders, R. L., Jones, T., Shapley, A. E., et al. 2020, *ApJL*, 888, L11

Sani, E., Lutz, D., Risaliti, G., et al. 2010, MNRAS, 403, 1246

Santoro, F., Oonk, J. B. R., Morganti, R., Oosterloo, T. A., & Tadhunter, C. 2016, A&A, 590, A37

Sargsyan, L., Samsonyan, A., Leboutteiller, V., et al. 2014, ApJ, 790, 15

Schawinski, K., Thomas, D., Sarzi, M., et al. 2007, MNRAS, 382, 1415

Schawinski, K., Virani, S., Simmons, B., et al. 2009, ApJL, 692, L19

Schaye, J., Crain, R. A., Bower, R. G., et al. 2015, MNRAS, 446, 521

Schirmer, M. 2013, ApJS, 209, 21

Schlafly, E. F., & Finkbeiner, D. P. 2011, ApJ, 737, 103

Schmidt, M. 1959, ApJ, 129, 243

Scholtz, J., Harrison, C. M., Rosario, D. J., et al. 2020, MNRAS, 492, 3194

Schroetter, I., Bouché, N. F., Zabl, J., et al. 2019, MNRAS, 490, 4368

Schulz, B., Marton, G., Valtchanov, I., et al. 2017, arXiv, arXiv:1706.00448

Seyfert, C. K. 1943, ApJ, 97, 28

Shangguan, J., Ho, L. C., & Xie, Y. 2018, ApJ, 854, 158

Shankar, F., Weinberg, D. H., Marsden, C., et al. 2020, MNRAS, 493, 1500

Shimizu, T. T., Mushotzky, R. F., Meléndez, M., Koss, M., & Rosario, D. J. 2015, MNRAS, 452, 1841

Silva, L., Granato, G. L., Bressan, A., & Danese, L. 1998, ApJ, 509, 103

Silva, L., Maiolino, R., & Granato, G. L. 2004, MNRAS, 355, 973

Silverman, J. D., Lamareille, F., Maier, C., et al. 2009, ApJ, 696, 396

Singha, M., Husemann, B., Urrutia, T., et al. 2022, A&A, 659, A123

Skibba, R. A., Engelbracht, C. W., Dale, D., et al. 2011, ApJ, 738, 89

Smirnova-Pinchukova, I., Husemann, B., Busch, G., et al. 2019, A&A, 626, L3

Smirnova-Pinchukova, I., Husemann, B., Davis, T. A., et al. 2022, A&A, 659, A125

Smith, J. D. T., Croxall, K., Draine, B., et al. 2017, ApJ, 834, 5

Smith, K. L., Koss, M., Mushotzky, R., et al. 2020, ApJ, 904, 83

Smith, M. W. L., Gomez, H. L., Eales, S. A., et al. 2012, ApJ, 748, 123

Soldi, S., Türler, M., Paltani, S., et al. 2008, A&A, 486, 411

Springel, V., Di Matteo, T., & Hernquist, L. 2005, MNRAS, 361, 776

- Stacey, G. J., Geis, N., Genzel, R., et al. 1991, *ApJ*, 373, 423
- Stacey, G. J., Hailey-Dunsheath, S., Ferkinhoff, C., et al. 2010, *ApJ*, 724, 957
- Stern, J., & Laor, A. 2013, *MNRAS*, 431, 836
- Storchi-Bergmann, T., Schmitt, H. R., Calzetti, D., & Kinney, A. L. 1998, *AJ*, 115, 909
- Strateva, I., Ivezić, Ž., Knapp, G. R., et al. 2001, *AJ*, 122, 1861
- Tacconi, L. J., Genzel, R., Saintonge, A., et al. 2018, *ApJ*, 853, 179
- Temi, P., Marcum, P. M., Young, E., et al. 2014, *ApJS*, 212, 24
- Thorne, K. S. 1974, *ApJ*, 191, 507
- Thorp, M. D., Ellison, S. L., Simard, L., Sánchez, S. F., & Antonio, B. 2019, *MNRAS*, 482, L55
- Tremblay, G. R., Combes, F., Oonk, J. B. R., et al. 2018, *ApJ*, 865, 13
- Tremonti, C. A., Heckman, T. M., Kauffmann, G., et al. 2004, *ApJ*, 613, 898
- Tumlinson, J., Thom, C., Werk, J. K., et al. 2011, *Science*, 334, 948
- Urry, C. M., & Padovani, P. 1995, *PASP*, 107, 803
- Utomo, D., Bolatto, A. D., Wong, T., et al. 2017, *ApJ*, 849, 26
- Valdes, F., Gruendl, R., & DES Project. 2014, in *Astronomical Society of the Pacific Conference Series*, Vol. 485, *Astronomical Data Analysis Software and Systems XXIII*, ed. N. Manset & P. Forshay, 379
- Valdes, F., Gupta, R., Rose, J. A., Singh, H. P., & Bell, D. J. 2004, *ApJS*, 152, 251
- Vogelsberger, M., Genel, S., Springel, V., et al. 2014a, *MNRAS*, 444, 1518
- . 2014b, *Nature*, 509, 177
- Wagg, J., Carilli, C. L., Wilner, D. J., et al. 2010, *A&A*, 519, L1
- Walcher, C. J., Coelho, P. R. T., Gallazzi, A., et al. 2015, *A&A*, 582, A46
- Walsh, J. L., Barth, A. J., Ho, L. C., & Sarzi, M. 2013, *ApJ*, 770, 86
- Wang, T. G., Brinkmann, W., Wamsteker, W., Yuan, W., & Wang, J. X. 1999, *MNRAS*, 307, 821
- Wang, Z., Wiita, P. J., & Hooda, J. S. 2000, *ApJ*, 534, 201
- Weaver, J., Husemann, B., Kuntschner, H., et al. 2018, *A&A*, 614, A32
- Weilbacher, P. M., Streicher, O., Urrutia, T., et al. 2012, *SPIE Conf. Ser.*, 8451, doi:10.1117/12.925114
- Weilbacher, P. M., Streicher, O., Urrutia, T., et al. 2014, in *ASPCS*, Vol. 485, *Astronomical Data Analysis Software and Systems XXIII*, 451

- Wild, V., Heckman, T., & Charlot, S. 2010, MNRAS, 405, 933
- Willett, K. W., Lintott, C. J., Bamford, S. P., et al. 2013, MNRAS, 435, 2835
- Wisotzki, L., Christlieb, N., Bade, N., et al. 2000, A&A, 358, 77
- Wolf, C., Onken, C. A., Luvaul, L. C., et al. 2018, , 35, e010
- Woo, J.-H., Son, D., & Bae, H.-J. 2017, ApJ, 839, 120
- Wyder, T. K., Martin, D. C., Schiminovich, D., et al. 2007, ApJS, 173, 293
- Wylezalek, D., & Zakamska, N. L. 2016, MNRAS, 461, 3724
- Wylezalek, D., Zakamska, N. L., Greene, J. E., et al. 2018, MNRAS, 474, 1499
- Yamamura, I., Makiuti, S., Ikeda, N., et al. 2009, in ASPCS, Vol. 418, AKARI, a Light to Illuminate the Misty Universe, 3
- Yang, G., Boquien, M., Buat, V., et al. 2020, MNRAS, 491, 740
- Yates, R. M., Kauffmann, G., & Guo, Q. 2012, MNRAS, 422, 215
- York, D. G., Adelman, J., Anderson, John E., J., et al. 2000, AJ, 120, 1579
- Zel'dovich, Y. B. 1964, Soviet Physics Doklady, 9, 195

Acknowledgments

“War is a product of despotism. Without despotism, there could be no war; there could be fights, but not war. Despotism produces war, and war sustains despotism. Those who want to fight war must only fight despotism.”

– Leo Tolstoy, 1904

My PhD is a beautiful adventure full of discoveries, travelling, science, and friendship. It started with a breathtaking trip to New Zealand and continued to turn my life upside-down (in a good way). I am enormously grateful to Dr. Bernd Husemann for giving me this opportunity in the first place, and not only for being my supervisor leading me on the scientific path, but also for being so humanly kind, for travelling with me, for giving me parenting advice, for giving me rides when I broke my leg, and many-many more. Thank you!

I thank Prof. Dr. Ralf Klessen for being reachable when I needed supervision, understanding of my family situation, and so approachable that I had absolutely no stress organizing thesis committee meetings (and that’s important for the PhD students).

I thank Prof. Dr. Ralf Klessen again together with Prof. Dr. Jochen Heidt for reading and refereeing this thesis, and Prof. Dr. Henrik Beuther and Prof. Dr. Matthias Bartelmann for agreeing to be on my PhD examination committee, sharing the examination date with me which is a closure of this journey and the beginning of the new one.

Thank you, Julia Lienert and Paul Joseph for taking a look at the Zusammenfassung and giving advice on improving the language.

I thank my colleagues, without them this result would be impossible to achieve. The entire CARS team for being so involved and accessible, especially Françoise Combes, Miguel Pérez-Torres, Rebecca McElroy, Julia Scharwächter, Justus Neumann, Mainak Singha, Nico Winkel, Brent Groves, Tanya Urrutia and Mirko Krumpe that first met me on an internship in Potsdam, Scott Croom, Andreas Eckart, Stefi Baum, Chris O’Dea, Matthieu Bethermin, Tom Rose, and Meredith Powell. The SOFIA team for being involved in the scientific discussion and for a great atmosphere during observations and conferences: Christian and Nadine Fischer, Randolph Klein, William Vacca, Sebastian Colditz, and Alfred Krabbe. My other co-authors for collaborating and agreeing to be in the same boat with me: Johannes Puschnig, Connor Smith, David Rosario, and Philip Appleton.

Directors, post-doctoral researchers, and other employees at MPIA (and LSW) for being a core of the institute, for the technical and logistical support, and for all the small-talks that are a nice part of the everyday life: Hans-Walter Rix for being in the quiz team with me (we did not win of course), Knud Jahnke, Nadine Neumayer, Tom Herbst for "How to give a talk" talks, Annalisa Pillepich, Fabian Walter, Ludmila Carone and Iskren Georgiev for making science coffee a special time in the morning, Mladen Novak for all the celebrated New Years and for your endless optimism, Olga Zakhovzhai for noticing all the colors that match, Bertram Bitsch and Chiara Battistini, Eduardo Banados, Jan-Torge (J-T) Schindler, Gregory Green, Kathryn Kreckel, Dmitry Semenov and Sierk van Terwisga for various delicious food we shared, Trifon Trifonov, Yana Khusanova, Faustine Cantalloube, Alyssa Drake, Alessandra Mastrobuono-Battisti, Rosalie McGurk, Allison Merritt,

Wu Po-Feng, Ingrid Apfel, Christiane Hölscher, Jana Baier, Daniela Scheerer, Ina Beckmann, Ulrich Hiller, Frank and Britta Witzel. Even though no one from this list will find their names here, I find so much joy reading it, as there is a person behind every name bringing up memories that build this stage of my life.

I thank my friends, for making my life better. The fellow IMPRS-HD students that welcomed me, Heidelberg started to feel like home because of you: Chiara Mazzucchelli, Sara Rezaei Khoshbakht, and Michael Rugel (my first office mates), Anna-Christina Eilers, Sarah Leslie, Neven Tomicic, Steffi Yen, Aida Ahmadi and Asmita Bhandare thanks for fighting for student's rights, Christos Vourellis, Yulong Zhuang, Alexander Hygate, Arianna Musso Barucci, Johanna Coronado, Joshua van Houdt, Daniel Rahner, Matthias Samland, Hector Hiss, Thales Gutcke, Matteo Mazzarini, Mayte Alfaro Cuello, Mikhail Kovalev, and Valeriy Vasilyev. I thank Christian Fendt and Huong Witte-Nguy for organising IMPRS retreats and seminars and filming my talks (yes, I watched them). My IMPRS generation: Philipp Hottinger, Vera Wolthoff, Stephan Stock, Martin Schlecker, Giada Peron, Victor Marian, Diana Kossakowski, Melanie Kaasinen, Jindra Gensior, Neige Frankel, Felix Bosco, Bahar Bidaran, Branislav Avramov, Francisco Aros; thank you for the amazing trip to Amsterdam, and sorry I joined the gatherings so rarely finding excuses that I've lived in Boxberg. CHRISTIAN LENZ, thank you for being such a supportive friend and for letting me drive your car without criticizing me, even though I did not know what I am doing. The students from the next generations for keeping the spirit of friendliness: Samantha Brown and Christoph Engler for being around and helping with our cat, Marcelo Barraza, Lizzandra Flores, Jacob Isbell, Oliver Völkel for teaching me boxing, Camille Bergez-Casalou for raclette, Vincent Carpenter, Ismael Pessa Gtierrez and Paz Bluhm congratulations on your wedding, Caroline Gieser, Francesco Conte, Alina Böcker, Riccardo Franceschi for introducing the Haggard music band to me, Giancarlo Mattia for being a princess, Maximilian Häberle for taking the hat building duty off my shoulders and Frida for the Mexican food, Siddhant Deshmukh, Emily Hunt, Theodora Xylakis-Dornbusch, Jonas Syed, Alexander Dimoff, Dhruv Muley, Evert Nasedkin, Selina Nitschai, Eric Rohr, Luzian Seeburger and Markus Kuhlberg for helping with our cat, Verena Fuernkranz, and Olga Borodina good luck with your PhD!

My friends from Moscow, for not vanishing, staying in contact, and even visiting: Alexey Nikonov, Alexandra Grudskaya, Alyona Balakina and Philipp Balakin, Anastasiya Voloshina, Evgenia Kalinicheva and Petr Kalinichev, Sergey Sapozhnikov, Ilya and Anastasiya Kuksenok, Anna Chmyhova, Arthur Avakyan, Kristina Kupriyanova, Anastasia Topchieva, Tamara Molyarova, and Vitaliy Akimkin.

My dear family. My mother Larisa Pinchukova, for giving me the start that I had, and thank you for coming to my Patzer talk! My sister Lyubov Noga, for all the support she gave me during the PhD, pregnancy, and all I had to go through. You really are very understanding and this is something I could always rely on. And of course, the best man in the world, my husband Grigorii Smirnov-Pinchukov, for being my rock, for telling me the right things no matter how bad I react, and for sharing the miracle with me, which is our Marina.

Declaration of Originality

Declaration of Originality

I hereby declare that this thesis is my own work and that I have used no other than the stated sources and aids.

Originalitätserklärung

Ich versichere, dass ich diese Arbeit selbstständig verfasst habe und keine anderen als die angegebenen Quellen und Hilfsmittel benutzt habe.

Heidelberg, May 16, 2022

(Irina Smirnova-Pinchukova)